FEDERAL UNIVERSITY OF SANTA CATARINA
DEPARTMENT OF MECHANICAL ENGINEERING

Ernane Silva

CHARACTERIZATION OF RAREFIED FLOWS OF REFRIGERANTS WITH A NEW METHOD FOR THE MEASUREMENT OF MASS FLOW RATE THROUGH MICROCHANNELS

Florianópolis
2016

Ernane Silva

CARACTERIZAÇÃO DE ESCOAMENTOS RAREFEITOS DE FLUIDOS REFRIGERANTES COM UM NOVO MÉTODO PARA MEDIÇÃO DE VAZÃO EM MICROCANAIS

Tese submetida ao Programa de Pós-Graduação em Engenharia Mecânica da Universidade Federal de Santa Catarina para a obtenção do Grau de Doutor em Engenharia Mecânica.

Orientador:
Prof. César J. Deschamps, Ph.D.
Coorientador:
Prof. Marcos Rojas-Cárdenas, Dr.

Florianópolis
2016

Ficha de identificação da obra elaborada pelo autor,
através do Programa de Geração Automática da Biblioteca Universitária da UFSC.

Silva, Ernane
Caracterização de escoamentos rarefeitos de fluidos refrigerantes com um novo método para medição de vazão em microcanais / Ernane Silva ; orientador, César J. Deschamps ; coorientador, Marcos Rojas-Cárdenas. - Florianópolis, SC, 2016.
181 p.

Tese (doutorado) - Universidade Federal de Santa Catarina, Centro Tecnológico. Programa de Pós-Graduação em Engenharia Mecânica.

Inclui referências

1. Engenharia Mecânica. 2. Mecânica dos fluidos. 3. Dinâmica de gases rarefeitos . I. Deschamps, César J.. II. Rojas-Cárdenas, Marcos. III. Universidade Federal de Santa Catarina. Programa de Pós-Graduação em Engenharia Mecânica. IV. Título.

Ernane Silva

CARACTERIZAÇÃO DE ESCOAMENTOS RAREFEITOS DE FLUIDOS REFRIGERANTES COM UM NOVO MÉTODO PARA MEDIÇÃO DE VAZÃO EM MICROCANAIS

Esta Tese foi julgada adequada para obtenção do Título de Doutor em Engenharia Mecânica e aprovada em sua forma final pelo Programa de Pós-Graduação em Engenharia Mecânica da Universidade Federal de Santa Catarina.

Florianópolis, 6 de dezembro de 2016.

_____

Prof. César José Deschamps, Ph.D.
Orientador
Universidade Federal de Santa Catarina

_____

Prof. Marcos Rojas-Cárdenas, Dr.
Coorientador
Institut National des Sciences Appliquées de Toulouse

_____

Prof. Jonny Carlos da Silva, Dr.
Coordenador do Curso

Banca Examinadora:

_____

Prof. César José Deschamps, Ph.D. – Presidente
Universidade Federal de Santa Catarina

_____

Prof. Felix Sharipov, Ph.D. – Relator
Universidade Federal do Paraná

_____

Prof.ª Carolina Palma Naveira Cotta, Dr.ª
Universidade Federal do Rio de Janeiro

_____

Prof. Julio César Passos, Dr.
Universidade Federal de Santa Catarina

_____

Prof. Jader Riso Barbosa Jr., Ph.D.
Universidade Federal de Santa Catarina

_____

Prof. Alexandre Kupka da Silva, Ph.D.
Universidade Federal de Santa Catarina

To my wife, Bruna Luiza,
to my parents, Adenir and Sônia,
and to my sister, Eliziane.
Nothing would be possible
without all of you.

AKNOWLEDGEMENTS

I would like to express my sincere gratitude to my advisors Prof. César J. Deschamps and Prof. Marcos Rojas-Cárdenas for the continuous support in my doctoral research, motivation and knowledge.

My sincere thanks to the Microfluidics group from the *Institut Clément Ader*, in Toulouse, France, who welcomed me for an academic exchange of 9-months: Prof. Stéphane Colin, Prof. Lucien Baldas, Prof. Christine Barrot-Lattes, Prof. Pascale Magaud, Yanfeng Gao, Shiqi Wang, Dominique Fratantonio, Guillermo López-Quesada, Varun-Kumar Yeachana, Daniel Mariuta, Jie Chen, Hacene Si-Hadj-Mohand, and Nicolas Laurien. Also to Fu Jian, Qiu Donghai, Yiwei Wang and Pierre-André Rey. It was a fruitful experience, fundamental to my academic and personal growth.

Besides, I would like to thank the committee: Prof. Felix Sharipov, Prof. Carolina Palma Naveira Cotta, Prof. Julio César Passos, Prof. Jader Riso Barbosa Jr. and Prof. Alexandre Kupka da Silva, for their valuable comments and contributions to this thesis.

I would like to express my gratitude to the financial support of the National Institute of Science and Technology (INCT) in Refrigeration and Termophysics, CNPq, and Embraco. I am thankful also to the Program of Post-Graduation in Mechanical Engineering, POSMEC, from the Federal University of Santa Catarina.

My thanks also to the Materials Laboratory (LABMAT) and the Center of Reference in Innovative Technologies (CERTI) that assisted me with the measurement of the channels and to the Heat Pipes Laboratory (LABTUCAL) for providing the leak detector and ultrasonic bath. Also, to Prof. Walter Lindolfo Weingaertner, who manufactured the first channels.

Many thanks to my friends from POLO, especially to those who contributed directly to the development of this thesis, providing valuable assistance and technical support: Eduardo Ludgero da Silva, Fabiano Vambömmel, Ricardo Hellmann, Marco Carrilho Diniz, Thiago Dutra, Gustavo Coelho Rezende, Daniel Luiz da Silva, Fernanda Letícia dos Santos, Murilo Ferreira Nicoluzzi and Renata Steinbach.

I would like also to express my sincere gratitude to my family, especially to my parents, Adenir João Silva and Sônia Regina Machado Silva, and my sister, Eliziane Silva. Your support, motivation and encouragement were fundamental to the development of this thesis.

Finally, I would like to thank my wife, Bruna Luiza Santos, for the love, dedication and comprehension.

"There's plenty of room at the bottom."
(Feynman, 1992)

ABSTRACT

The study of gas flows in microchannels, especially with regard to micro- (MEMS) and nano-electromechanical systems (NEMS), is pivotal for the development of new technologies. However, these flows also occur in systems commonly used in our daily lives, for example, gas leakage through valves of domestic refrigeration compressors, where refrigerant fluid flows through gaps formed by surface imperfections. Thus, understanding the physics of such flows and characterizing their behavior is fundamental for the design of numerous technological devices. To this end, the present work experimentally investigated the isothermal flow of rarefied gases in microchannels in order to obtain data that would aid in the design of refrigeration compressors. For this purpose, two experimental setups were designed to analyze rarefied flows: one for circular section channels (microtubes) and the other for rectangular section channels with controlled surface characteristics. In addition, a new technique based on the constant volume method was developed to measure the mass flow rate in microchannels. The flow of N_2 and refrigerant fluids R134a and R600a were analyzed in stainless steel, copper and brass metal microtubes in practically the entire range of slip and transition regimes. The values of the slip coefficient and tangential momentum accommodation coefficient (TMAC) were obtained by comparing these measurements with analytical solutions of the Navier-Stokes equation and numerical results from the BGK model available in the literature. The measurements in the microtubes showed that the gas–surface interaction approaches the complete diffuse behavior with a TMAC of 0.96–1.06.

Keywords: Rarefied flow. Gas–surface interaction. Microchannel.

RESUMO

O estudo de escoamentos de gases em microcanais é de fundamental importância para o desenvolvimento de novas tecnologias, especialmente no que se refere a sistemas micro (MEMS) e nanoeletromecânicos (NEMS). Porém, esses escoamentos também ocorrem em sistemas comumente utilizados em nosso dia-a-dia. Esse é o caso de vazamentos através de válvulas de compressores de refrigeração doméstica, onde fluidos refrigerantes escoam através de folgas formadas por imperfeições superficiais. Assim, entender a física de tais escoamentos e caracterizar o seu comportamento é fundamental no projeto de muitos dispositivos tecnológicos. O presente trabalho é uma investigação experimental de escoamentos isotérmicos de gases rarefeitos em microcanais, com o objetivo de fornecer dados para auxiliar no projeto de compressores de refrigeração. Para tanto, foram desenvolvidas duas bancadas para análise de escoamentos rarefeitos, uma projetada para canais de seção circular (microtubos) e outra para canais de seção retangular a fim de permitir controle sobre a característica da superfície. Além disso, uma nova técnica baseada no método de volume constante foi proposta para a medição de vazão em microcanais. Escoamentos de nitrogênio e fluidos refrigerantes R134a e R600a foram analisados em microtubos metálicos de aço inoxidável, cobre e latão, cobrindo praticamente toda a faixa dos regimes de escorregamento e transição. Valores de coeficientes de deslizamento e acomodação da quantidade de movimento tangencial (TMAC) foram extraídos a partir da comparação dessas medições com soluções analíticas da equação de Navier-Stokes e resultados numéricos do modelo BGK disponíveis na literatura. Observou-se das medições em microtubos que a interação gás-superfície se dá de forma praticamente difusa, com TMAC entre 0,96 e 1,06.

Palavras-chave: Escoamento rarefeito. Interação gás-superfície. Microcanal.

LIST OF FIGURES

LIST OF TABLES

LIST OF SYMBOLS AND ABBREVIATIONS

Roman

a, b	Pressure ratios	
A,B,C	Fitting coefficients	
$\vec{c}$	Thermal or peculiar velocity	m/s
$\bar{c}$	Mean thermal speed	m/s
c_p	Specific heat at constant pressure	$J/(kg \cdot K)$
c_v	Specific heat at constant volume	$J/(kg \cdot K)$
C	Conductance	m^3/s
d	Mean molecular diameter	m
D	Diameter	m
dE	Energy flux per unit time	$J/(m^2 \cdot s)$
e	Specific internal energy	J/kg
f	Velocity distribution function	s^3/m^6
f^M	Maxwellian velocity distribution function	s^3/m^6
f_{loc}^M	Local Maxwellian velocity distribution function	s^3/m^6
$\vec{F}$	External body force per unit of mass	N/kg
$\vec{F}_i$	Intermolecular force	N
FS	Full scale of the pressure transducer	Pa
G	Reduced mass flow rate	
h	Height	m
k	Thermal conductivity	$W/(m \cdot K)$
k_B	Boltzmann constant	J/K
k_λ	Coefficient of the molecular model	
Kn	Knudsen number	
l_{sv}	Characteristic length of the sampling volume	m

L	Characteristic length of the system, length	m, m
m	Molecular mass, mass	kg, kg
$\dot{m}$	Mass flow rate	kg/s
M	Molar weight	g/mol
Ma	Mach number	
n	Number density, normal coordinate, number of points	$m^{-3}, m, -$
$\dot{n}$	Molar flow rate	mol/s
N	Number of molecules	
P	Pressure	Pa
P^*	Pressure (auxiliary variable)	Pa
Q	Throughput, reduced mass flow rate	$Pa \cdot m^3/s, -$
Q_v	Volumetric flow rate	m^3/s
r	Radial coordinate	m
$\vec{r}$	Position vector	m
R	Specific gas constant	$J/(kg \cdot K)$
R_1	Inner radius	m
R_2	Outer radius	m
Ra	Arithmetic average surface roughness	m
Re	Reynolds number	
Rz	Average maximum peak to valley of five consecutive sampling lengths within the measuring length	m
s	Tangential coordinate	m
S	Dimensionless mass flow rate	
t	Time	s
T	Temperature	K
$\vec{u}$	Gas bulk velocity	m/s

$\vec{v}$	Velocity of the molecules	m/s
V	Sampling volume, volume	m^3, m^3
V_0	Equivalent volume	m^3
V_C	Volume of the sample cylinder	m^3
w	Width	m
x, y	Transversal coordinates	m
z	Longitudinal coordinate	m

Greek

α	Tangential momentum accommodation coefficient, coefficient of the VSS model	
α^L	Tangential momentum accommodation coefficient extracted using the formulation proposed by Loyalka *et al*. (1975)	
α^M	Tangential momentum accommodation coefficient extracted using the formulation proposed by Maxwell (1879)	
α^S	Tangential momentum accommodation coefficient extracted using the formulation proposed by Loyalka *et al*. (1968)	
α_n	Accommodation coefficient of kinetic energy due to the normal velocity	
α_T	Energy accommodation coefficient	
β_w	Slip coefficient employed by Blanchard and Ligrani (2007)	
γ	Specific heat ratio	
δ	Mean molecular spacing, rarefaction parameter	$m, -$
ΔP	Pressure difference	Pa
ΔV	Volume change	m^3
$\Delta\theta$	Angular distance	rad

ε	Relative variation of temperature	
η	Coefficient of the IPL and Leonard-Jones models	
η'	Coefficient of the Leonard-Jones model	
κ	Coefficient of the IPL and Leonard-Jones models	
κ'	Coefficient of the Leonard-Jones model	
λ	Mean free path	m
μ	Viscosity	$Pa \cdot s$
Π	Pressure ratio	
ρ	Density	kg/m^3
σ_P	First-order slip coefficient	
σ_P^L	First-order slip coefficient extracted using the formulation proposed by Loyalka *et al.* (1975)	
σ_P^M	First-order slip coefficient extracted using the formulation proposed by Maxwell (1879)	
σ_P^S	First-order slip coefficient extracted using the formulation proposed by Loyalka *et al.* (1968)	
σ_{2P}	Second-order slip coefficient	
τ	Momentum, relaxation time (BGK), characteristic time	$kg \cdot m/s$, s, s
ν	Collision frequency	$1/s$
υ	Most probable molecular speed	m/s
φ	Intermolecular potential	$N \cdot m$
ω	Collision frequency (BKG), exponent of the law of viscosity, angular speed	$1/s$, $-$, rad/s
Ψ_i	Fitting coefficients of the dynamic constant volume method	
Ω	Collision term	s^2/m^6

Subscript

0	Reference condition

1	Upstream
2	Downstream
eq	Equivalent
EQ	Equilibrium
exp	Experimental
i	Incident, index
m	Mean
o	Outlet
r	Reflected
s	Tangential component
th	Theoretical
w	Wall

Superscrit

0	Initial condition
i	Index
∞	Final condition

Abbreviation

BGK	Bhatnagar-Gross-Krook
CL	Cercignani-Lampis
EAC	Energy accommodation coefficient
GHS	Generalized hard sphere
HS	Hard sphere
IPL	Inverse power law
VHS	Variable hard sphere
VS	Variable sphere
VSS	Variable soft sphere
M	Maxwell

MD	Molecular Dynamics
MEMS	Micro-electromechanical systems
MM	Maxwell molecules
NEMS	Nano-electromechanical systems
TMAC	Tangential momentum accommodation coefficient

CONTENTS

1 INTRODUCTION

In an article published in 1960 entitled "*There's plenty of room at the bottom"*, the famous physicist Richard P. Feynman described the problem of controlling and manipulating things on small scale as a field in which little had been done and which would have an enormous number of applications in the upcoming future (Feynman, 1992). Considerable progress has been made in this field since then, with the increasing demands for miniaturization in almost every industrial and research field. Nowadays, micro-electromechanical systems (MEMS) are employed in different applications, such as deployment of airbags, drug delivery, cell sorting, fluid pumping, actuators and sensors.

These MEMS appeared in the 1980s with the advance of microfabrication techniques. Initially this denomination was employed because most applications involved both mechanical and electronic components only. Even with the current sophistication of microsystems, this term remained unaltered and today MEMS are also related to different physical phenomena, such as optics and fluidics. In fluidics, the first application can be traced back to 1975, with the creation of a miniaturized gas chromatography system, but it was only in the 1990s that the field of microfluidics really emerged. Nowadays, there is a myriad of MEMS for microfluidic applications as, for instance, micropumps, micromixers, microactuators, microsensors and droplet dispensers (Tabeling, 2005).

Microfluidics differs from the conventional continuum theory of fluid flows. According to Karniadakis *et al*. (2005), in microgeometries the flow is granular for liquids and rarefied for gases, and the walls "move". In addition, other phenomena such as thermal creep, electrokinetics, viscous heating, anomalous diffusion, and even quantum and chemical effects become important. Also, it has been proven that the material of the wall and the quality of its surface play a crucial role in the momentum and energy exchange of the fluid at the wall.

Microflows can also be found in applications other than MEMS. An example is the leakage of gas in valves of compressors adopted in household refrigeration systems. These valves are commonly referred to as automatic valves because they are actuated by pressure differences. When closed, such valves must avoid any leak of gas from high- to low-pressure chambers. However, small microchannels are formed due to geometrical imperfections on the valve and seat surfaces (Figure 1.1). Silva and Deschamps (2015) found that even tiny clearances may significantly affect the isentropic and volumetric efficiencies of oil-less reciprocating compressors. For instance, their predictions showed that a

clearance with a dimension of 1 μm would reduce the isentropic and volumetric efficiencies by 4.4% and 2.7%, respectively. The authors also indicated the existence of non-continuum effects on the flow.

In this sense, the design of many technological appliances requires the understanding and correct characterization of non-continuum effects in gas microflows, which is the motivation for the present study. Particularly, the main interest resides in the analysis of flows of gases commonly employed in the refrigeration industry, such as R134a (1,1,1,2-Tetrafluorethane) and R600a (Isobutane), and nitrogen with emphasis on the gas–surface interaction for isothermal flows, which, in this work, are characterized by means of slip and accommodation coefficients obtained experimentally from measurements of mass flow rate. These measurements are performed using the dynamic constant volume method developed in this work, which associates the mass flow rate through a channel with pressure variations in the reservoirs located upstream and downstream. The slip and accommodation coefficients are necessary for the correct modeling of such flows and play a determinant role at the level of the boundary conditions. Therefore, they must be determined in order to estimate leakage in compressor valves. The following sections address the aspects that make gas microflows not treatable with conventional continuum theory and the alternatives for its modeling. Theoretical aspects necessary to determine the flow regimes are introduced together with the models used to extract the investigated coefficients.

1.1 GAS MICROFLOWS

The description of gas flows in microgeometries can differ from the conventional theory established by the continuum hypothesis of classical Fluid Mechanics. The continuum assumption neglects the microscopic discontinuities within the flow. Hence, all macroscopic properties, such as density, temperature, pressure and velocity, are assumed to vary continuously from point to point. This is accomplished by averaging microscopic properties on a sufficiently large sampling volume, containing a significant number of molecules, in order to avoid the influence of microscopic fluctuations. If the sampling volume is too small, fluctuations in the average value of a property over the sampling volume are caused by variations in the number and kind of molecules inside it. On the other hand, this sampling volume must be sufficiently small so that the local value of a macroscopic property can be defined independently of spatial variations (Batchelor, 1967), as shown in Figure 1.2.

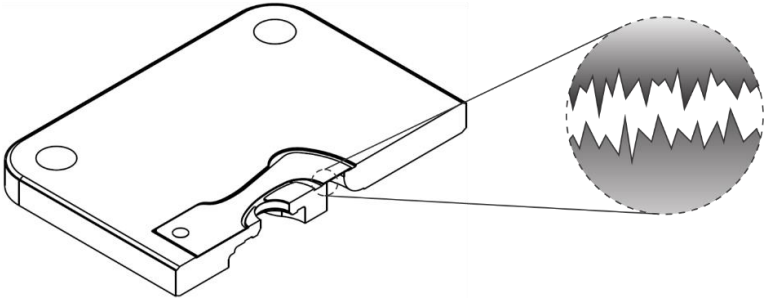

Figure 1.1 – Schematic representation of geometric imperfections in the valve and seat of a refrigeration compressor.

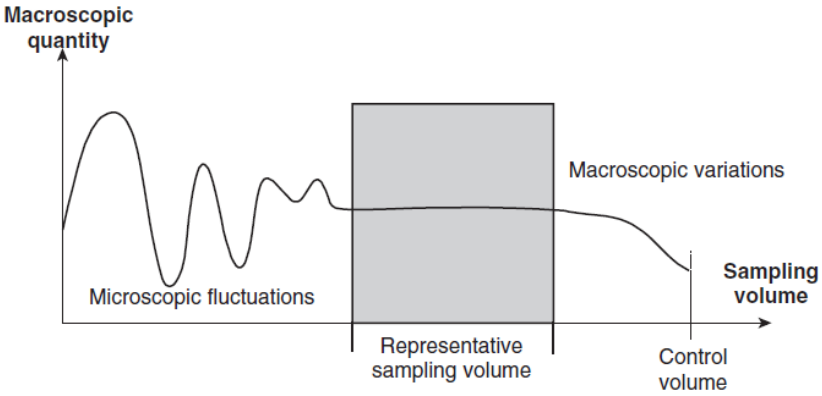

Figure 1.2 – Variation of an arbitrary average quantity according to the sampling volume size (Colin, 2014).

In gas flows through microsystems, the size of the sampling volume is limited by the size of the system and the sampling volume may have an insufficient number of molecules for averaging microscopic properties. Therefore, a well-defined criterion must be considered to assess whether the continuum assumption is acceptable or not. According to Karniadakis *et al*. (2005), a sampling volume containing 10^4 molecules presents 1% statistical variation in the macroscopic properties. A gas at 1 mbar and 20 °C, for instance, has approximately 2.5×10^4 molecules in a volume with 1 μm^3. If this 1% statistical fluctuation is considered as a limit for the continuum hypothesis, then it is possible to define a parameter to evaluate its validity.

Consider a sampling volume V, with characteristic length l_{sv}, which encompasses N molecules. The number density n is defined as

$$n = \frac{N}{V} = \frac{N}{{l_{sv}}^3} \ , \tag{1.1}$$

and its inverse, the mean volume occupied by one molecule, can be related to the mean molecular spacing δ as

$$\frac{1}{n} = \frac{{l_{sv}}^3}{N} = \delta^3 \ . \tag{1.2}$$

From the condition suggested by Karniadakis *et al*. (2005) regarding the 1% of statistical fluctuation for a gas volume sample containing $N = 10^4$ molecules, one obtains

$$\frac{l_{sv}}{\delta} = 10^{4/3}. \tag{1.3}$$

Since l_{sv} must be much smaller than L, the characteristic dimension of the system, in order to capture the spatial variations of the macroscopic properties of the flow, the continuum hypothesis requires that

$$\frac{L}{\delta} \gg 10^{4/3} \ , \tag{1.4}$$

which is a condition that is not always achieved in gas microflows.

The continuum assumption also requires the existence of thermodynamic equilibrium in the sampling volume (local equilibrium). This implies that the local thermodynamic properties in the sampling volume satisfy the same thermodynamic relations as those for a system in equilibrium even if this condition does not apply for the whole system. This assumption requires that the characteristic time associated to the macroscopic transient processes (non-equilibrium processes) be much larger than the time necessary for the sampling volume to reach an appropriate equilibrium state when isolated from the real system (Balmer, 2011). Therefore, the frequency of intermolecular collisions inside the sampling volume must be high enough, which implies that the gas mean free path λ, the average distance traveled by a molecule between two

consecutive collisions, be small when compared to the length of the sampling volume. Consequently,

$$Kn = \frac{\lambda}{L} \ll 1 \,. \tag{1.5}$$

This ratio is commonly used in rarefied gas flows and is known as the Knudsen number, Kn. In internal flows, such as the ones occurring in microsystems, when the Knudsen number is not small, local thermodynamic non-equilibrium effects become relevant to the flow. This non-equilibrium occurs in a fluid layer in the vicinity of the walls known as Knudsen layer, where there are fewer intermolecular interactions than in the core of the flow. The Knudsen layer extends away from the walls for a length on the order of the mean free path. For smaller Knudsen numbers it represents a very small region of the domain. However, as Kn increases this layer grows and affects more and more the flow, until the non-equilibrium condition extends all over the channel. Under these circumstances, the continuum assumption is not appropriate anymore and a molecular description is necessary. Similarly, the mean free time, the average elapsed time between two consecutive collisions, must remain much smaller than the characteristic time associated with the variations of the macroscopic properties in the flow in order to guarantee local equilibrium.

The Boltzmann equation, to be introduced in the next section, forms the basis for the molecular description of flows. A strong assumption that has to be made in the derivation of this equation is the dilute gas assumption. In a dilute gas, most of the intermolecular collisions are of binary nature and this simplifies considerably the treatment of the collision term in the Boltzmann equation. However, a gas, to be considered dilute, must satisfy the following condition:

$$\frac{d}{\delta} \ll 1, \tag{1.6}$$

where d is the molecular diameter of the gas.

Figure 1.3 presents a schematic representation of the main length scales at the molecular level, while Figure 1.4 presents the limits of validity for the regions of dilute gas approximation ($\delta/d = 7$), thermodynamic equilibrium ($\lambda/L = 0.1$), and negligible statistical fluctuations ($L/\delta = 100$) as suggested by Bird (1994). The mean free path is defined as (Colin, 2014)

$$\lambda_{HS} = \frac{\delta^3}{\sqrt{2}\pi d^2}\,, \tag{1.7}$$

where HS stands for hard sphere molecular model, which will be introduced in Section 1.3. As one can notice, the mean free path is directly proportional to the cube of the molecular spacing and inversely proportional to the square of the molecular diameter.

In Figure 1.4, the three lines practically intersect each other at a single point. The line defining the local thermodynamic equilibrium limit is always between the limits of both the statistical fluctuations and dilute gas. Then, when the characteristic length of the system, L, is reduced for a dilute gas at constant molecular spacing, δ, the thermodynamic non-equilibrium limit is reached before the level of statistical fluctuations becomes relevant for a particular gas with mean molecular diameter d. On the other hand, statistical fluctuations are present before thermodynamic non-equilibrium is reached for a dense gas. Since most studies on gas microflows involve the use of dilute gases, Figure 1.4 shows why gas microflows are usually categorized in analogy with rarefied gas flows and the flow regimes are treated as a function solely of the Knudsen number. Even if the analogy is not complete, it is a convenient manner to identify the flow regimes.

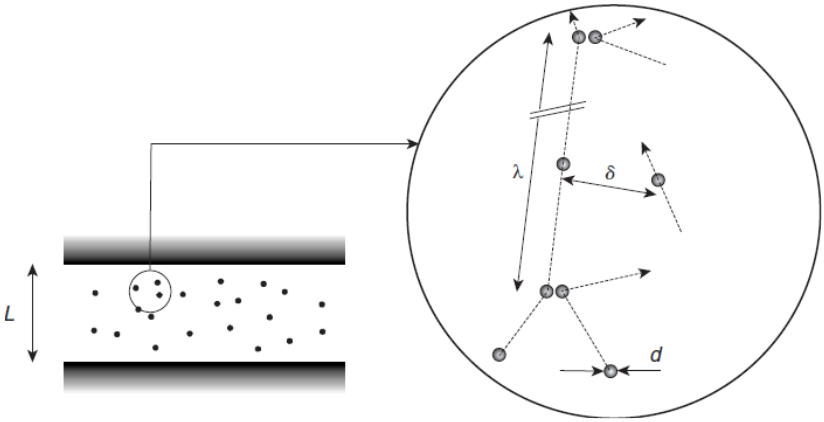

Figure 1.3 – Main characteristic length scales at the molecular level (Colin, 2014).

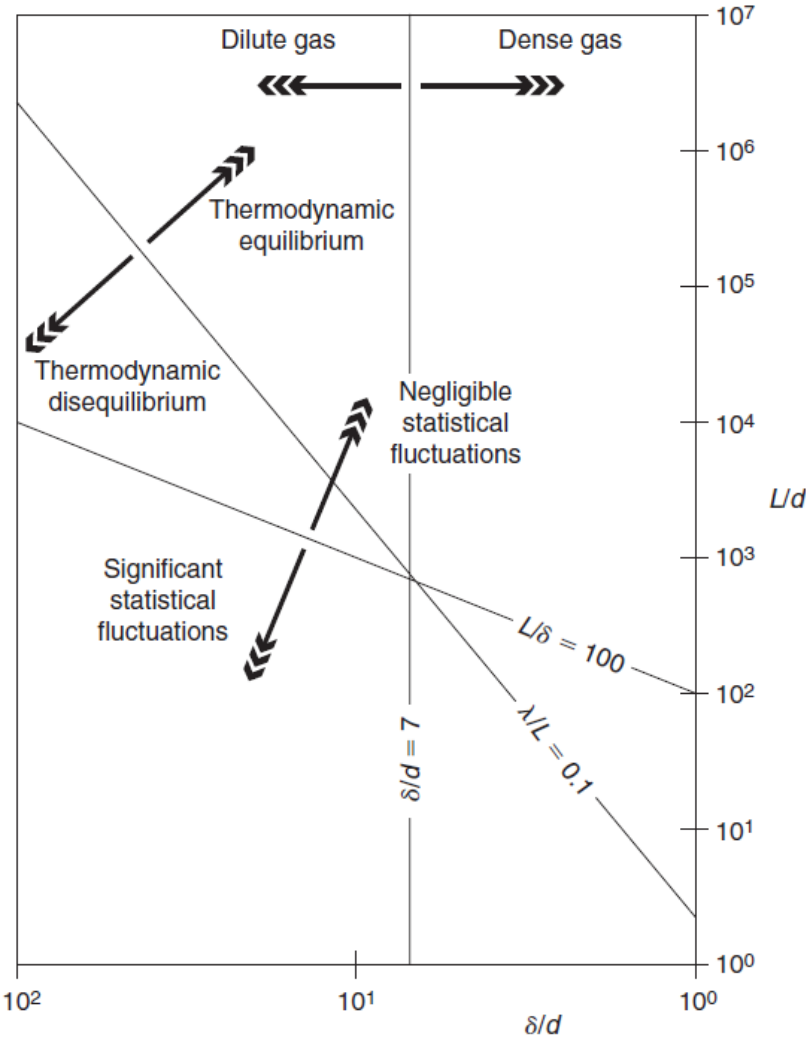

Figure 1.4 – Limits of the main assumptions for the modeling of gas microflows (Colin, 2014).

1.2 FLOW REGIMES

As verified in the last section, rarefaction, characterized by means of Kn, is the main effect associated with the reduction of the characteristic size of systems. This allows us to treat gas microflows in analogy with the theory of rarefied gas flows and categorize the flow regimes simply with respect to the Knudsen number. This is commonly referred to as Knudsen analogy. In this sense, the flows can be classified in hydrodynamic, slip flow, transition and free molecular regimes (Figure 1.5). The definition of the boundaries of each regime is based on empiricism and may vary according to different authors.

Also, the definition of the appropriate characteristic dimension of the system, L, can be misleading. In general, it is chosen to be the hydraulic diameter or the depth of the channel (Colin, 2014). However, sometimes it is preferable to define a local Knudsen number with L based on the length scale of macroscopic gradients (Bird, 1994), such as the density gradient:

$$L = \frac{\rho}{d\rho/dx}. \tag{1.8}$$

The rarefaction level is many times characterized in terms of the alternative parameter δ (not to be confused with the mean molecular spacing), known as the rarefaction parameter, defined as

$$\delta = \frac{L}{\lambda_{eq}}, \tag{1.9}$$

where $\lambda_{eq} = \mu\sqrt{2RT}/P$ is the equivalent mean free path and μ, R, T and P are the gas viscosity, specific gas constant, temperature and pressure, respectively.

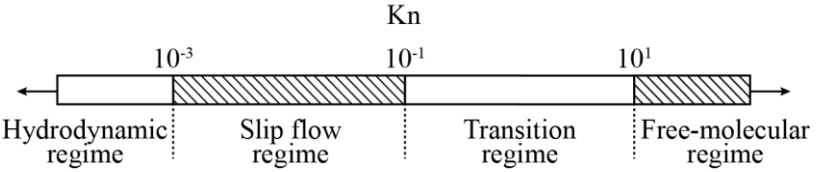

Figure 1.5 – Gas flow regimes as a function of the Knudsen number.

According to the regime of rarefaction, different theories are used to describe the flow. In the hydrodynamic flow regime ($Kn < 10^{-3}$), the flow can be described by means of the Navier-Stokes equation together with the conservation of mass and energy. In addition, the boundary conditions consider temperature and velocity continuity at the interface between fluid and solid wall. The governing equations can be applied to model flows from a macroscopic perspective, discarding any microscopic depart from equilibrium.

As the Knudsen number is increased, eventually the thermodynamic non-equilibrium near the wall increases and the effect of the Knudsen layer cannot be neglected. In this case, a continuum description of the flow would not be appropriate. However, in the slip flow regime ($Kn < 10^{-1}$) the thickness of the Knudsen layer is considerably small and the hydrodynamic equations can still be considered by modifying the boundary conditions to take into account a velocity slip and a temperature jump at the wall.

Under more rarefied conditions, as in the transition ($Kn > 10^{-1}$) and free molecular ($Kn > 10$) flow regimes, the continuum models fail and a molecular approach is required. Then, the flow must be described via the Boltzmann equation, where the only parameter of interest is the velocity distribution function, describing the number of molecules in a six-dimensional space formed by the three components of the position vector and the three components of the velocity vector. In this case, all flow parameters can be derived from the velocity distribution function.

The next section presents the models used to describe the gas behavior under different rarefaction conditions. Initially, extended boundary conditions, taking into account the slip velocity of the gas at the wall, are described for the slip flow regime. Then, the Boltzmann equation is introduced for flows in the transition and free molecular flow regimes.

1.2.1 Slip flow regime (extended boundary conditions)

Maxwell (1879) proposed the first model for slip flow regime developed from a molecular approach that described the gas interaction with the wall. Maxwell referred to a momentum balance at the wall assuming that a fraction α of the molecules colliding against the surface was reflected diffusely, i.e., with complete loss of their tangential momentum before collision, with velocities distributed as if the molecules were issuing from a gas at rest with respect to the wall; the remainder fraction of the molecules $(1 - \alpha)$ was reflected in a specular manner, with

the tangential momentum of the molecules remaining unaltered after collision (Kennard, 1938). These two types of collisions are schematically represented in Figure 1.6. In order to formulate the model, Maxwell assumed that the incident molecules on the surface do not interact with the reflected ones, that is, the incident molecules have the same velocity distribution function as those in the midst of the gas (Zhang *et al*., 2012a). Then, the first form of boundary condition for continuum models taking into account a slip velocity at the wall was given by (Colin, 2014)

$$u_s - u_w = \frac{2-\alpha}{\alpha}\lambda_M \left[\frac{\partial u_s}{\partial n} - \frac{3}{2}\frac{\mu}{\rho T}\frac{\partial^2 T}{\partial s \partial n}\right]_w + \frac{3}{4}\left[\frac{\mu}{\rho T}\frac{\partial T}{\partial s}\right]_w , \tag{1.10}$$

where u_s is the tangential component of the gas velocity and u_w is the velocity of the wall. The parameters μ, ρ, P and T represent the viscosity, density, pressure and temperature of the gas. The coordinates normal and tangential to the wall are represented by n and s, respectively. The mean free path λ_M was defined by Maxwell as follows:

$$\lambda_M = \frac{\sqrt{\pi}}{2}\frac{\mu\sqrt{2RT}}{P} , \tag{1.11}$$

where R is the specific gas constant.

As indicated by Colin (2014), Eq. (1.10) is usually simplified to the following form:

$$u_s - u_w = \frac{2-\alpha}{\alpha}\lambda_M \left[\frac{\partial u_s}{\partial n}\right]_w + \frac{3}{4}\left[\frac{\mu}{\rho T}\frac{\partial T}{\partial s}\right]_w . \tag{1.12}$$

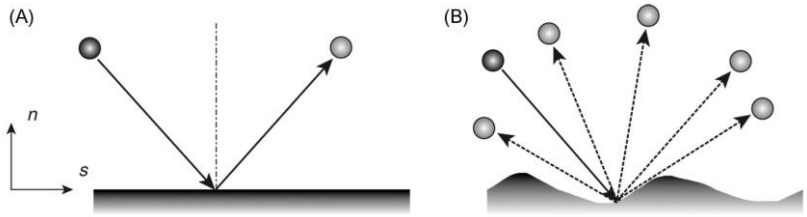

Figure 1.6 – Incident and re-emerging velocities of a molecule after a gas–surface interaction. Specular (a) and diffuse (b) reflections (Colin, 2014).

In Eqs. (1.10) and (1.12) the derivatives are calculated at the wall. The coefficient α is called the tangential momentum accommodation coefficient (TMAC) and can be expressed as a function of the momentum of the incident (τ_i) and reflected (τ_r) molecules with respect to the momentum of the wall (τ_w), that is,

$$\alpha = \frac{\tau_i - \tau_r}{\tau_i - \tau_w} \ . \tag{1.13}$$

The value of α characterizes the gas–surface interaction and varies from zero to unity according to the diffuse-specular scattering proposed by Maxwell, with zero indicating a complete specular reflection of a perfectly smooth surface and a unitary value corresponding to a fully diffuse reflection. The value of the TMAC is affected by several parameters, such as the gas species, surface material and surface conditions such as roughness, temperature and the presence of contaminants (Agrawal & Prabhu, 2008).

The second term on the right hand side of Eq. (1.12) represents the thermal creep or thermal transpiration phenomenon. It consists in inducing a flow in the absence of any pressure gradient only by subjecting the flow to a temperature gradient parallel to the wall. In this case, the slip velocity is different from zero and the gas flows in the direction of the temperature gradient, that is, from the colder region toward the warmer region.

Many authors have proposed second-order boundary conditions for isothermal flows in an attempt to extend the functionality of the continuum models to more rarefied flows (Zhang *et al*., 2012a). A general form of these second-order boundary conditions can be written as follows:

$$u_s - u_w = \pm \frac{\sigma_P}{k_\lambda} \lambda \left(\frac{\partial u}{\partial n}\right)_w - \frac{\sigma_{2P}}{{k_\lambda}^2} \lambda^2 \left(\frac{\partial^2 u}{\partial n^2}\right)_w \ , \tag{1.14}$$

where σ_P and σ_{2P} are the first- and second-order slip coefficients and k_λ is a parameter dependent on the molecular model considered. The different molecular models are described in Section 1.3.

The slip coefficients are weakly dependent of the molecular model (Perrier *et al*., 2011) and σ_P can be directly related to the TMAC. For the particular case of Eq. (1.12), which is a simplification of the more general expression derived by Maxwell (1879), the first slip coefficient is given by

$$\sigma_P^M = \frac{\sqrt{\pi}}{2}\frac{2-\alpha^M}{\alpha^M}\cdot \tag{1.15}$$

The parameter α^M denotes the TMAC extracted from the slip coefficient σ_P^M as proposed by Maxwell. As already mentioned, a simplification of this formulation is to consider that the incident molecules on the surface do not interact with the reflected molecules. More elaborate formulations have been proposed in the literature since then. For instance, Loyalka *et al*. (1975) proposed the following alternative relation derived from results obtained by the numerical solution of the BGK kinetic model, considering the effect of the interaction of the incident and reflected molecules in the Knudsen layer:

$$\sigma_P^L = \frac{\sqrt{\pi}}{2}\frac{2-\alpha^L}{\alpha^L}(1+0.1621\alpha^L)\cdot \tag{1.16}$$

An alternative formulation presented earlier by Loyalka *et al*. (1968), based on the solution of the Boltzmann equation by means of variational methods, written as

$$\sigma_P^S = \frac{2-\alpha^S}{\alpha^S}\left(\sigma_P^S(1) - 0.1211(1-\alpha^S)\right), \tag{1.17}$$

was recommended by Sharipov and Seleznev (1998) for practical calculations. In this equation, $\sigma_P^S(1) = 1.016$ and represents the value of the slip coefficient for $\alpha^S = 1$, being consistent with theoretical predictions of Albertoni *et al*. (1963). Equations (1.15)-(1.17) represent the most commonly referred expressions in the literature relating the slip coefficient to the TMAC. Such expressions will be used in the present work to determine experimentally TMACs in the slip and early transition flow regimes.

By analogy with the slip velocity, an expression for the temperature jump can be obtained from an energy balance at the wall (Kennard, 1938), that is,

$$T - T_w = \frac{2-\alpha_T}{\alpha_T}\frac{2\gamma}{\gamma+1}\frac{k}{\mu c_P}\lambda\left.\frac{\partial T}{\partial n}\right|_w \ , \tag{1.18}$$

where T and T_w are the gas temperature and the wall temperature, respectively. The parameters γ and k represent the specific heat ratio

($= c_P/c_V$), that is, the specific heat at constant pressure over the specific heat at constant volume, and the thermal conductivity of the gas.

The parameter α_T is the energy accommodation coefficient (EAC) and represents the fraction of the molecules that change their mean thermal energy by experiencing a long contact with the wall. It is assumed that these molecules are reemitted as if they were issuing from a gas at the temperature of the wall (Colin, 2014). Accordingly, $(1-\alpha_T)$ represents the fraction of the molecules that are reflected with their incident thermal energy. As the TMAC, the EAC can vary between zero and one. The EAC can similarly be expressed as a function of energy fluxes associated with the incoming (dE_i) and reflected molecules per unit time (dE_r) and the energy flux per unit time that would be associated with the reflected molecules if they issued from a gas in equilibrium at the wall temperature (dE_w), that is,

$$\alpha_T = \frac{dE_i - dE_r}{dE_i - dE_w} \ . \tag{1.19}$$

The EAC also depends on the nature of the interaction between the gas molecules and the surface (Kennard, 1938).

Although the diffuse-specular scattering model proposed by Maxwell (1879) has been widely employed in the literature for its simplicity, some works (Sharipov, 2003; Sharipov, 2011) have considered a more physical model proposed by Cercignani and Lampis (1971). The Cercignani-Lampis (CL) model depends on two parameters: the accommodation coefficient of tangential momentum α and the accommodation coefficient of kinetic energy α_n due to the normal velocity. The parameter α varies in the range from 0 to 2 while α_n varies from 0 to 1. A particularity of the CL model is that it admits back scattering, when the molecule is reflected in the same incident direction with opposite velocity, which may occur in a rough surface (Sharipov, 2003). A difficulty arises in the determination of α and α_n since two different experiments must be performed using the same gas and channel. For instance, one may determine α and α_n from the simultaneous analysis of Poiseuille flow and thermal creep. In the present work, only the diffuse-specular model is considered since it allows the comparison with data from the literature and only one experiment is necessary to determine α.

1.2.2 Transition and free molecular regimes (Boltzmann equation)

In the transition and free molecular flow regimes all flow properties are described in terms of the velocity distribution function $f(t,\vec{r},\vec{v})$. The distribution function represents the number of molecules dN at time t positioned between $\vec{r}$ and $\vec{r}+d\vec{r}$ with velocities between $\vec{v}$ and $\vec{v}+d\vec{v}$, that is,

$$dN = f(t,\vec{r},\vec{v})d\vec{r}d\vec{v} \ . \tag{1.20}$$

Using this definition, the number density, n, indicated in Eq. (1.1) can be alternatively written as

$$n(t,\vec{r}) = \int f(t,\vec{r},\vec{v})d\vec{v} \ . \tag{1.21}$$

All macroscopic quantities, such as density, ρ, bulk velocity, $\vec{u}$, and internal energy, e, can be determined from f. For instance:

$$\rho(t,\vec{r}) = \int mf(t,\vec{r},\vec{v})d\vec{v}, \tag{1.22}$$

$$\vec{u}(t,\vec{r}) = \frac{1}{n}\int \vec{v}f(t,\vec{r},\vec{v})d\vec{v} \ , \tag{1.23}$$

$$e(t,\vec{r}) = \frac{1}{\rho}\int \frac{mc^2}{2}f(t,\vec{r},\vec{v})d\vec{v} \ , \tag{1.24}$$

where m is the molecular mass and $\vec{c} = \vec{v} - \vec{u}$ is the thermal or peculiar velocity relative to the bulk fluid velocity $\vec{u}$.

The velocity distribution function $f(t,\vec{r},\vec{v})$ depends on seven independent variables: time, t, position, $\vec{r}$, and velocity, $\vec{v}$, of the molecules, and is determined from the solution of the Boltzmann equation (Karniadakis *et al*., 2005)

$$\frac{\partial f}{\partial t} + \vec{v}\cdot\frac{\partial f}{\partial \vec{r}} + \vec{F}\cdot\frac{\partial f}{\partial \vec{v}} = \Omega(f) \ . \tag{1.25}$$

In this equation, the parameter $\vec{F}$ is an external body force per unit of mass. The term $\vec{v} \cdot \frac{\partial f}{\partial \vec{r}}$ represents the convection of molecules across the faces of an infinitesimal volume $d\vec{r}$ in the physical space due to velocity $\vec{v}$. The term $\vec{F} \cdot \frac{\partial f}{\partial \vec{v}}$ represents the balance of molecules that leave or enter an infinitesimal volume $d\vec{v}$ in the velocity space by the influence of the external force $\vec{F}$, which can be due to gravity or electromagnetic fields, for instance.

The term on the right-hand side of Eq. (1.25), $\Omega(f)$, is the collision term and has an integral nature, which contrasts with the differential nature of the left-hand side of this equation. This term represents the scattering of molecules in and out of the infinitesimal volume $d\vec{r}d\vec{v}$ in the six-dimensional space defined by the three components of the position vector and the three components of the velocity vector. The collision term is responsible for most of the difficulties associated with the solution of the Boltzmann equation. In this sense, to make the problem treatable, the gas is assumed dilute and, consequently, only binary collisions are considered. Therefore, the collision term depends on the velocity distribution f of the incident and reflected molecules in a binary collision. Since it does not require the thermodynamic equilibrium condition, the Boltzmann equation is valid in the whole rarefaction range. However, due to the inherent difficulties associated with its solution, Eq. (1.25) is usually solved for simplified flow situations.

When the gas is at equilibrium, that is, no macroscopic motion, no heat exchange and no chemical reactions occur in the gas (Sharipov, 2016), f assumes a particular form known as the Maxwellian distribution function, f^M. The kinematic definition of equilibrium imposes that the distribution of molecular velocities is independent of time and location, then $f^M = f(\vec{v})$ (Gombosi, 1994) and the resulting equation is

$$f^M(\vec{v}) = \frac{n}{[2\pi RT]^{3/2}} e^{-\frac{v^2}{2RT}} \ , \tag{1.26}$$

where n and T are constant over the whole reservoir containing the gas.

In the free molecular regime, the gas molecules are very distant from one another and the balance of molecules that enter and leave the infinitesimal volume $d\vec{r}d\vec{v}$ is null. Consequently, $\Omega(f) = 0$ and Eq. (1.25) can be easily solved. For less rarefied flows, the balance of intermolecular collisions cannot be disregarded and the solution of the Boltzmann equation becomes very complicated. Therefore, in many

practical situations the collision operator is approximated with a simpler operator, keeping some of its important physical and mathematical properties. The main idea is that the details of the collision operator that do not affect significantly the values of many experimentally measured quantities can be suppressed by adopting a "blurred image" of it, i.e., a simpler operator that is able to retain qualitative and average properties of the true collision operator (Cercignani, 1988). Therefore, Eq. (1.25) can be solved without significant error (Mohamad, 2011). Models using a simplified collision integral are known as model kinetic equations.

The BGK model introduced by Bhatnagar, Gross and Krook (Bhatnagar *et al*., 1954) has been successfully employed for the modelling of rarefied gas flows and consists in approximating the collision term by

$$\Omega = \omega(f_{loc}^{M} - f) = \frac{1}{\tau}(f_{loc}^{M} - f)\,, \tag{1.27}$$

where ω is the collision frequency and τ is the relaxation time. The variable f_{loc}^{M} is the local equilibrium distribution function, defined as

$$f_{loc}^{M}(t,\vec{r},\vec{v}) = \frac{n(t,\vec{r})}{[2\pi RT(t,\vec{r})]^{3/2}}\, e^{-\frac{[\vec{v}-\vec{u}(t,\vec{r})]^2}{2RT(t,\vec{r})}}\,. \tag{1.28}$$

Boundary conditions must be provided in order to solve Eq. (1.25). The accommodation coefficients represent a convenient manner to describe the gas–surface interaction also under more rarefied conditions and need to be prescribed. Therefore, the determination of these coefficients as well as the influence of different factors is of great importance, since the gas–surface interaction plays a determinant role for rarefied flows in the entire rarefaction range.

1.3 MOLECULAR QUANTITIES

The limits of validity of the hypotheses of dilute gas, thermodynamic equilibrium and absence of statistical fluctuations were defined for a general gas in Section 1.1. In order to verify if these limits are attended for a specific gas under a particular condition, the mean molecular spacing, molecular diameter and mean free path must be calculated. Therefore, equations describing these quantities as functions of measurable macroscopic parameters of the flow must be provided. This can be accomplished by means of molecular analysis. However, it is not

the objective of the present work to give a comprehensive description of molecular theory, but to identify means of evaluating microscopic parameters of the gas necessary to characterize the flow. As a general assumption, the gas is consider to be composed of a single chemical species with all molecules having the same internal structure.

The easiest parameter to be obtained is the mean molecular spacing since its value can be directly related to the number density n through Eq. (1.2). In its turn, the number density can be calculated based on macroscopic parameters by the gas equation of state for an ideal gas:

$$P = nk_BT \ , \tag{1.29}$$

which is obtained by assuming a dilute gas in thermodynamic equilibrium. In this equation k_B is the Boltzmann constant ($k_B = 1.38064852 \times 10^{-23} J/K$).

On the other hand, both the molecular diameter, d, and the gas mean free path, λ, depend on the molecular interaction in a binary collision, that is, on the forces exerted by the molecules on each other. In fact, the magnitude of the interaction force depends on the distance between the molecules, as depicted in Figure 1.7. This force is weakly attractive when the molecules are at large distances and tends to zero as this distance increases. At short distances the force becomes highly repulsive and increases indefinitely as the molecules approach each other. The representation of the real behavior of the intermolecular force makes the molecular analysis considerably complicated. Accordingly, different simplified molecular models are generally used to describe this force interaction (Vicenti & Kruger, 1965).

Generally, the molecular models are described in terms of the potential, φ, related to the intermolecular force $\vec{F}_i$ (Gombosi, 1994):

$$\vec{F}_i(\vec{r}) = -\frac{d\varphi(\vec{r})}{dr}\hat{e}_r. \tag{1.30}$$

In this equation $\vec{r}$ is the relative position vector of two molecules and $\hat{e}_r$ is a unit vector in the same direction.

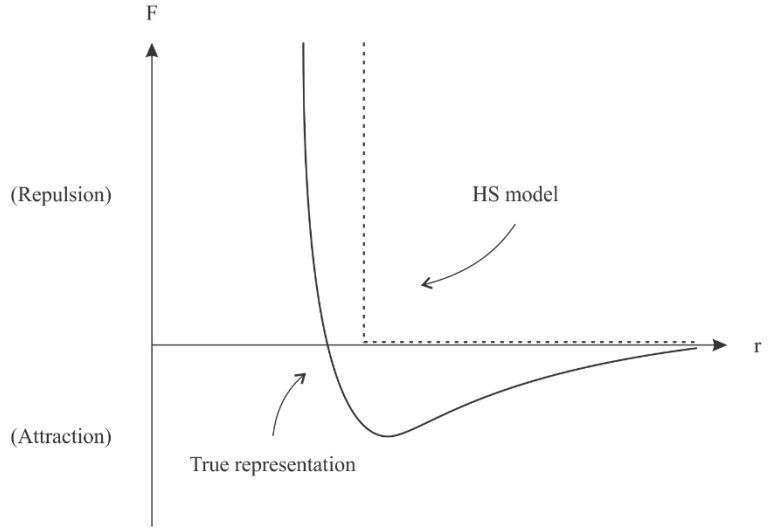

Figure 1.7 – Intermolecular force as a function of the distance between the molecules (Vicenti & Kruger, 1965).

The inverse power law (IPL) model is the most adopted molecular model and accounts only for the repulsive force between the molecules. According to the IPL model, the molecular potential is given by

$$\varphi = \frac{\kappa}{(\eta - 1) r^{\eta - 1}}\,, \tag{1.31}$$

where κ and η are constant parameters of the model. Variations of the IPL model are found according to the coefficients used to describe the molecular interaction. The simplest IPL model is the hard sphere (HS) model, in which $\eta \to \infty$ as depicted in Figure 1.7. The variable hard sphere (VHS) model proposed by Bird (1994) is an improvement of the HS model that considers the diameter of the molecules as a function of their relative velocity. The variable soft sphere (VSS) model differs from the VHS model by using a different expression for the angle of deflection of the molecules after the collision takes place. Finally, the Maxwell molecules (MM) model can also be considered a particular form of the IPL model with $\eta = 5$.

Alternatively, there are models that also take into account the attractive potential, such as the Leonard-Jones model:

$$\varphi = \frac{\kappa}{(\eta - 1)r^{\eta - 1}} - \frac{\kappa'}{(\eta' - 1)r^{\eta' - 1}}, \tag{1.32}$$

which has two additional constant parameters, κ' and η'. Other models, which also take into account the attractive-repulsive interaction, are the generalized hard sphere (GHS) and the variable sphere (VS) models (Colin, 2014). More recently, *ab initio* potentials, which do not rely on parameters extracted from experimental data, have been used (Sharipov, 2016).

Generally, the molecular diameter d is deduced through the comparison between the theoretical coefficient of viscosity, μ, obtained from the Chapman-Enskog expansion for the hard sphere model (HS), and its measured value in the real gas (Bird, 1994). The Chapman-Enskog expansion provides an approximation to the velocity distribution function f for systems that are not at equilibrium. It consists in adding a perturbation term to the local Maxwellian distribution function, given by Eq. (1.28), and allows the determination of transport coefficients of momentum and energy, that is, the viscosity coefficient μ and thermal conductivity k, respectively (Kremer, 2005).

If the hard sphere model (HS) is used, an expression can be obtained to evaluate the molecular diameter (Sharipov, 2016):

$$d_{HS} = \left(1.01603 \frac{5}{16\mu} \sqrt{\frac{m k_b T}{\pi}} \right)^{1/2}, \tag{1.33}$$

where the viscosity is a function of the temperature:

$$\mu_{HS} = \mu_0 \left(\frac{T}{T_0} \right)^{1/2}. \tag{1.34}$$

In these equations m is the molecular mass and μ_0 is the viscosity for a reference temperature T_0. Despite its simplicity, the HS model provides reasonable results. The main difficulty at the macroscopic level is the modeling of the viscosity dependence on temperature. This limitation can be overcome by the adoption of more sophisticated models such as the variable hard sphere model (VHS) developed by Bird (1994). The HS model is sufficient for the present analysis, providing a relationship between d and μ and avoiding the complexity of alternative formulations.

The last parameter to be obtained is the mean free path,

$$\lambda = \frac{\bar{c}}{\nu}\,, \tag{1.35}$$

which is expressed as the ratio between the mean thermal speed, $\bar{c}$, and the collision frequency of the molecules, ν.

From the kinetic theory, the mean thermal speed of the molecules can be expressed as $\bar{c} = \sqrt{8RT/\pi}$, while the collision frequency depends on the molecular interaction model. For IPL collision models, λ is generally written as

$$\lambda = k_\lambda \frac{\mu\sqrt{2RT}}{P}, \tag{1.36}$$

with k_λ defined in Table 1.1 according to the particular model considered, that is, hard sphere (HS), variable hard sphere (VHS), Maxwell molecules (MM) and variable soft sphere (VSS). The expression proposed by Maxwell (M) in 1879 for λ, Eq. (1.11), is frequently encountered in the literature (Colin, 2014), and also written in the form of Eq. (1.36) with its parameters given in Table 1.1. For the particular case in which $k_\lambda = 1$, λ is known as the equivalent mean free path λ_{eq}. The rarefaction parameter can be related to the Knudsen number as $\delta = k_\lambda / Kn$.

The parameter ω in Table 1.1 is associated with the law of viscosity derived using the Chapman-Enskog theory:

$$\mu = \mu_0 \left(\frac{T}{T_0}\right)^{\omega}\,, \tag{1.37}$$

where μ_0 is the viscosity associated with a reference temperature T_0. The parameter α from the VSS model (not to be confused with the tangential momentum accommodation coefficient α) comes from a correction term for the mean free path with respect to the estimation provided by the VHS model, that is:

$$\lambda_{VSS} = \frac{6\alpha}{(\alpha+1)(\alpha+2)}\lambda_{VHS}\,, \tag{1.38}$$

and its value is generally between 1 and 2.

Table 1.1 – Parameters associated with the collision models. Adapted from: Colin (2014).

Model	η	ω	k_λ
M	-	-	$\frac{\sqrt{\pi}}{2}$
HS	∞	$\frac{1}{2}$	$\frac{8}{5\sqrt{\pi}}$
VHS	η	$\frac{\eta+3}{2(\eta-1)}$	$\frac{(7-2\omega)(5-2\omega)}{15\pi}$
MM	5	1	$\frac{1}{\sqrt{\pi}}$
VSS	η	$\frac{\eta+3}{2(\eta-1)}$	$\frac{2\alpha(7-2\omega)(5-2\omega)}{5(\alpha+1)(\alpha+2)\sqrt{\pi}}$

1.4 OBJECTIVES

The design of many technological devices is currently associated with the modeling of flows in microscale. In the case of gases, the gas–surface interaction plays a determinant role and is affected by several aspects, many of which are not well understood or quantified. This work aims to characterize experimentally the gas–surface interaction in microflows induced by pressure gradients by means of the slip coefficients, σ_P and σ_{2P}, and the tangential momentum accommodation coefficient, α. Such results will reduce the lack of data in the literature related to the description of gas–surface interaction in rarefied gas flows, especially for flow conditions associated with leakage of gas inside refrigeration compressors. In this regard, attention is given to gases used in the refrigeration industry, such as R134a (1,1,1,2-Tetrafluoroethane) and R600a (Isobutane), and metallic materials, such as stainless steel, copper and brass. Two experimental setups were developed to measure the mass flow rates of rarefied gases through microchannels, with the proposition of an alternative version of the constant volume method, namely the dynamic constant volume technique.

1.5 STRUCTURE OF THE THESIS

A comprehensive literature review of studies on gas–surface interaction in microflows is presented in the next chapter (Chapter 2), so as to identify the main aspects of the flow and the main contributions of the thesis. Then, in Chapter 3, the experimental setups and procedure used to measure microflows are described in details. Also, analytical expressions and numerical data are introduced for comparison with the measurements. In Chapter 4, the results are discussed. Initially, slip and tangential momentum accommodation coefficients obtained for nitrogen flows through a microtube are compared with data from the literature, providing a validation of the experimental setup and procedure. Subsequently, the independence of the results with respect to the experimental setup and the adequacy of the quasi-stationary flow condition are assessed, followed by measurements of conductance. Moreover, slip and tangential momentum accommodation coefficients extracted from flows of nitrogen through a rectangular microchannel are also presented. Then, the influence of the gas chemical composition and surface characteristics (material and roughness) on the flow is analyzed. Finally, Chapter 5 summarizes the main conclusions of the investigation and proposes directions for further studies.

2 LITERATURE REVIEW

This chapter presents a review of studies about isothermal rarefied gas flows through microchannels with emphasis on the gas–surface interaction. Based on this review, the main contributions of this thesis are highlighted at the end of the chapter.

2.1 GAS FLOWS THROUGH MICROCHANNELS

In recent years, a number of works have been developed on the topic of gas flows through microchannels via theoretical and experimental approaches. Encouraged mainly by new developments of micro- and nano-electromechanical systems (MEMS and NEMS), many topics of interest have been investigated, such as mass and heat transfer in gas flows at microscale. Although the theoretical analyses allow to shed light on questions that are for now inaccessible from an experimental point of view, solid foundations for new phenomena are stablished more clearly when based also on experimental observation. In this sense, the main works, mainly of experimental nature, that comprise the analysis of rarefied gas flows through microchannels are underlined here. Particularly, the interest resides in analyzing the factors affecting the gas–surface interaction.

In order to simplify the models used to extract information on the gas interaction with the solid boundary, the flows studied have been mainly of isothermal nature, engendered by pressure gradients between the inlet and outlet of long channels with circular or rectangular cross sections. The microchannels have been manufactured in silicon and/or fused silica, in part because of the accessibility to silicon based manufacturing technologies, and the most used working fluids are nitrogen (N_2) and the noble gases helium (He) and argon (Ar). Given this brief overview, the influence of different parameters on the gas–surface interaction is analyzed separately in the following sections.

2.1.1 Gas effect

Many experimental investigations have been carried out on gas flows through microchannels, but few of them analyzed different gases using the same experimental apparatus, experimental method and theoretical model. Therefore, it becomes difficult to isolate the effect of the gas chemical composition on the gas–surface interaction when comparing results from different works. This section considers

investigations available in literature that make comparisons effectively possible.

As outlined by Agrawal and Prabhu (2008), many techniques have been put forward to measure slip and accommodation coefficients at gas-solid interfaces. The molecular beam technique was widely used in the 1960s and 1970s, while the spinning rotor gauge method was also adopted subsequently. Recent works have preferred to deduce these coefficients from measurements of mass flow rate and pressure drop in flows of gases through microchannels. Arguably, Arkilic *et al*. (2001) developed the first recent work with this aim. The authors measured the mass flow rates of argon (Ar), nitrogen (N_2) and carbon dioxide (CO_2) through a long rectangular microchannel, with length of 7.49 mm, manufactured in a silicon wafer with cross sectional dimensions of 1.33 μm in height and 52.3 μm in width, resulting in an aspect ratio (h/w) close to 0.026. The roughness along the channel length was smaller than 0.65 nm. Flows with different levels of rarefaction were considered by controlling the pressures upstream and downstream of the microchannel. The Knudsen number at the outlet of the channel, Kn_o, varied in the range from 0.03 to 0.44.

The value of the tangential momentum accommodation coefficient (TMAC), α, was inferred from each experiment by comparing the measurement with the theoretical prediction obtained from an analytical expression, which was derived from a perturbation expansion of the Navier-Stokes equation for the flow between parallel plates with first-order slip velocity boundary conditions at the walls. The HS molecular model was considered in the analysis and α was related to the first-order slip coefficient, σ_P, by means of Eq. (1.15). Since a first-order boundary condition was employed, α was the only unknown and could be determined directly for each experiment. For the majority of the experiments an incomplete accommodation ($\alpha < 1$) of the gas molecules at the walls was observed, with the value of TMAC ranging between 0.75 and 0.85 in most of the cases. The TMAC was virtually independent of the outlet Knudsen number, although an apparent increase was observed when Kn_o approached zero for N_2, as can be seen in Figure 2.1. Arkilic *et al*. (2001) justified this aspect of their results by the fact that the experiments were carried out from high to low Kn_o, suggesting that an "aging effect" in the channel could be the cause of this anomalous behavior. There was no comment on the influence of the gas chemical composition on the TMAC.

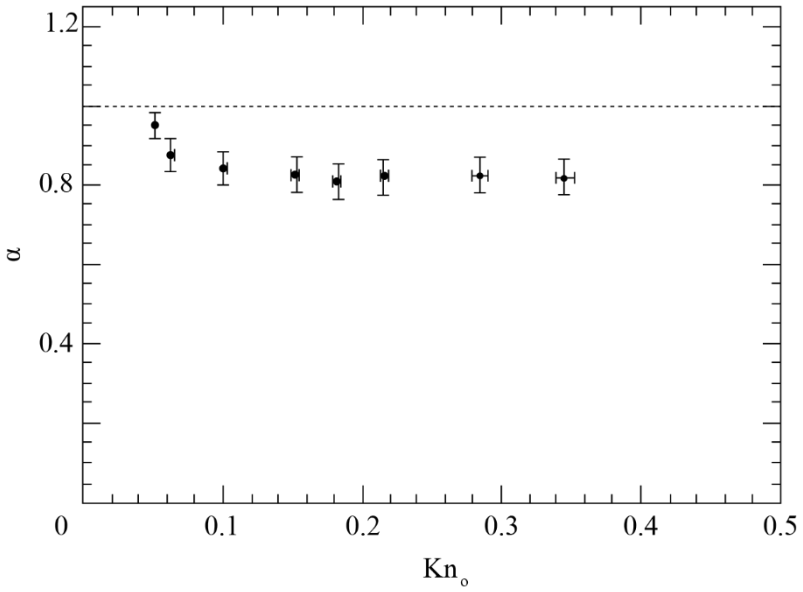

Figure 2.1 – TMAC values as a function of the outlet Knudsen number for flows of N_2 (Arkilic *et al*., 2001).

Maurer *et al*. (2003) carried out a similar analysis for He and N_2 in a rectangular microchannel 1 cm long with a cross section 1.14 μm deep and 200 μm wide ($h/w = 0.006$) etched in glass and covered with an atomically flat silicon wafer. The roughness of the glass was estimated to be 20 nm. An average Knudsen number, Kn_m, based on the mean pressure between inlet and outlet of the microchannel, was adopted as the reference parameter of the problem. In comparison with the work of Arkilic *et al*. (2001), a larger rarefaction range was investigated covering both the slip and transition flow regimes ($0.05 \leq Kn_m \leq 0.8$). The authors compared their measurements with predictions from a continuum-based approach using the Navier-Stokes equation with second-order velocity slip boundary condition for the parallel plates configuration. Again, the HS model was adopted to determine the mean free path and Eq. (1.15) was adopted to relate α to σ_P.

The experimental results were presented in terms of the dimensionless mass flow rate, defined as

$$S = \frac{12 Q_v \mu P_o L}{\Delta P P_m w h^3} \ , \tag{2.1}$$

where Q_v is the volumetric flow rate, μ is the gas viscosity, P_o is the outlet pressure, L is the microchannel length, ΔP is the pressure difference applied, P_m is the average pressure between inlet and outlet of the microchannel, w is the channel width and h is the channel height. The theoretical expression for S was written as

$$S = 1 + 6A_1 Kn_m + 12A_2 Kn_m^2 , \tag{2.2}$$

where A_1 and A_2 were obtained by fitting the experimental data (Figure 2.2). By using Eq. (1.15) to relate α and σ_P, the following expression was derived to calculate α:

$$\alpha = \frac{2}{A_1 + 1} \ . \tag{2.3}$$

The results of Maurer *et al*. (2003) revealed values of TMAC close to 0.9 for He and N_2 flows. They also defined $Kn_m = 0.3 \pm 0.1$ as the upper limit value of the slip flow regime for flows through rectangular microchannels and showed that for greater values of Kn_m a second-order boundary condition was more effective to describe the flow than a first-order one. It should be mentioned that the theoretical model considered the same TMAC value for the lower and upper walls of the microchannel, which is not necessarily true since these walls were made of different materials. The authors also extracted the TMAC values considering a first-order velocity slip boundary condition in the same manner as Arkilic *et al*. (2001) by defining $A_2 = 0$ in Eq. (2.2). Values of α were obtained directly for each experiment and the same trend reported by Arkilic *et al*. (2001) was observed, with α decreasing with the increase of Kn_m (Figure 2.3). However, Maurer *et al*. (2003) observed a larger scatter of the data for small values of Kn_m and hence considered it unsafe to draw conclusions about this subject. In this sense, this anomalous behavior could be associated with limitations of the instruments employed.

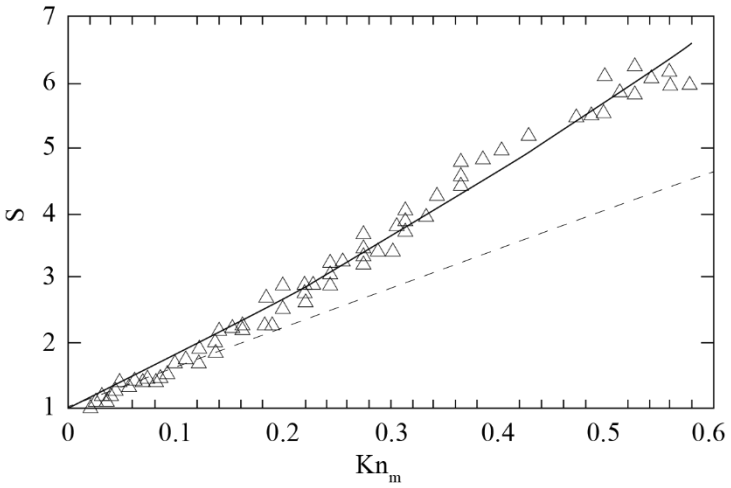

Figure 2.2 – Dimensionless mass flow rate as a function of Kn_m for flows of N_2. First- (– –) and second-order (—) models (Maurer *et al*., 2003).

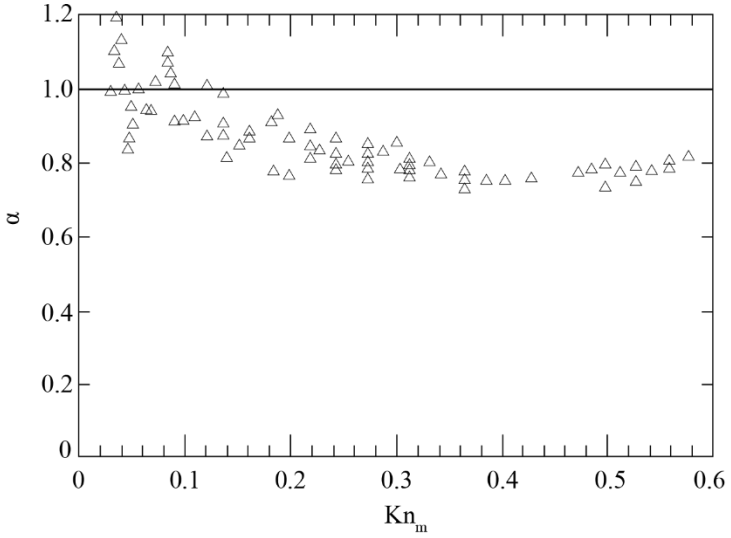

Figure 2.3 – TMAC values as a function of Kn_m for flows of N_2 (Maurer *et al*., 2003).

Colin *et al*. (2004) proposed an analytical model based on the Navier-Stokes equation with first- and second-order velocity slip boundary conditions, following the form proposed by Deissler (1964), to take into account three-dimensional effects of a rectangular cross section microchannel. Results of this model for flows of helium (He) and nitrogen (N_2) were compared to experimental data obtained for microchannels etched in silicon wafers and covered with Pyrex with different aspect ratios ($0.011 \leq h/w \leq 0.087$). The channels had a length of 5 mm. For the smaller aspect ratios, a group of microchannels with the same dimensions were arranged in parallel to obtain a sufficiently large flow rate that could be measured with accuracy. Values of Knudsen number as high as 0.47 were obtained at the channel outlet and second-order slip velocity boundary conditions proved to be valuable for $Kn_o \leq 0.25$. The best fit of the experimental data for both He and N_2 was found by specifying $\alpha = 0.93$.

The first attempt to analyze experimentally the gas–surface interaction in a single microtube considering different gases can be attributed to Ewart *et al*. (2007a). In their work, mass flow rates of He, N_2 and Ar were measured in a 25.2 μm diameter silica microtube in the Kn_m range from 0.003 to 0.309. The microtube length was 5.3 cm and the roughness was estimated to be smaller than 0.1% of the diameter. The theoretical model used to extract TMAC values from experimental data was based on the Navier-Stokes equation with first- and second-order slip velocity boundary conditions. As in Maurer *et al*. (2003), the authors presented the results in terms of the dimensionless mass flow rate S, which for a channel with circular cross section was defined as

$$S = \frac{128\mu RTL}{\pi D^4 \Delta P P_m}\dot{m} \ , \tag{2.4}$$

where $\dot{m}$ stands for the absolute mass flow rate and D represents the microtube diameter. In this case, the theoretical model was written as

$$S = 1 + A_1 Kn_m + A_2 Kn_m^2 \ , \tag{2.5}$$

and A_1 was related to σ_P by the following expression:

$$A_1 = \frac{\sigma_P}{8k_\lambda}. \tag{2.6}$$

The slip coefficient, σ_P, was related to TMAC, α, via Eqs. (1.15) and (1.16) and the mean free path was calculated considering the VHS molecular model. The coefficients A_1 and A_2 were determined by fitting the experimental data with the same procedure proposed by Maurer *et al.* (2003).

Ewart *et al*. (2007a) concluded that for the gases and rarefaction range considered in the measurements, a second-order slip boundary condition was more suitable (Figure 2.4). Also, the relative weight of the second-order effect increased with the increase of the molecular mass, although it was not significantly affected by the molecular internal structure. Even when different definitions of the slip coefficient were considered, an incomplete accommodation was always observed for the gases studied, with $\alpha_M = 0.914 \pm 0.009$, 0.908 ± 0.041 and 0.871 ± 0.017, for He, N_2 and Ar, respectively. Alternatively, $\alpha_L = 0.986 \pm 0.009$, 0.981 ± 0.041 and 0.942 ± 0.017, for He, N_2 and Ar, respectively. In this respect, the value of TMAC decreased when the molecular weight increased for monoatomic gases.

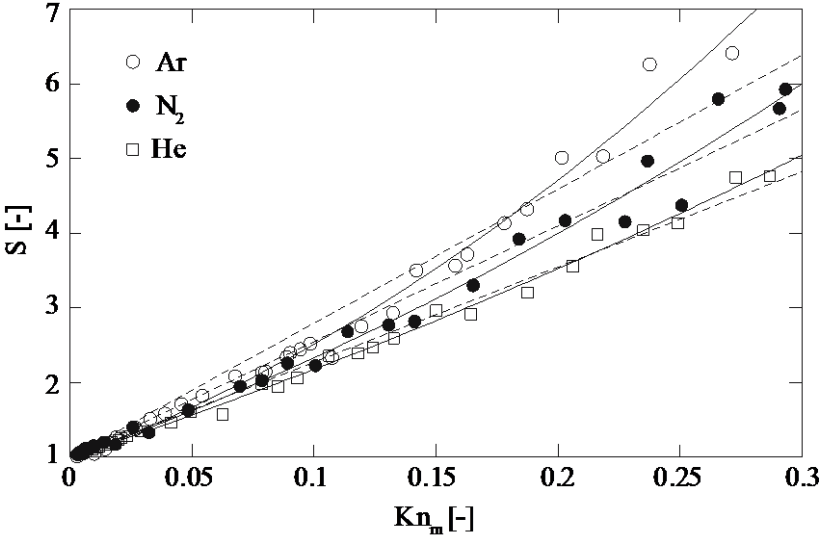

Figure 2.4 – Dimensionless mass flow rate of N_2, Ar and He considering first- (– –) and second-order (—) models (Ewart *et al*., 2007a).

A wider rarefaction range was explored in rectangular microchannels by Graur *et al*. (2009), considering flows of He, N_2 and Ar in a single silicon microchannel with length of 9.39 mm and cross sectional dimensions of 9.38 μm in height and 492 μm in width ($h/w = 0.019$) up to an average Knudsen number of 30. Results obtained previously for He in the same experimental setup (Ewart *et al*., 2007b) were gathered to widen the scope of the analysis. The surface roughness was estimated to be smaller than 20 nm. Since a very extensive rarefaction range was considered, different theoretical approaches were required. For $0 \leq Kn_m \leq 0.3$, a model based on the Navier-Stokes equation for flows between parallel plates with both first- and second-order slip velocity boundary conditions was used. The authors employed the same fitting approach proposed by Maurer *et al*. (2003) to extract the slip and accommodation coefficients. The mean free path was calculated with the Maxwell model (M) and Eq. (1.17) was used to related α and σ_P. From the analysis of the results, the second-order approach was considered to be more appropriate. However, independently of the chosen approach the value of TMAC was seen to decrease with the increase of the molecular weight. Values of first-order TMAC equal to 0.933 ± 0.003, 0.889 ± 0.004 and 0.848 ± 0.008 were obtained for He, N_2 and Ar, respectively. Second-order values of TMAC were only estimated for N_2 and Ar, being equal to 0.956 ± 0.005 and 0.910 ± 0.028, respectively.

Graur *et al*. (2009) also compared theoretical values of the reduced mass flow rate, calculated from two kinetic models, with experimental data in the whole rarefaction range, characterized by the mean rarefaction parameter, δ_m (Figure 2.5). The reduced mass flow rate was defined by

$$G = \frac{L\sqrt{2RT}}{h^2 w \Delta P}\dot{m} \cdot \tag{2.7}$$

The first model (Sharipov, 1999) considered complete diffuse reflection at the walls but took into account the finite width of the microchannel, while the second model (Loyalka *et al*., 1976) neglected the effect of the lateral walls, but considered the incomplete accommodation of the molecules. The authors concluded that as rarefaction increases ($\delta_m \to 0$), the effect of the incomplete accommodation of molecules at the walls is manifested first. Accordingly, the model of Loyalka *et al*. (1976) better fits the experimental data in the lower rarefaction range. As rarefaction is further increased, for δ_m close to 1, a departure is observed between the measurements and both theoretical models. In this range of δ_m the

influences of both the finite width and incomplete accommodation of the molecules cannot be disregarded. However, as rarefaction increases even further, with δ_m near 0.1, the effect of the finite width of the microchannel becomes predominant and the experimental data approaches the curve defined by the model of Sharipov (1999). It should also be noted the large dispersion of the experimental data in the whole rarefaction range, especially for small values of δ_m.

By comparing experimental and theoretical results, Graur *et al*. (2009) estimated the TMAC for He to be close to 1, while for N_2 and Ar the values were 0.96 and 0.94, respectively. Independently of the Knudsen range analyzed and the theoretical approach considered, a tendency of increasing the TMAC was verified when the molecular mass was decreased. The authors proposed two possible explanations for this tendency: a) when a lighter molecule hits the wall its incoming direction is more easily changed since its momentum is smaller; b) the asperities of the wall can hold and then scatter more easily lighter molecules because they are usually smaller. In both circumstances, the momentum of the reflected molecules is more influenced by the momentum of the wall than by its incident momentum, resulting in values of TMAC closer to unity. Although verified for the three gases analyzed, Graur *et al*. (2009) did not conclude this behavior would hold whatever the conditions (wall material, surface roughness or even the gas). In fact, they considered that other parameters, such as the internal structure of the gas molecule and the characteristic length of the intermolecular potential, could also affect the TMAC. Second-order effects also decreased in gases with smaller molecular mass. Furthermore, as in other works, TMAC values significantly smaller than unity were found, indicating that the full accommodation assumption may not be satisfactory to describe the gas–surface interaction. Finally, based on the comparison with the results of Ewart *et al*. (2007a), the authors also concluded that second-order effects are more important in microtubes than in rectangular microchannels.

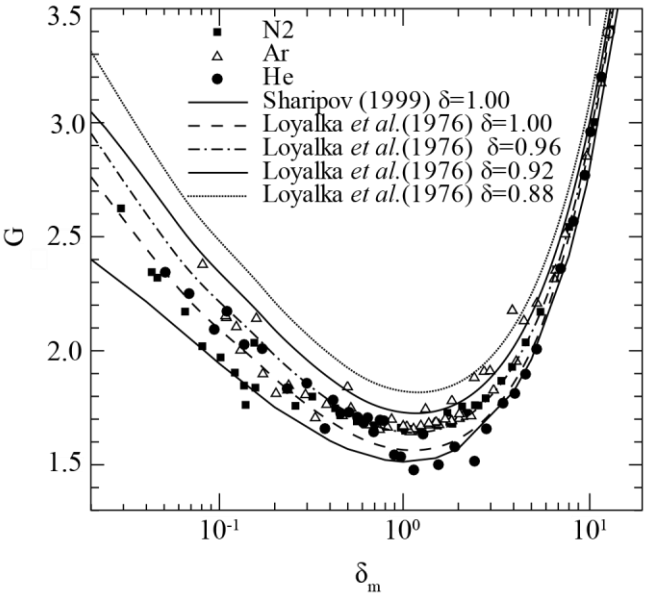

Figure 2.5 – Experimental reduced mass flow rate and theoretical curves considering the finite width of the channel (Sharipov (1999)) and the incomplete accommodation (Loyalka *et al*. (1976)) (Graur *et al*., 2009).

Perrier *et al*. (2011) analyzed flows of different gases – helium (He), nitrogen (N_2), argon (Ar) and xenon (Xe) – through single fused-silica microtubes with internal diameters of 25, 50, and 75 μm from hydrodynamic to near free molecular flow regime ($0.003 \leq Kn_m \leq 30$). The microtube with smaller length was 1.82 cm long. The authors compared measurements of mass flow rate with results obtained from analytical expressions based on the Navier-Stokes equation with first- and second-order slip velocity boundary conditions for slightly rarefied flows ($0.003 \leq Kn_m \leq 0.3$). The mean free path was calculated using the VHS model and Eq. (1.17) was adopted to related α and σ_P. Again, the value of α was determined by curve-fitting the measurements of the dimensionless mass flow rate S. The second-order results for the 50 μm microtube indicated $\alpha = 1.000 \pm 0.019, 0.961 \pm 0.005, 0.954 \pm 0.010$ and 0.954 ± 0.015 for He, N_2, Ar and Xe, respectively. It was also noted that when slip models were considered, the second-order term increased with the surface curvature, that is, in smaller channel diameters.

In the remaining rarefaction range considered, Perrier *et al*. (2011) compared the experimental measurements with results obtained from the

solution of the BGK kinetic equation. These comparisons allowed the determination of the slip and accommodation coefficients in the whole rarefaction range and the analysis of these results indicated that an incomplete accommodation ($\alpha < 1$) generally occurs on a silica surface, with a trend to increase α with the decrease of the gas molecular mass (Figure 2.6). This behavior was seen to be more important for gases with smaller molecular masses, despite the large dispersion observed in the experimental data.

Yamaguchi *et al*. (2011) analyzed flows of argon (Ar), nitrogen (N_2) and oxygen (O_2) through deactivated fused-silica microtubes with nominal inner diameter of 320 μm and 530 μm, with average Knudsen numbers up to 0.3. The lengths of the microtubes were 59.25 mm and 46.95 mm, respectively. In order to extract the value of TMAC for the different gases, the authors used the same analytical expression and procedure employed by Ewart *et al*. (2007a) with a second-order slip velocity boundary condition. The mean free path was calculated using the VHS model and the authors considered three different expressions, given by Eqs. (1.15)-(1.17), for the relation between α and σ_P. The results clearly indicated TMAC values smaller than unity for Ar, N_2 and O_2, regardless the equation used for extracting the TMAC, as indicated in Table 2.1. In addition, the authors found small effect of gas species on the TMAC, but pointed out that measurements should be carried out for lighter and heavier gases to allow a conclusion on this issue.

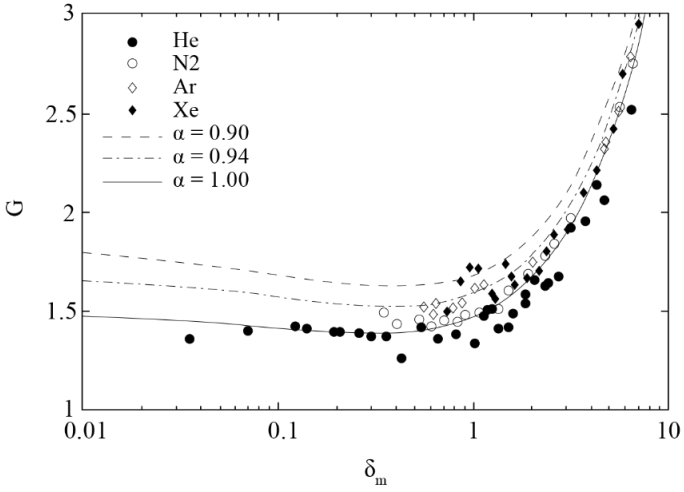

Figure 2.6 – Experimental reduced mass flow rate and theoretical curves for the 50 μm microtube (Perrier *et al*., 2011).

The results for tangential momentum accommodation coefficient (TMAC), α, obtained by considering a diffuse-specular interaction are summarized in Table 2.1. Apart from these results, Sharipov (2003) determined the TMAC, α, for the Cercignani-Lampis scattering model by comparing numerical data of mass flow rate obtained on the basis of the S-model kinetic equation with experimental data provided by Porodnov *et al*. (1974) for different gases through packets of glass capillaries. Since the Poiseuille flow has a weak dependence on the accommodation coefficient of kinetic energy due to the normal velocity, α_n, it was assumed that $\alpha_n = 1$. The results indicated $\alpha = 0.908 \pm 0.003$ for He, 0.893 ± 0.003 for Ne, 0.969 ± 0.007 for Ar, 0.985 ± 0.007 for Kr and 1 for Xe. Values of TMAC extracted by Porodnov *et al*. (1974) based on the diffuse-specular gas-surface interaction model were $\alpha = 0.895$ for He, 0.865 for Ne, 0.927 for Ar, 0.995 for Kr and 1.010 for Xe. Porodnov *et al*. (1974) also provided data for diatomic gases and CO_2. For these gases, they found $\alpha = 0.957$ for H_2, 0.934 for D_2, 0.925 for N_2 and 0.993 for CO_2. Particularly, CO_2 presented an almost complete accommodation ($\alpha \cong 1$).

The works discussed up to this point considered only single gases. Instead, Pitakarnnop *et al*. (2010) studied flows of He, Ar and also a 30% He – 70% Ar mixture through a package of 45 rectangular microchannels positioned in parallel. The microchannels had nominal dimensions of 1.88 μm × 21.2 μm and were etched in a silicon wafer with a length of 5 mm. The microchannel was covered with Pyrex, with typical roughness between 50 and 80 Å. The analysis comprised flows with Kn_o up to 0.034, 0.095 and 0.038 for He, Ar and He-Ar mixture, respectively. Predictions of the mass flow rate following a continuum approach with second-order velocity slip boundary conditions and a kinetic model were used to extract further information from the experimental data.

In the continuum model, the binary mixture was treated as a single gas and its properties were evaluated from the proportion of each gas. The mean free path was calculated based on the Maxwell model (M) and the relation between α and σ_P was based on Eq. (1.15) multiplied by a corrective coefficient proposed by Hadjiconstantinou (2003). On the other hand, the McCormack model (McCormack, 1973) was used to treat the mixture of gases in the kinetic model. Independently of the theoretical model adopted, a better fit of the experimental data was achieved with $\alpha = 1$ for all gases, including the He-Ar mixture (Figure 2.7). The authors suggested further studies of different mixtures and concentrations of gases, and a wider range of rarefaction conditions. They also pointed out

that the hypothesis adopted in the models that the concentration of the species is the same in the reservoirs and in the microchannels would probably not hold for more rarefied flows.

Table 2.1 – TMAC values for different gases. First-order results are shown in parentheses.

	Gas	α^M	α^L	α^S
		Microchannel		
a	Ar, N_2, CO_2	(0.75-0.85)		
b	He	0.91 ± 0.03		
	N_2	0.86 ± 0.03		
c	He, N_2	0.93		
d	He			(0.933 ± 0.003)
	N_2			0.956 ± 0.005 (0.889 ± 0.004)
	Ar			0.910 ± 0.028 (0.848 ± 0.008)
		Microtube		
e	He	0.914 ± 0.009	0.986 ± 0.009	
	N_2	0.908 ± 0.041	0.981 ± 0.041	
	Ar	0.871 ± 0.017	0.942 ± 0.017	
f	He			1.000 ± 0.019 (0.967 ± 0.010)
	N_2			0.961 ± 0.005 (0.899 ± 0.009)
	Ar			0.954 ± 0.010 (0.878 ± 0.013)
	Xe			0.954 ± 0.015 (0.882 ± 0.011)
g	N_2	0.845 ± 0.038	0.913 ± 0.041	0.906 ± 0.041
	O_2	0.836 ± 0.035	0.904 ± 0.038	0.897 ± 0.038
	Ar	0.837 ± 0.032	0.904 ± 0.034	0.898 ± 0.034

[a] Arkilic *et al*. (2001), silicon, roughness below 0.65 nm.
[b] Maurer *et al*. (2003), glass and silicon, estimated roughness 20 nm.
[c] Colin *et al*. (2004), Pyrex and silicon.
[d] Graur *et al*. (2009), silicon, roughness below 20 nm.
[e] Ewart *et al*. (2007a), fused silica, roughness below 0.1%.
[f] Perrier *et al*. (2011), fused silica, $D = 50\mu m$, roughness below 20 nm.
[g] Yamaguchi *et al*. (2011), deactivated-fused silica, $D = 530\mu m$.

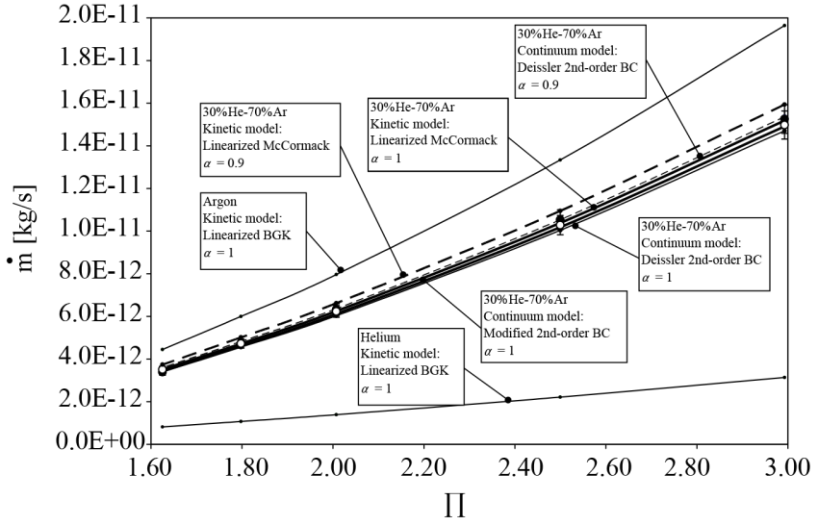

Figure 2.7 – Mass flow rate ($\dot{m}$) versus pressure ratio (Π) for a mixture of He (30%) and Ar (70%). Measurements at the inlet (●) and outlet (○) of the microchannel (Pitakarnnop *et al*., 2010).

2.1.2 Material effect

Although most studies in microfluidics have been carried out in microchannels manufactured in silicon or silica, as verified in the last section, there are some investigations about the influence of the material on the gas–surface interaction. For example, Hadj Nacer *et al*. (2011) measured mass flow rates of He, N_2 and Ar through a rectangular silicon microchannel with height of 27.84 μm, width of 52.23 μm ($h/w = 0.53$), and length of 15.07 mm, covered with a thin gold coating of average roughness of 0.87 nm. The measurements were performed for a wide rarefaction range, that is, $0.0025 \leq Kn_m \leq 26.2$, employing the same experimental setup and procedure of Ewart *et al*. (2007a) and Graur *et al*. (2009).

Theoretical results from a continuum model with first-order slip velocity boundary conditions and from a kinetic model, both accounting for the finite width of the microchannel, were used for comparison. Equation (1.17) was used to relate α to σ_P in the continuum model. Values of TMAC were extracted from the experimental data for $Kn_m \leq 0.1$ through comparisons with the results of the continuum model, being equal to 0.868 ± 0.007, 0.845 ± 0.004 and 0.853 ± 0.007 for He, N_2 and Ar,

respectively. When comparing the measurements to predictions given by the kinetic model in the whole rarefaction range, the authors observed that α was within the 0.8–1.0 range (Figure 2.8), in accordance with results extracted from the continuum model. Although the novelty of the material used for the microchannel was introduced, the adopted manufacturing process produced cross sectional geometries very poorly defined, as shown in Figure 2.9.

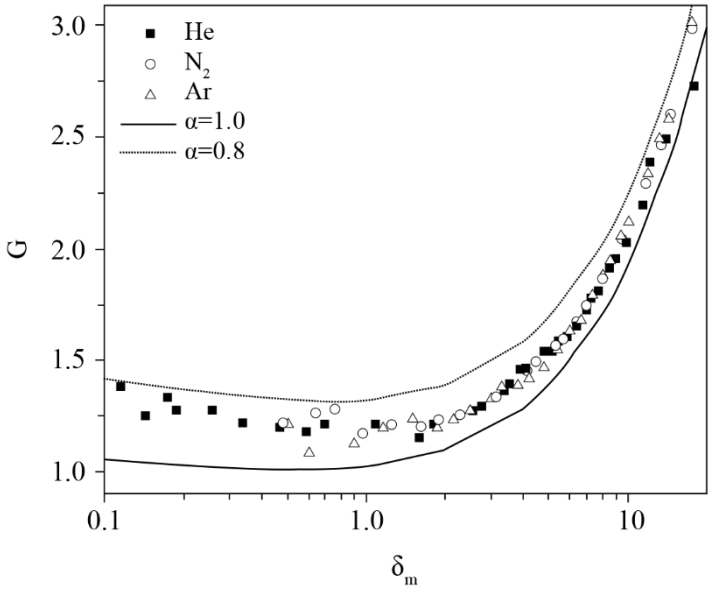

Figure 2.8 – Experimental reduced mass flow rate (symbols) compared to numerical predictions (lines) (Hadj Nacer *et al*., 2011).

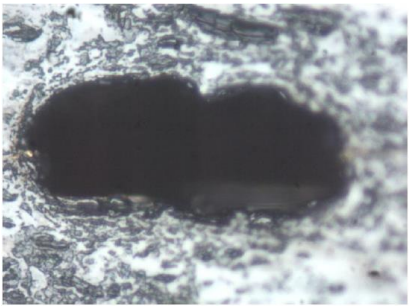

Figure 2.9 – Cross sectional view of the microchannel (Hadj Nacer, 2012).

By using the experimental setup developed by Yamaguchi *et al*. (2011), Yamaguchi *et al*. (2012) measured the values of TMAC for Ar, N_2 and O_2 in commercially available stainless steel microtubes with nominal diameter of 0.29 mm. The results were obtained for Kn_m up to 0.32. The authors aimed to verify the assumed complete accommodation of gases ($\alpha = 1$) on machined and non-treated metal surfaces, often called engineering surfaces. A continuum model with second-order velocity slip boundary condition was adopted to describe the flows and Eqs. (1.15) and (1.17) were used to extract α from measurements of σ_P. The experiments were conducted in three different microtube samples and α^M and α^S for all gas species were close to 0.89 and 0.95, respectively, even when different samples were compared. The values of TMAC smaller than unity suggested an incomplete accommodation at the wall even for engineering surfaces. Moreover, the gas species had a negligible effect on the TMAC with this type of surface, differently from the tendency observed in previous works for non-metal surfaces. Nevertheless, the authors recommended further measurements to confirm this trend because the difference between the molecular weights of the gases used in their study was too small.

Hadj Nacer *et al*. (2014) presented an interesting comparative analysis for flows of He, N_2, Ar and CO_2 through two stainless steel microtubes, one of which had its internal surface covered by silica-based coating. The microtubes had internal nominal diameters of 250 μm and the roughness levels were not measured. An analytical expression based on the solution of the Navier-Stokes equation considering first-order slip velocity boundary condition was used to extract the value of the TMAC for Kn_m up to 0.1. In this case, the VHS model was used to determine the mean free path and Eq. (1.17) to extract α from values of σ_P.

The results confirmed that for monoatomic gases the TMAC decreases when the molecular mass increases, as also observed in Ewart *et al*. (2007a), Graur *et al*. (2009) and Perrier *et al*. (2011). The values of TMAC were equal to 0.930 ± 0.003 for He, 0.881 ± 0.003 for N_2, 0.883 ± 0.004 for Ar and 0.951 ± 0.004 for CO_2 for the stainless steel microtube with coating. Since for monoatomic gases the molecular mass is directly related to the size of the spherical molecule, the authors suggested that the large sizes could increase the amount of specular reflection by minimizing the effects of both the wall asperity and the wall structure (roughness and atomic arrangement). Contrarily, for the polyatomic molecules the authors pointed out that the non-spherical structure associated with the corresponding internal degrees of freedom can favor a diffusive

reflection. This effect was more pronounced for CO_2 in comparison with N_2.

Regarding the effect of the surface material, the results showed a significant dependence although the roughness of the surface may also have contributed to the differences found. The stainless steel surface without coating reduced the effect of the gas, providing TMAC values in a narrower range around 0.9. The authors also compared the measurements obtained in a wider rarefaction range ($10^{-4} \leq Kn_m \leq 5$) with numerical results from the linearized S-model kinetic equation (Shakhov, 1968). The S-model is an alternative approximation to the collision term, as the BKG model, which provides a correct expression for the Prandtl number (Sharipov, 2016). The authors inferred new TMAC values from this comparison and found the values in agreement with those obtained in the slip flow regime. However, a significant deviation was observed between experimental and numerical results in both microtubes as the rarefaction increased ($\delta_m \rightarrow 0$) (Figure 2.10).

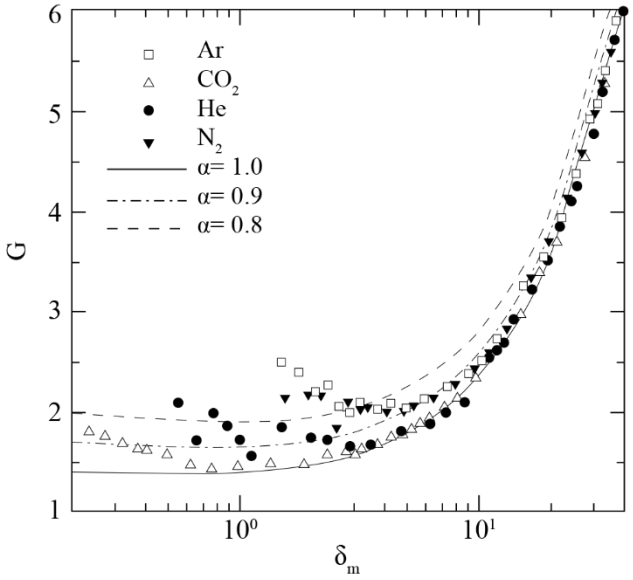

Figure 2.10 – Experimental reduced mass flow rate (symbols) compared to numerical predictions (lines) for stainless steel microtube with coating (Hadj Nacer *et al*., 2014).

2.1.3 Surface effects

The state of the surface plays a determinant role in the gas–surface interaction. In fact, as mentioned by Agrawal and Prabhu (2008), the surface roughness, temperature and even adsorbed materials can affect the TMAC. Despite its importance, few experimental investigations of this phenomenon are available, since the characterization of such parameters and the measurement of their effects are very difficult.

Most studies on the effect of surface roughness have been carried out via numerical simulation, with the surface topography being described by means of regular or random patterns of geometric elements (Cao *et al*., 2006; Lilly *et al*., 2007; Chai *et al*., 2008; Rovenskaya, 2013) or using fractal geometry (Zhang *et al*., 2012b; Yan *et al*., 2015; Deng *et al*., 2016). Also, different flow models have been considered, including the Navier-Stokes equation with slip velocity boundary conditions at the walls (Yan *et al*., 2015), the Boltzmann equation (Chai *et al*., 2008; Zhang *et al*., 2012b; Rovenskaya, 2013; Yan *et al*., 2015; Deng *et al*., 2016) and molecular dynamics (Cao *et al*., 2006). Most of such studies suggest that the surface roughness has a significant influence on the flow even in the laminar flow regime and that the arithmetic average surface roughness does not suffice to characterize the surface. However, some conflicting results have also been reported. For example, some authors (Zhang *et al*., 2012b; Yan *et al*., 2015; Deng *et al*., 2016) advocate that the effect of the surface roughness increases as the rarefaction level increases, while others predicted the opposite behavior (Chai *et al*., 2008; Rovenskaya, 2013). Clearly, accurate experimental measurements would provide a better understanding of these aspects.

From an experimental point of view, some works can be highlighted. In particular, Turner *et al*. (2004) investigated the effects of surface roughness, rarefaction and compressibility on laminar gas flows through rectangular microchannels etched in silicon wafers (relative roughness from 0.1% to 6%) capped with glass, and hydraulic diameters between 5 and 96 μm and length $L = 30\ mm$. The authors analyzed flows of He, N_2 and air and showed that the influence of the surface roughness on the friction factor is insignificant for both continuum and slip flow regimes ($Kn \leq 0.11$), with differences within the uncertainty range. No reference was made to the value of the TMAC.

Lilly *et al*. (2007) also made some experiments to measure the mass flow rates of He and N_2 through rectangular microchannels ($h = 150\ \mu m,\ w = 1\ cm,\ L = 1.5\ cm$), manufactured in silicon and with controlled surface roughness in order to validate their numerical model.

Flows in the transition regime were analyzed in microchannels with atomically smooth, triangular patterned, and square patterned surfaces (Figure 2.11). Higher slip was observed for the smooth surface (Figure 2.12), though no reference to the variability of the TMAC with the surface roughness was reported.

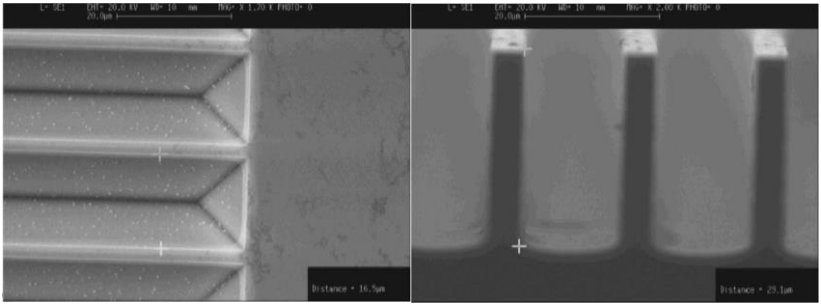

(a) (b)

Figure 2.11 – SEM pictures of (a) the end of the triangular textures from above and (b) the view along cleaved square textures from side (Lilly *et al*., 2007).

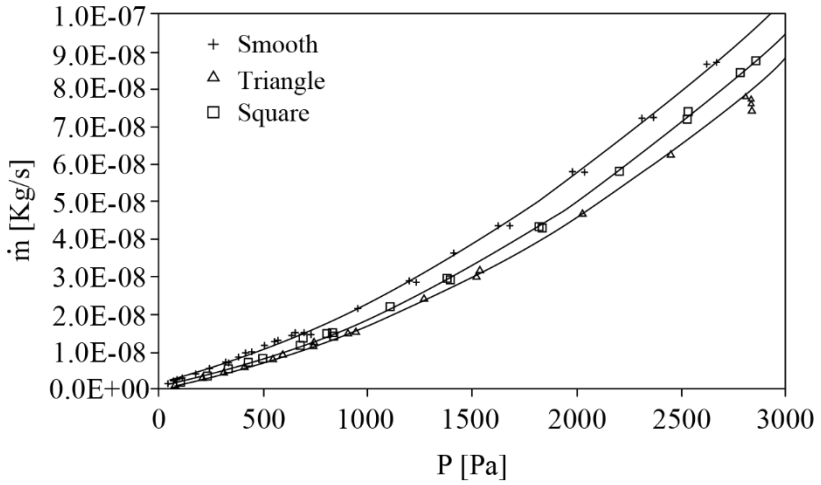

Figure 2.12 – Experimental results of mass flow rate for flows of He considering textured geometries (Lilly *et al*., 2007).

More elaborated experimental setups were also built to facilitate the control of the surface conditions inside the channels and reduce the uncertainties associated with the measurements. For example, Blanchard and Ligrani (2007) determined the TMAC for flows of He and air over PEEK surfaces with different roughness levels and $0.0025 \leq Kn \leq 0.031$. An original experimental setup was also built to analyze rotation-induced flows in C-shaped fluid chamber passages formed between a rotating disk and a stationary surface (Figure 2.13). The chamber height was adopted as the characteristic length to determine Kn, and its value ranged from 6.85 to 29.2 μm. The average roughness was determined to be within the range from 0.01 to 1.1 μm.

With the method proposed, the TMAC was determined from pressure measurements for a no-flow condition, in which the inlet and outlet ports were closed, and theoretical results based on the solution of Navier-Stokes equation with first-order slip velocity boundary conditions.

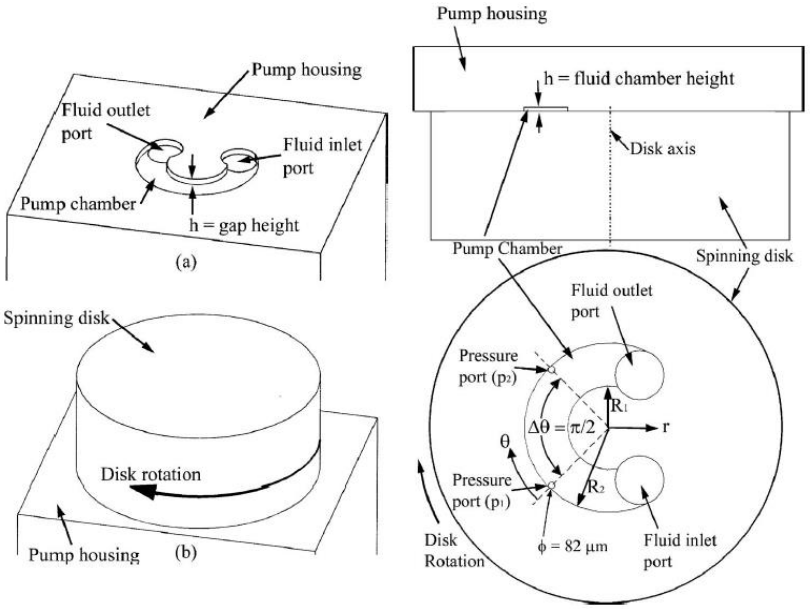

(a) (b)

Figure 2.13 – (a) External and internal views of the single-disk viscous pump and (b) fluid chamber configuration (Blanchard & Ligrani, 2007).

Equation (1.15) was used to relate α and σ_P, and an expression for the pressure difference, ΔP, in terms of α was derived:

$$\Delta P = \frac{-3\mu\omega\Delta\theta\left({R_2}^2 - {R_1}^2\right)}{h^2 \ln(R_1/R_2)[1 + 6(\beta_w \lambda/h)]}, \tag{2.8}$$

where μ is the fluid viscosity, ω is the angular speed of the spinning disk, $\Delta\theta$ is the circumferential angle between the pressure measurement ports, R_1 and R_2 are inner and outer radii of the C-shaped fluid passage, h is the chamber height, λ is the mean free path and $\beta_w = (2 - \alpha)/\alpha$. During the experiments, the Knudsen number was varied by changing the chamber height, h, and the mean pressure in the chamber.

The authors claimed that TMAC values could be obtained with reduced uncertainty compared to procedures that rely on the analysis of stationary flows in tubes and channels, since the uncertainty associated with the mass flow rate was eliminated and the uncertainty related to the channel height was reduced. An uncertainty of 2% in the measurements of pressure difference was attributed to leak of gas in the test section.

The results indicated that the TMAC decreases considerably as the channel roughness increases when the channel height is measured from the peaks of the roughness elements (Figure 2.14). This was attributed to the fact that the resulting TMAC takes into account slip due to rarefaction at gas–solid interfaces as well as slip due to shear at gas–gas interfaces located in the volumes of gas confined between adjacent roughness elements. However, the authors observed that the TMAC is largely independent of the surface roughness when the channel height is measured from the midway between the crests and troughs of the roughness elements, with $\alpha = 0.885$ for air and $\alpha = 0.915$ for He. Therefore, they concluded that slip is mostly due to rarefaction when the channel height is appropriately defined.

An alternative experimental approach was also used by Yoshida *et al.* (2010) to analyze the effect of surface material and roughness on flow conductance, C, between two parallel disks under rarefied conditions ($0.1 \leq Kn \leq 1000$). As will be detailed in Section 3.1.2, following the analogy with Ohm's law, one can relate the pressure difference (ΔP) between the ends of the microchannel to the electric potential, the flow throughput, Q, to the current and the conductance, C, to the inverse of the electric resistance, that is,

$$Q = C\Delta P\ . \tag{2.9}$$

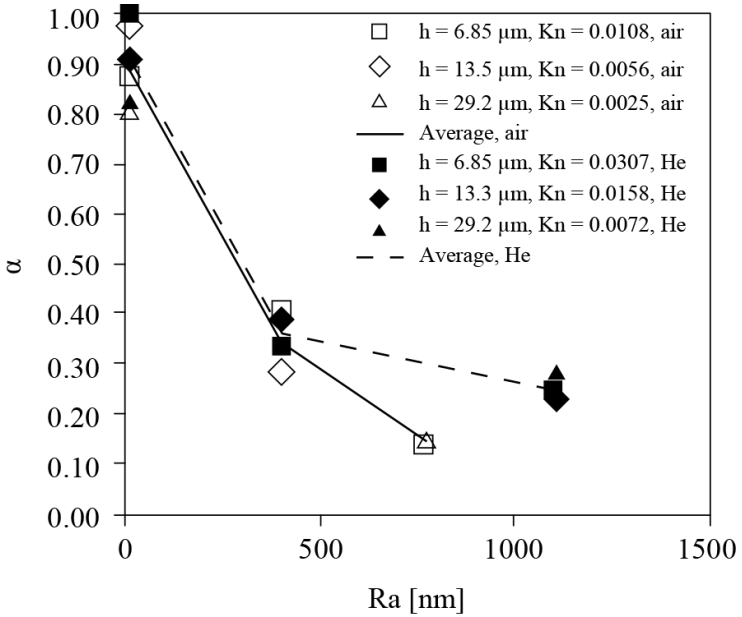

Figure 2.14 – TMAC as a function of the surface roughness when channel height is measured from the peaks of the roughness elements (Blanchard & Ligrani, 2007).

Flows of hydrogen (H_2), helium (He), nitrogen (N_2) and argon (Ar) were investigated over eleven surfaces: polished stainless steel, roughly polished stainless steel, quartz, titanium, copper, aluminum, alumina with smooth surface, alumina with rough surface, stainless steel with gold coating, stainless steel with platinum coating and stainless steel with diamond-like carbon (DLC) coating. The conductances for H_2, N_2 and Ar considering polished stainless steel surfaces were comparable to those obtained from Monte Carlo calculation assuming a diffuse reflection. However, the experimental values for He were observed to be 3% to 5% higher. By assuming a diffuse-specular reflection at the wall, the momentum accommodation coefficients for H_2, N_2 and Ar on polished stainless steel were estimated to be in the range from 0.98 to 1.00, while for He it varied from 0.95 to 0.97.

Concerning the effect of the surface material and roughness on flow conductance, measurements of some samples indicated values from 1% to 7% smaller than the calculations. These differences were attributed to the slope of the surface roughness, rather than the arithmetic average surface roughness or the material. This argument was supported by

comparison of the surface characteristics and by the works of Davis *et al*. (1964) and Sugiyama *et al*. (1996). Finally, the authors attributed the small effect of the surface material to the existence of an oxide layer, an impurity or an absorbed layer such as H_2O on the surface of the rotating disk.

Regarding the presence of contaminants on the surface, Sazhin *et al*. (2001) examined the level of adsorbed materials on the microchannel wall and analyzed the flows of helium (He), neon (Ne), argon (Ar) and krypton (Kr) through a long tube ($L = 124\ mm$) with 3.6 mm in diameter in the free molecular regime. The capillary tube was made of Pyrex glass and its internal surface was covered with silver (Ag) and titanium (Ti). By monitoring the pressure in a reservoir located upstream of the tube, the mass flow rate was determined and the TMAC was extracted by fitting measurements with predictions obtained with the Test Particle Monte Carlo method. After the experiments with atomically clean surfaces of silver and titanium, the titanium surface was exposed to oxygen and the effect of the adsorbed layer of oxygen on the mass flow rate and TMAC was assessed. Figure 2.15 presents the non-dimensional reduced mass flow rates of He, Ar and Kr measured for the titanium surface as a function of the surface exposure to oxygen.

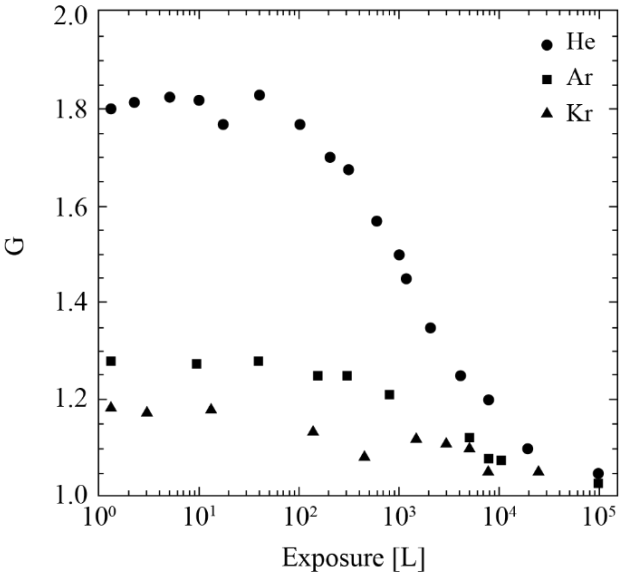

Figure 2.15 – Reduced mass flow rates for titanium surface partially coated by O_2 versus the exposure measured in langmuir (L) (Sazhin *et al*., 2001).

As can be seen, the mass flow rates decreased significantly for all gases with the surface exposure to oxygen. Hence, the surface contamination increases the TMAC and the gas–surface interaction approaches a complete diffuse reflection. Values of TMAC equal to 0.71 were obtained for flow of He in the tube with atomically clean silver and titanium surfaces and 0.96 in the tube with titanium surface highly exposed to oxygen. Similar trends were observed for flows of other gases (Table 2.2). The authors concluded that for atomically clean surfaces the value of the TMAC depends almost exclusively on the gas species and not on the surface material. The values obtained for TMAC were far from unity, with higher differences for lighter gases. On the other hand, as the level of contaminant on the surface is increased the value of the TMAC becomes closer to unity.

Table 2.2 – TMAC value for different gases and surfaces (Sazhin *et al*., 2001).

Gas	Clean Ag	Clean Ti	Ti coated by O_2
He	0.71	0.71	0.96
Ne	0.80	-	-
Ar	0.88	0.87	0.98
Kr	0.92	0.92	1.00

The wall temperature is another aspect worth investigating. When the molecules of a gas flowing through a microchannel reach the wall they are trapped, undergo many collisions and only leave the wall after some residence time. This behavior governs the momentum exchange between the molecules and the wall and, consequently, affects the TMAC. Since this trapping–desorption behavior of the gas molecules depends on the wall temperature, the same is expected to happen with the TMAC. However, most studies deal with temperatures in the narrow range from 293 K to 300 K. Therefore, it is fair to say that measurements in this area are inexistent. Nevertheless, a brief insight into this phenomenon can be obtained from the flow induced by shear stress investigated by Cao *et al*. (2005).

Cao *et al*. (2005) explored the TMAC dependence on the surface temperature by means of a molecular dynamics (MD) simulation. Ar flows were established between two parallel platinum plates set 0.1 μm apart with the same temperature, from 83.9 K to 388.2 K, and average Knudsen number in the range of 0.01–0.12. The surface temperature was found to have a significant effect on the TMAC, with higher temperatures

reducing the TMAC values (Figure 2.16). The authors also showed that this effect on the gas–surface interaction is more pronounced at very low temperatures.

2.1.4 Concluding remarks

Few experimental investigations available in the literature have considered microchannels of circular cross section, mainly because the mass flow rate for a specific rarefaction condition is much smaller in microtubes than in rectangular microchannels, making the measurements more difficult. This difficulty arises because the microtube diameter for a fixed pressure drop must be equal to the smaller dimension of the rectangular microchannel to achieve the same Knudsen number. Naturally, there is no relation between the Knudsen number and the width of the rectangular microchannel. Therefore, this dimension can have any value, providing large flow areas even for small Knudsen numbers. Currently, researchers circumvent this difficulty by using tubes of larger diameters or groups of microtubes in parallel.

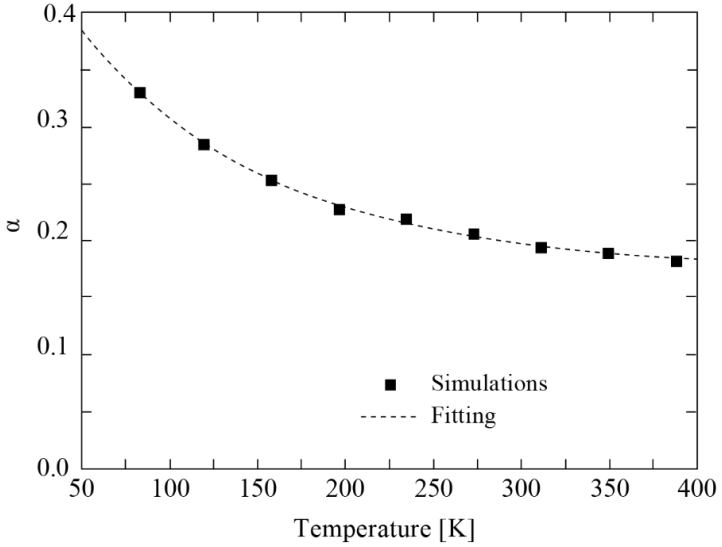

Figure 2.16 – Dependence of TMAC with temperature (Cao *et al.*, 2005).

Concerning the gases analyzed, a very limited number of gases was considered so far. Most of the works were focused on monoatomic and simple gases such as H_2, N_2, O_2 and CO_2. Therefore, data of slip and accommodation coefficients are scarce for polyatomic molecules. Although the theoretical models used to extract the TMAC consider the gas to be monoatomic, in the case of isothermal flows these models can be extended to the analysis of polyatomic molecules without introducing significant errors. Theoretical results reported by Loyalka and Storvick (1979) and recently highlighted in an extensive review by Sharipov (2011), suggest that the viscous slip coefficient, σ_P, is not affected by the internal structure of the molecules.

Moreover, few works considered materials for the microchannel other than silicon and silica. Therefore, there is also a need to establish slip and accommodation coefficients for alternative materials as well as to identify its influence on the flow. The effect of the surface roughness must be treated in conjunction with this topic. Other aspects that are usually treated as of secondary importance, such as the effect of the temperature and contamination of the surface, must be carefully controlled in experimental works.

Many authors have investigated the gas–surface interaction and there is currently a large variability in the data available. This problem is associated with uncertainties in the measurements, which become even more problematic for lower pressures, and with uncontrolled variables that can affect the flow. For example, the difference between the surface roughnesses of the channels of two different studies may give rise to discrepancies between the measurements for the same gas and channel material. The value of the surface roughness is not even mentioned in some studies. This aspect must be added to the natural variability of the experiment itself, contributing to the large dispersion of the results reported in the literature. Finally, there is also a difficulty in comparing results of TMAC obtained from different models even when based on the same experimental data.

2.2 MAIN CONTRIBUTIONS OF THE THESIS

Many experimental studies of gas microflows are available in the literature, but there remain many open questions about the gas–surface interaction. This thesis aims to contribute to the understanding of the gas–surface interaction through the following actions:

i. Development of experimental setups and proposal of a new method to extract data to characterize the gas–surface interaction, with special attention to the slip and accommodation coefficients;

ii. Determination of slip and accommodation coefficients for polyatomic gases commonly used in the refrigeration industry, namely hydrocarbon R600a (Isobutane) and fluorocarbon R134a (1,1,1,2-Tetrafluoroethane) over metallic surfaces;

iii. Assessment of the effect of the gas–surface interaction by adopting commercially available microchannels manufactured from different metallic materials, such as stainless steel, copper and brass.

3 EXPERIMENTAL SETUP AND PROCEDURE

3.1 MASS FLOW RATE MEASUREMENT TECHNIQUES

In the analysis of isothermal gas flows through microchannels the interest usually resides in the determination of mass flow rates induced by a specific pressure difference. Direct measurements of mass flow rate are not possible with flowmeters and high precision flow sensors since their range of applicability is usually restricted to values above 10^{-8} kg/s (Ewart *et al*., 2006), with some manufacturers already providing ultra-low mass flow meters capable of measuring flows as low as 10^{-10} kg/s. Therefore, alternatives for measuring extremely low mass flow rates, in the order of 10^{-13} kg/s, were developed. Three techniques are most commonly employed: the liquid droplet method, the constant pressure method and the constant volume method.

The liquid droplet method is a direct measurement technique in which the volumetric flow rate induced by a pressure difference is determined by monitoring the motion of a liquid droplet flowing along calibrated transparent tubes located at the inlet and/or outlet of the microchannel (Harley *et al*., 1995; Maurer *et al*., 2003; Colin *et al*., 2004; Ewart *et al*., 2006) (Figure 3.1). Optical-electronical sensors are frequently used to monitor the liquid droplet displacement. For mass flow rate measurements at low pressures, liquids with low saturation pressure must be used to prevent vaporizing effect on the moving surface of the droplet. Although this method provides a direct measurement of the volumetric flow rate, its implementation is associated with two main difficulties (Ewart *et al*., 2006): i) the precise identification of the droplet-gas interface; ii) the process of introducing the liquid droplet without perturbing the pressure in the reservoirs or forming several droplets, which may also collapse inside the calibrated tube. Quasi-stationary measurements of mass flow rate are obtained when the volumes of the reservoirs are sufficiently large so that the pressure variations are negligible during the measurement interval.

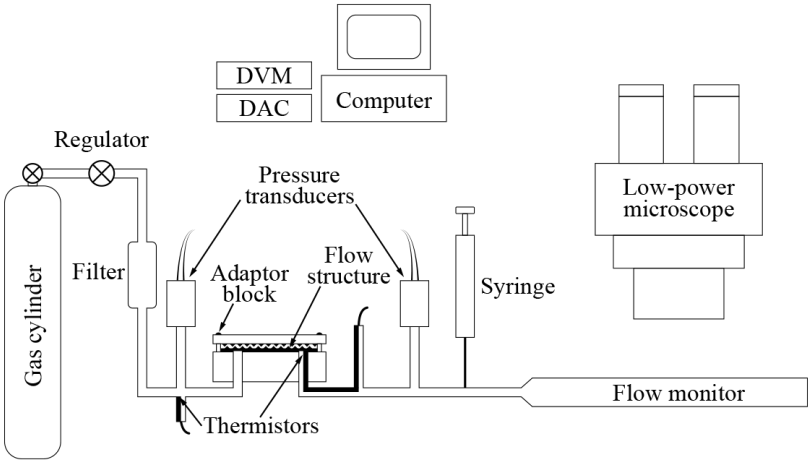

Figure 3.1 – Experimental setup used in the liquid droplet method (Harley *et al*., 1995).

The constant pressure and the constant volume methods are indirect measurement techniques, which use the gas equation of state to relate detectable changes in the volume or pressure, respectively, to the mass flow rate in the microchannel. The constant pressure technique, as its name suggests, consists in keeping the pressure constant in a reservoir located upstream or downstream of the microchannel by varying its volume. This change of volume, ΔV, is usually obtained by driving a piston into the reservoir (Figure 3.2). Under isothermal conditions, the mass flow rate through the microchannel can be correlated with the variation of the reservoir volume with time (McCulloh *et al*., 1987; Jousten *et al*., 2002). This approach has the inconvenient that for very low mass flow rates it requires prohibitively small rates of advance of the piston. In addition, high-integrity seals are necessary to prevent gas leakages (Arkilic *et al*., 1997). Due to the inherent construction difficulties of this technique, its use has been avoided recently.

The constant volume method allows measurement of mass flow rate through a microchannel by monitoring the pressure variation with time in a rigid reservoir located upstream or downstream of the microchannel (Suetin *et al*., 1973; Ewart *et al*., 2006; Pitakarnnop *et al*., 2010; Yamaguchi *et al*., 2011). A detailed description of the constant volume method is presented in the following section, followed by the introduction of the dynamic constant volume technique, developed in the present work.

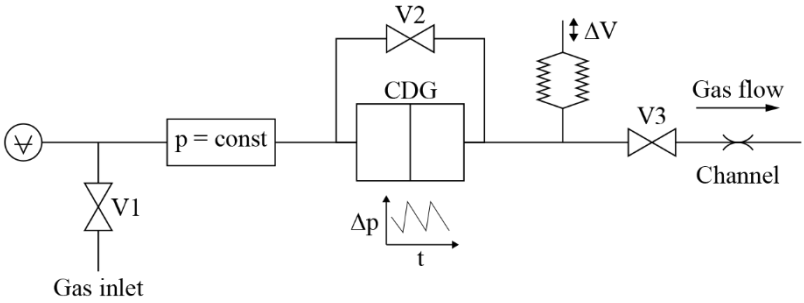

Figure 3.2 – Scheme of the experimental setup used in the constant volume method. V1 to V3: valves; CDG: differential capacitance diaphragm gauge (Jousten *et al*., 2002).

3.1.1 Constant volume method

Consider two finite reservoirs R1 and R2 at pressures P_1 and P_2, respectively, with $P_1 > P_2$, connected by a channel (Figure 3.3). The temperature in both reservoirs is T, as a consequence of the room temperature or a temperature regulation system. This technique consists in detecting small pressure changes in any of the reservoirs due to the mass flowing through the channel connecting both reservoirs.

From the equation of state for an ideal gas, the mass of gas in any reservoir can be determined by

$$m_i = \frac{V_i P_i}{RT} \quad , i = 1,2, \tag{3.1}$$

where V_i represents the volume of the reservoir and R is the specific gas constant. The variation of the mass of gas inside the reservoirs can be related to the variations of pressure and temperature, that is,

$$\frac{dm_i}{dt} = \frac{V_i}{RT}\frac{dP_i}{dt} - \frac{P_i V_i}{RT^2}\frac{dT}{dt} \quad , i = 1,2. \tag{3.2}$$

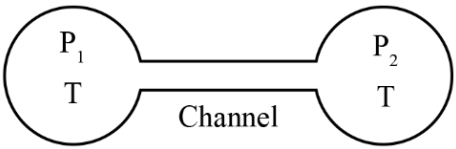

Figure 3.3 – Scheme of the gas flow through a channel using the constant volume technique.

Rearranging the terms, Eq. (3.2) can be written as

$$\frac{dm_i}{dt} = \frac{V_i}{RT}\frac{dP_i}{dt}(1 - \varepsilon_i),\ i = 1,2, \tag{3.3}$$

where

$$\varepsilon_i = \left(\frac{1}{T}\frac{dT}{dt}\right)\Big/\left(\frac{1}{P_i}\frac{dP_i}{dt}\right) = \frac{P_i}{T}\frac{dT}{dP_i}\ ,\ i = 1,2 \tag{3.4}$$

is a measure of the variation of temperature in relation to the variation of pressure and gives an indication of how close an experiment is to a perfect isothermal condition, i.e., $\varepsilon_i = 0$. If ε_i is small enough, the isothermal condition is acceptable and dm_i/dt can be calculated solely by means of the pressure derivative (Eq. (3.2) with $\varepsilon_i = 0$), considering an additional uncertainty associated with the term $(1 - \varepsilon_i)$. In the experiments carried out in the present work, this condition was considered acceptable if $|\varepsilon_i| \leq 0.01$.

If there is no gas accumulation inside the channel, then the mass flow rate flowing through the channel, $\dot{m}$, is equal to the mass flow rates leaving the upstream reservoir and entering the downstream reservoir. Consequently,

$$\dot{m} = -\frac{V_1}{RT}\frac{dP_1}{dt} = \frac{V_2}{RT}\frac{dP_2}{dt} \quad . \tag{3.5}$$

If in the measurement interval the pressure variation is small, it can be approximated by a linear function of time, that is,

$$P_i = A_i t + B_i \ . \tag{3.6}$$

Then,

$$\frac{dP_i}{dt} = A_i \ . \tag{3.7}$$

In such a flow condition, the term dP_i/dt is equal to a constant obtained from curve-fitting of the experimental data with Eq. (3.6). As a result, from Eq. (3.5), the mass flow rate $\dot{m}$ is also constant along the time interval considered.

As explained, the flow condition represented by Eq. (3.6) is associated with the existence of small pressure changes, typically on the order of 1–2% (Pitakarnnop *et al*., 2010). On the other hand, the pressure variation in the reservoirs must be sufficiently large in order to be detected by the pressure transducers. Therefore, conflicting requirements arise in the constant volume method regarding the magnitude of the pressure variation. This problem is circumvented by defining appropriately the time interval for the measurements. In other words, the time interval is defined long enough to allow the detection of pressure changes and sufficiently small so that these variations remain linear.

The direct application of this technique for flows near atmospheric pressure is highly sensitive to temperature fluctuations, since larger pressures contribute to the increase of ε_i in Eq. (3.4). In order to overcome this difficulty, Arkilic *et al*. (1997) introduced a variation of this method, namely the dual-tank method, in which the mass flow rate is determined from the variation in the differential pressure between two reservoirs at thermal equilibrium.

Recently, the steady character of the constant volume method was replaced by a time-dependent methodology proposed by Rojas-Cárdenas *et al*. (2011) to measure the mass flow rates induced by temperature gradients. The experimental setup accounted for an additional gas path of large dimensions between the reservoirs. In such a way, any possible pressure difference between the reservoirs generated by the temperature-driven flow through the microchannel was prevented by the flow in the secondary gas path, and a stationary flow was obtained. To allow the measurement of the mass flow rate, however, detectable pressure changes were necessary in the reservoirs and were obtained with the closure of the secondary gas path. In this way, the pressures in the reservoirs changed, but a counter Poiseuille flow was engendered. However, in the initial moments of the experiment, the counter flow generated by the pressure difference between the reservoirs could be neglected because it was much weaker than the thermally-driven flow, with a linear pressure increase being verified.

3.1.2 Dynamic constant volume method

In the present work, influenced by the method proposed by Rojas-Cardenas *et al*. (2011), a time-dependent version of the constant volume method was developed for measurement of mass flow rates induced by pressure gradients. The dynamic constant volume method consists in correlating the mass flow rate through the microchannel analyzed with

the pressure variations in the reservoirs located upstream and downstream of the channel, as in the standard constant volume method. The main novelty introduced is that instead of considering a time interval in which the pressure varies linearly, the whole duration of the experiment is considered to obtain quasi-stationary measurements of mass flow rate.

To understand the method, consider that the pressures in the reservoirs upstream (R1) and downstream (R2) of the microchannel (Figure 3.3) are P_1^0 and P_2^0 in the beginning of the experiment. Suppose that $P_1^0 > P_2^0$, hence the gas flow is induced through the microchannel from R1 to R2. As the experiment proceeds the pressure in the upstream reservoir $P_1(t)$ is decreasing and the pressure in the downstream reservoir $P_2(t)$ is increasing, as a result of the gas flow, until thermodynamic equilibrium is reached, that is, $P_1 = P_2 = P_{EQ}$. Since the pressure difference imposed between the ends of the microchannel, $\Delta P(t) = P_1 - P_2$, decreases with time, the mass flow rate through the microchannel, $\dot{m}(t)$, also decreases, from a maximum at the beginning of the experiment to zero at the end.

In any instant during the experiment, Eqs. (3.1) – (3.5) obtained for the constant volume method hold. Therefore, the variation of mass in any of the reservoirs can be calculated from Eq. (3.5).

Since the method proposed relies on the assumption that the mass flow rate through the microchannel can be obtained simply from the pressure variations in the reservoirs, it is fundamental to determine the pressure derivative with respect to time in the best possible manner from the experimental data. Herein, the experimental data is fitted with an arbitrary function to allow the analytical evaluation of the derivatives appearing in Eq. (3.5). Polynomial functions are a clear first attempt to fit the data. However, given the asymptotic behavior of the pressure measurements, it was seen that usually a single polynomial function does not fit adequately the data along the entire time length of the experiment, requiring a piecewise fitting. Besides, even if a good fit is obtained in a determined time interval, the derivatives are not always well-behaved and can provide unexpected results. In this sense, a fitting function based on physical reasoning would be a better choice.

3.1.2.1 Constant conductance

In order to obtain an expression describing the evolution of pressure with time inside the reservoirs, consider the definition of pressure throughput for each of the reservoirs:

$$Q_i = \frac{d(P_i V_i)}{dt} = V_i \frac{dP_i}{dt}\ , i = 1{,}2. \tag{3.8}$$

In this equation, the second equality arises from the fact that the reservoirs have constant volume. Also, from Eq. (3.5) and considering that the whole system is under isothermal condition, we can write $Q_2 = -Q_1$. Finally, if one uses an electrical analogy, it is possible to associate the throughput (current) to the difference of pressure through the channel (potential) by means of the inverse of a hydraulic resistance, that is, the conductance C. Hence,

$$Q_2 = -Q_1 = C(P_1 - P_2)\,, \tag{3.9}$$

where the conductance, C, is a practical parameter often used in vacuum technology. Therefore, the following system of equations can be written:

$$\frac{dP_1}{dt} = -\frac{C}{V_1}(P_1 - P_2)\ \ , \tag{3.10a}$$

$$\frac{dP_2}{dt} = \frac{C}{V_2}(P_1 - P_2). \tag{3.10b}$$

Assuming that C is constant, the expression used by Porodnov *et al*. (1974) relating the pressure difference between the reservoirs with time can be retrieved from Eq. (3.10), that is,

$$\Delta P = \Delta P^0 e^{-t/\tau}\ , \tag{3.11}$$

where ΔP^0 is the pressure difference in the beginning of the experiment and τ is a characteristic time, defined as:

$$\tau = \frac{V_0}{C}\ \ , \tag{3.12}$$

with

$$V_0 = \frac{V_1 V_2}{V_1 + V_2}\,. \tag{3.13}$$

The parameter τ can be determined by fitting the experimental data of $\Delta P(t)$. The mass flow rate through the channel $\dot{m}$ can be obtained by manipulating Eqs. (3.5) and (3.11):

$$\dot{m} = -\frac{V_0}{RT}\frac{d\Delta P}{dt} = \frac{V_0}{RT}\frac{\Delta P}{\tau} \quad . \tag{3.14}$$

An interesting aspect of this approach is that by fitting the pressure difference for a particular experiment along time with Eq. (3.11), the characteristic time of the experiment is obtained and this parameter allows the channel conductance to be determined directly via Eq. (3.12).

It is important to emphasize that Eqs. (3.11) – (3.14) are valid only for the particular case in which C remains constant during the experiment, which is not always the case. The conductance depends on many aspects, as the geometry of the channel, the gas properties and the level of rarefaction. Even if the gas and the channel remain the same during an experiment, the pressure in the channel changes along the experiment and so does the rarefaction level. As a consequence, the conductance cannot be considered constant, except when the volumes of the reservoirs are equal to each other, that is, $V_1 = V_2$. In this particular case, the mean pressure, $P_m = (P_1 + P_2)/2$, remains constant during the whole experiment and so does the rarefaction level. Therefore, experiments in which $V_1 = V_2$ can be used to determine experimentally the conductance of channels. Particularly, for flows in the free molecular flow regime the conductance C remains constant independently of P_m.

3.1.2.2 Variable conductance

For the remaining cases, in which $V_1 \neq V_2$, an original approach is proposed herein. It is assumed that the conductance varies linearly according to the mean pressure P_m during the experiment. Since the experiment setup is a closed system:

$$P_1V_1 + P_2V_2 = P_{EQ}(V_1 + V_2), \tag{3.15}$$

where P_{EQ} is the equilibrium pressure, obtained at the end of the experiment, when the pressures in both reservoirs are equal. Therefore, Eq. (3.10a) can be written in terms of P_1:

$$\frac{dP_1}{dt} = -\frac{C}{V_0}\left(P_1 - P_{EQ}\right), \tag{3.16}$$

where V_0 is given by Eq. (3.13).

By introducing a new variable, $P_1^* = P_1 - P_{EQ}$, Eq. (3.16) can be written in a simplified form:

$$\frac{dP_1^*}{dt} = -\frac{C}{V_0}P_1^*. \tag{3.17}$$

This equation could be easily solved if the conductance C was constant. However, C varies with the channel geometry, gas species and degree of rarefaction. Since the channel and the gas are fixed during an experiment, C is simply a function of the rarefaction level, which can be characterized as a function of the mean pressure P_m, that is, $C = C(P_m)$.

By using Eq. (3.15) and considering that P_{EQ} is constant for a particular experiment, $C = C(P_1) = C(P_1^*)$. Therefore, Eq. (3.17) can be rewritten and integrated as follows:

$$\int \frac{dP_1^*}{C(P_1^*)P_1^*} = -\int \frac{dt}{V_0}. \tag{3.18}$$

The solution of this equation requires the relationship between C and P_1^*. Given that the experiments occur in a reduced rarefaction interval in which C changes moderately, it is convenient to assume that it varies linearly with P_1^*, that is:

$$C(P_1^*) = A_1 + B_1 P_1^* \ , \tag{3.19}$$

with A_1 and B_1 being the linear and angular coefficients of the equation, respectively.

After substituting Eq. (3.19) into Eq. (3.18), the integration yields:

$$P_1 = \frac{\left(\frac{A_1 P_1^{*0}}{A_1 + B_1 P_1^{*0}}\right) e^{-\frac{A_1}{V_0}t}}{1 - \left(\frac{B_1 P_1^{*0}}{A_1 + B_1 P_1^{*0}}\right) e^{-\frac{A_1}{V_0}t}} + P_{EQ} \ , \tag{3.20}$$

with $P_1^{*0} = P_1^0 - P_{EQ}$, and P_1^0 is the upstream pressure at the beginning of the experiment. This equation can be written in a more compact form:

$$P_1 = \frac{\Psi_{A,1} e^{\Psi_{B,1} t}}{1 + \Psi_{C,1} e^{\Psi_{B,1} t}} + \Psi_{D,1} \,, \tag{3.21}$$

with:

$$\Psi_{A,1} = \left(\frac{A_1 P_1^{*0}}{A_1 + B_1 P_1^{*0}} \right) > 0 \quad , \tag{3.22a}$$

$$\Psi_{B,1} = -\frac{A_1}{V_0} < 0 \ , \tag{3.22b}$$

$$\Psi_{C,1} = -\left(\frac{B_1 P_1^{*0}}{A_1 + B_1 P_1^{*0}} \right) > 0 \ , \tag{3.22c}$$

$$\Psi_{D,1} = P_{EQ} > 0 \, . \tag{3.22d}$$

Analyzing Eq. (3.22d), it is possible to see that $\Psi_{D,1} > 0$, giving that it represents the equilibrium pressure. Similar relations can be obtained for the other equations. For instance, since C must be a positive value at any instant during the experiment, $A_1 > 0$ because $C(P_1^* = 0) = A_1$ when the equilibrium pressure is reached in the system. In the same way, $C(P_1^* = P_1^{*0}) = A_1 + B_1 P_1^{*0} > 0$. P_1^* is defined in such a way that it is always greater than or equal to zero. Therefore, $P_1^{*0} > 0$, otherwise no flow would occur. Finally, one can see from Eq. (3.13) that $V_0 > 0$. Consequently, $\Psi_{A,1} > 0$ and $\Psi_{B,1} < 0$.

The signs of the parameters appearing in $\Psi_{C,1}$ can also be determined. For the experiments performed it was seen that C increases when P_m increases, which happens as the equilibrium condition is approached, since $V_1 > V_2$. At the same time, as the experiment proceeds P_1^* is reduced and, as a result, C increases. Consequently, from Eq. (3.19), $B_1 < 0$ and $\Psi_{C,1} > 0$.

A similar expression to Eq. (3.21) can be obtained for P_2, by writing $P_2^* = P_{EQ} - P_2$ and $C(P_2^*) = A_2 + B_2 P_2^*$. Thus,

$$P_2 = \frac{\Psi_{A,2} e^{\Psi_{B,2} t}}{1 + \Psi_{C,2} e^{\Psi_{B,2} t}} + \Psi_{D,2} \,, \tag{3.23}$$

with $\Psi_{A,2} < 0$, $\Psi_{B,2} < 0$, $\Psi_{C,2} > 0$, and $\Psi_{D,2} > 0$. Both Eqs. (3.21) and (3.23) can be written in the following general form:

$$P_i = \frac{\Psi_{A,i} e^{\Psi_{B,i} t}}{1 + \Psi_{C,i} e^{\Psi_{B,i} t}} + \Psi_{D,i} \quad , i = 1,2. \tag{3.24}$$

It should be noted that ideally $A_1 = A_2 = C_{EQ}$, where C_{EQ} represents the microchannel conductance at equilibrium. Hence, $\Psi_{B,1} = \Psi_{B,2}$. Also, $\Psi_{D,1} = \Psi_{D,2} = P_{EQ}$.

Equation (3.24) can be used to fit the experimental data of pressure variation with time in any reservoir of a system in which V_1 and V_2 are not necessarily equal. Actually, Eq. (3.24) could have been defined based only on three coefficients to be adjusted, given that $\Psi_{D,i}$ represents the equilibrium pressure, P_{EQ}, at the end of the experiment, which can be determined if the system is allowed to reach its thermodynamic equilibrium state. However, this reduces the degrees of freedom of the fitting function and can hamper the optimization process to find the function coefficients, as was observed in some experiments. Therefore, it is convenient to keep $\Psi_{A,i}$, $\Psi_{B,i}$, $\Psi_{C,i}$ and $\Psi_{D,i}$ as the fitting coefficients.

Considering Eq. (3.24) and data from a single experiment, the mass flow rate through the microchannel can be calculated by

$$\dot{m} = -\frac{V_1}{RT_1} \frac{\left(P_1 - \Psi_{D,1}\right)\Psi_{B,1}}{1 + \Psi_{C,1} e^{\Psi_{B,1} t}} = \frac{V_2}{RT_2} \frac{\left(P_2 - \Psi_{D,2}\right)\Psi_{B,2}}{1 + \Psi_{C,2} e^{\Psi_{B,2} t}} \, . \tag{3.25}$$

Thus, provided that the pressure measurements are fitted using Eq. (3.24), the mass flow rate at any instant is directly determined from Eq. (3.25).

3.1.2.3 Quasi-stationary condition of the flow

The equations required to obtain the mass flow rate from experimental data were presented in the previous section. Therefore, at this point it becomes necessary to explain how quasi-stationary measurements can be performed considering that the pressures in the reservoirs change continuously during the experiments.

In order to perform this analysis the time-scales associated with the pressure change inside the reservoirs and with the flow inside the microchannel must be evaluated. Recently, Vargas *et al*. (2014) have

shown that the characteristic time associated with the pressure changes can be evaluated as

$$\tau_{P_i} = \frac{V_i/(D/2)^2}{\upsilon} \ , i = 1,2, \tag{3.26}$$

where $\upsilon = \sqrt{2RT}$ is the most probable molecular speed. On the other hand, the characteristic time to establish a steady flow over a cross section of channel, τ_s, was approximated as

$$\tau_s = \frac{(D/2)}{\upsilon} \ . \tag{3.27}$$

Vargas *et al*. (2014) pointed out that numerical results available in the literature for transient flows through long tubes (Lihnaropoulos & Valougeorgis, 2011), short tubes (Sharipov, 2013) and orifices (Sharipov, 2012) indicate that the time necessary to achieve steady-state conditions varies from approximately $5\tau_s$ up to $50\tau_s$, depending on the flow parameters.

Therefore, if $\tau_s \ll \tau_{P_i}$, the characteristic length and time over which the macroscopic quantities may vary are significantly larger in the reservoirs than in the channel (Vargas *et al*., 2014). Consequently, the stationary condition in the flow through the microchannel is reached much faster in comparison with the pressure variations in the reservoirs, and the transient nature of the flow inside the channel can be neglected. Hence, the mass flow rate through the microchannel approaches that obtained under stationary condition. Without further developments and using the same arguments, the stationary flow condition can be assumed in measurements of mass flow rates whenever

$$\frac{\tau_{P_i}}{\tau_s} = \frac{V_i}{(D/2)^3} \gg 1 \ , \tag{3.28}$$

which is the case for the experimental facilities used, where this factor is at least in the order of 10^6.

According to Sharipov and Graur (2014), the characteristic time necessary to establish a steady flow in the whole channel is given by

$$\tau_{\dot{m}} = \frac{2L^2}{(D/2)\upsilon} \ . \tag{3.29}$$

Consequently, a more restrict criterion can be established as

$$\frac{\tau_{P_i}}{\tau_{\dot{m}}} = \frac{V_i}{DL^2} \gg 1 \quad , \tag{3.30}$$

where L is the channel length. For the experimental facilities used this factor is at least 15.

The main advantage of the dynamic technique with respect to the standard constant volume method is that a large dataset is obtained from a single experiment, since a wide range of rarefaction conditions are evaluated as the pressures in the upstream and downstream reservoirs change with time. Additionally, the measurements with this technique presented small variability when compared with results available in the literature using the standard constant volume method.

3.2 EXPERIMENTAL APPARATUS

Three different experimental setups were used for measurements. Two of them were developed during this work at the Federal University of Santa Catarina (UFSC), one of them for the analysis of flows through microtubes and the other one for the analysis of flows through microchannels with rectangular cross section. The third apparatus was made available at the *Institut Clément Ader* in Toulouse, France, where part of this work was developed in collaboration with the *Institut National des Sciences Appliquées de Toulouse* (INSA Toulouse), and was used to verify the independence of the results with respect to the experimental setup and enlarge the rarefaction range analyzed. In the following, these experimental setups will be described.

3.2.1 Experimental setup 1 at UFSC (UFSC1)

This experimental setup is composed of two rigid reservoirs (R1 and R2), each one equipped with pressure (PT1 and PT2) and temperature transducers (TT1 and TT2), connected by a microchannel (Figure 3.4). In order to emulate a wide range of rarefaction conditions the pressure in the upstream and downstream reservoirs must be adjusted in the beginning of the experiment. This is accomplished by means of a tank of gas at high pressure connected to the upstream reservoir (R1) and a vacuum pump connected to the downstream reservoir (R2). Valves A and B are used to isolate the internal rig of the system when the desired pressures in the

reservoirs are established. A secondary path including valve C, which is exclusively opened to reduce vacuum time, also connects the two reservoirs.

In this very simple configuration, the reservoirs are built independently from each other and are connected by means of tube fittings as all other components of the setup. The pressure gauges are connected using ultra-high vacuum VCR metal gasket face seal fittings provided by Swagelok. All the other components are connected with regular Swagelok fittings. This apparatus was designed specifically for isothermal experiments, since it does not have a temperature regulation system. In that case, the temperature of the experiments is determined by the room air-conditioning. Therefore, the reservoirs were made in stainless steel with a substantial mass to increase thermal inertia and prevent small temperature fluctuations in the room to affect the gas inside the reservoirs. The absence of seals and the reduced number of connections minimizes the concern about air leakage when the system is under atmospheric pressure. This configuration is especially suitable for holding microchannels of any length that can be connected via regular Swagelok fittings.

In this setup the reservoirs have constant volumes, but sample cylinders can be attached to them, changing the total volume upstream or downstream of the microchannel. For the experiments reported herein, $V_1 = 181.1 \pm 0.9$ ml and $V_2 = 28.5 \pm 0.8$ ml. These volumes were determined using the method described in Section 3.3 and include also the internal volumes of the connections in the internal rig, between valves A and B.

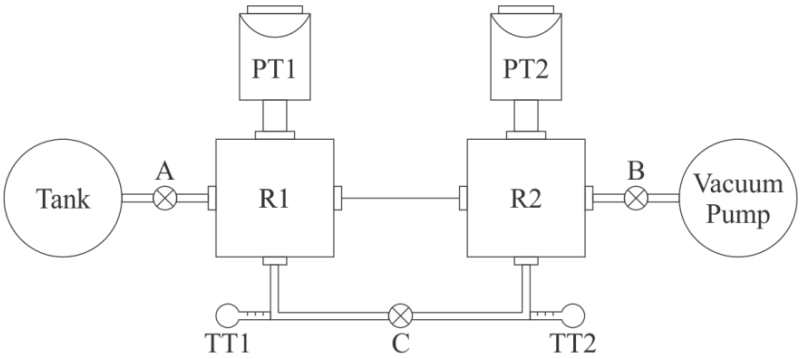

Figure 3.4 – Scheme of the experimental setups developed at UFSC.

Valves A and B were manually operated valves, the first one being a metering needle valve to control the amount of gas delivered to the system by the tank of gas at high pressure, and the second one being a simple needle valve used only as a shut-off valve. Valve C could also be manually operated valve, but a solenoid valve was selected instead because it was shared with experimental setup 2 at UFSC (UFSC2) in which controlled adjustment was required.

The pressure transducers PT1 and PT2 were chosen according to the expected pressure levels in each experiment. Since the microchannels employed in this work possessed characteristic dimensions in the submillimetric range, very low pressures were necessary to establish rarefaction flow conditions. Consequently, four INFICON capacitance diaphragm pressure gauges CDG025D were used, two with a full scale of 133 Pa and two with a full scale 1333 Pa. These pressure transducers had uncertainty of 0.2% of the reading, resolution of 0.003% of the full scale and lowest suggested reading of 0.05% of the full scale, with a response time of 30 ms. Concerning temperature measurements, type T Omega thermocouples with special limits of error were employed in both reservoirs. These thermocouples have uncertainty of 0.5 °C and operating temperature range from -60 °C to 100 °C.

A National Instruments data acquisition system connected to a computer was used to acquire data of pressure and temperature. It consisted of a SCXI-1001 chassis holding a SCXI-1303 terminal block connected to a SCXI-1102 module for temperature measurement with thermocouples. The same block and module were also used for voltage measurement of the pressure transducer signals. This module had a maximum sampling rate of 333 kS/s. Therefore, the acquisition rate was limited exclusively by the response time of the pressure sensors. Attached to this chassis there was also a SCXI-1302 block connected to a SCXI-1180 feedthrough panel, which was in turn connected directly to a PCI-6251 board installed in the computer for controlling the solenoid valve C.

An Edwards T-Station 75D turbo pumping system able to reach a vacuum pressure smaller than 5×10^{-9} mbar was used to evacuate the experimental setup. Such a system was composed of a compact turbo molecular pump EXT75DX and a completely dry XDD1 diaphragm backing pump. The absence of oil in the vacuum pump is a crucial factor since the presence of contaminants in the microchannel can affect considerably the measurements and mask the influence of some parameters on the gas–surface interaction. To prevent leakages, NW vacuum flanges were used to connect the pump to the system. Even if these connections account for elastomeric seals, they were placed outside

the internal rig of the system, encompassed between valves A and B. Figure 3.5 shows a picture of the experimental setup while Figure 3.6 shows how the microtubes were attached to the reservoirs.

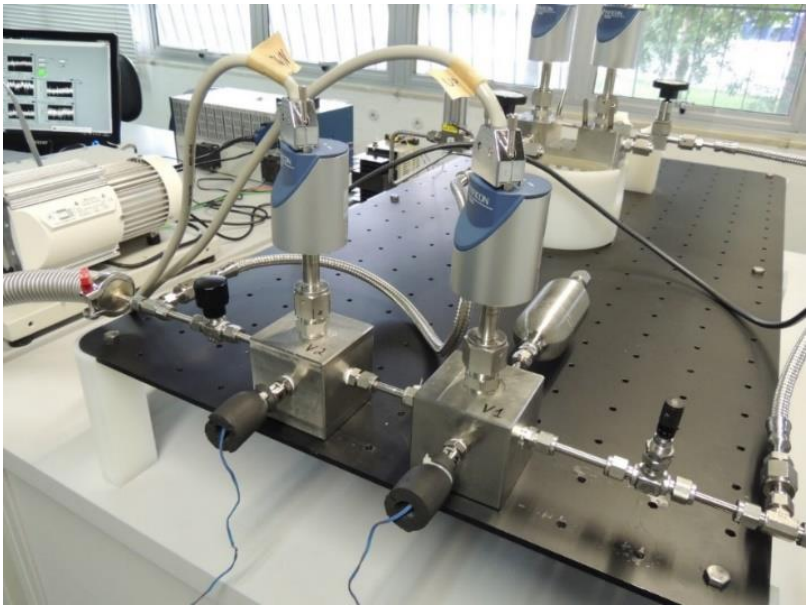

Figure 3.5 – Picture of the experimental setup UFSC1.

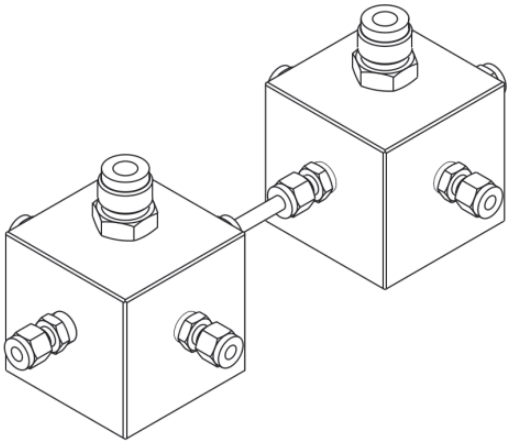

Figure 3.6 – Connection of the microtube with the reservoirs in experimental setup UFSC1.

Before running the experiments, the tightness of the internal rig was verified with an Edwards Spectron 5000 leak detector to guarantee that the experimental setup was free of leakages. After that, a simpler verification based on monitoring the pressure rise in the internal rig was adopted every time that a component was replaced. A pressure increase smaller than 8×10^{-6} Pa/s was detected when the system was subjected to the lowest possible pressure. This would correspond to a leakage of approximately 2.5×10^{-15} kg/s of air entering the downstream reservoir and 1.6×10^{-14} kg/s of air entering the upstream reservoir, which are much smaller than the minimum mass flow rate of approximately 3.5×10^{-13} kg/s measured in the experimental setup.

The experiments adopted microtubes built from commercially available brass and copper capillaries as well as stainless steel needles. The microtubes were placed inside stainless steel tubes with regular Swagelok fittings at the ends and epoxy adhesive was used to fill up the annular space between both components, allowing the gas to flow through the microtube only. This procedure consisted of: i) placing the capillary in the center of the tube and applying epoxy adhesive to one side of the annular space; ii) warming the tube for approximately 24 hours at 70 °C in order to cure the epoxy adhesive; iii) repeating steps i and ii for the other side of the tube; iv) warming the tube for approximately 3 hours at 120 °C to conclude the adhesive cure. In this process, the cure of the epoxy adhesive is performed initially at a low temperature (70°C) in order to avoid the formation of air bubbles. Figure 3.7 shows a picture of one of the microtubes used in the experiments.

An experiment was conducted to confirm the sealing capacity of the epoxy adhesive. It consisted of evacuating an independent reservoir with a connection to the atmosphere clogged with epoxy adhesive, closing the system and evaluating the pressure rise inside it. The pressure rise observed was equivalent to the leakage rate of the reservoir when a plug replaced the clogged connection. Therefore, the sealing capacity of the epoxy adhesive was considered to be better than that of the tube fittings.

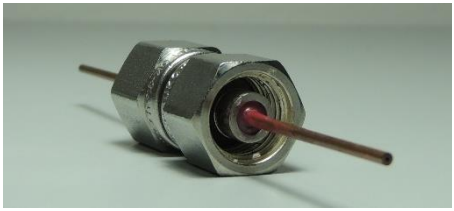

Figure 3.7 – Picture of a microtube used in the experiments.

The characteristics of the three microtubes of different materials employed in the experiments are given in Table 3.1. The diameters of the microtubes were initially measured at its ends by means of an optical measurement system Mitutoyo Quick Vision Apex. The measurements were performed at the Center of Reference in Innovative Technologies (CERTI) located at UFSC. However, optical measurements of samples B and C were not trustworthy, since deformation was introduced at the ends of the microtubes when trying to eliminate the burr generated by the cutting process. Consequently, these measurements are not reported in Table 3.1. This problem was not present in sample A because of the higher stiffness of stainless steel in comparison with copper and brass. In order to circumvent this difficulty, measurements were performed at intermediary positions of the microtubes with an X-ray system EasyTom 130 provided by RX Solutions at the *Institut Clément Ader*. Subsequently, the diameters were finely adjusted from an indirect procedure to be described in Section 3.5. Basically, this procedure is equivalent to determining the diameter of the channel using the analytical solution of a Poiseuille flow and measurements of mass flow rate and pressure drop. Particularly, measurements of nitrogen flows were used for this purpose.

According to Sharipov and Graur (2014), the influence of end effects in the hydrodynamic regime has the order of $(D/2)/L$, while in the free molecular regime it has the order of $(D/2)/L\ln(L/(D/2))$. For the microtubes described in Table 3.1, $(D/2)/L \cong 0.24\%$ and $(D/2)/L\ln(L/(D/2)) \cong 1.46\%$. Therefore, end effects can be neglected without introducing significant errors.

Table 3.1 – Characteristics of the microtubes used in the experiments.

Sample (Material)	Diameter (Optical) [μm]	Diameter (X-ray) [μm]	Diameter (Flow) [μm]	Length [mm]	Roughness $(Ra)/(Rz)$ [μm]
A (Stainless Steel)	438.6±4.5	435.7±3.3	435.5±3.5	92.22±0.01	0.81±0.06/ 4.81±0.47
B (Copper)	-	444.7±3.2	443.1±4.8	92.44±0.01	1.44±0.57/ 8.12±2.37
C (Brass)	-	443.4±5.7	446.2±8.5	92.32±0.01	2.35±0.30/ 11.40±0.92

Estimates of the surface roughness of the microtubes were made available by cutting samples of the materials and inspecting them with an optical surface profiler Zygo NewView 7300 at the Materials Laboratory (LabMat) located at UFSC. The surface roughness is characterized in Table 3.1 by means of Ra, the arithmetic average surface roughness and Rz, the average maximum peak to valley of five consecutive sampling lengths within the measuring length. For each parameter presented in Table 3.1, at least five measurements at different locations were performed. Images of the cross sections of the microtubes at its ends obtained with the optical measurement system Mitutoyo Quick Vision Apex and at intermediary positions obtained with the X-ray system EasyTom 130 are presented in Figure 3.8.

3.2.2 Experimental setup 2 at UFSC (UFSC2)

Schematically, this experimental setup is very similar to the setup presented in the previous section and depicted in Figure 3.4. However, the secondary path with the solenoid valve is necessarily within the internal rig for future measurements of temperature-induced flows, as shown in the scheme of Figure 3.4. In addition to that, three other differences of the new experimental setup can also be pointed out: a) both reservoirs were built as a single piece; b) fluid passages were built around the reservoirs to allow temperature regulation of the gas in the reservoirs; and c) the microchannels were formed by fastening together two plates in the reservoirs. As depicted in Figure 3.9, one of the plates, called channel plate, has a groove along its surface and the other, called intermediary plate, has the inlet and outlet ports.

The reservoirs provided a fastening area for the microchannel and elastomeric seals were used around the inlet and outlet ports in the interface between the reservoirs and the intermediary plate and around the channel in the interface between the intermediary plate and the channel (Figure 3.10). All other connections were made using ultra-high vacuum VCR metal gasket face seal fittings provided by Swagelok. This design of the experimental setup facilitates the manufacturing of microchannels as well as the measurement and control of their geometric characteristics. An important drawback of this setup is that the microchannel length is restricted to 40 mm, giving that the distance between the reservoirs is fixed. This experimental setup was also manufactured in stainless steel with a substantial mass to provide high thermal inertia in order to reduce the effect of temperature oscillations in the laboratory room.

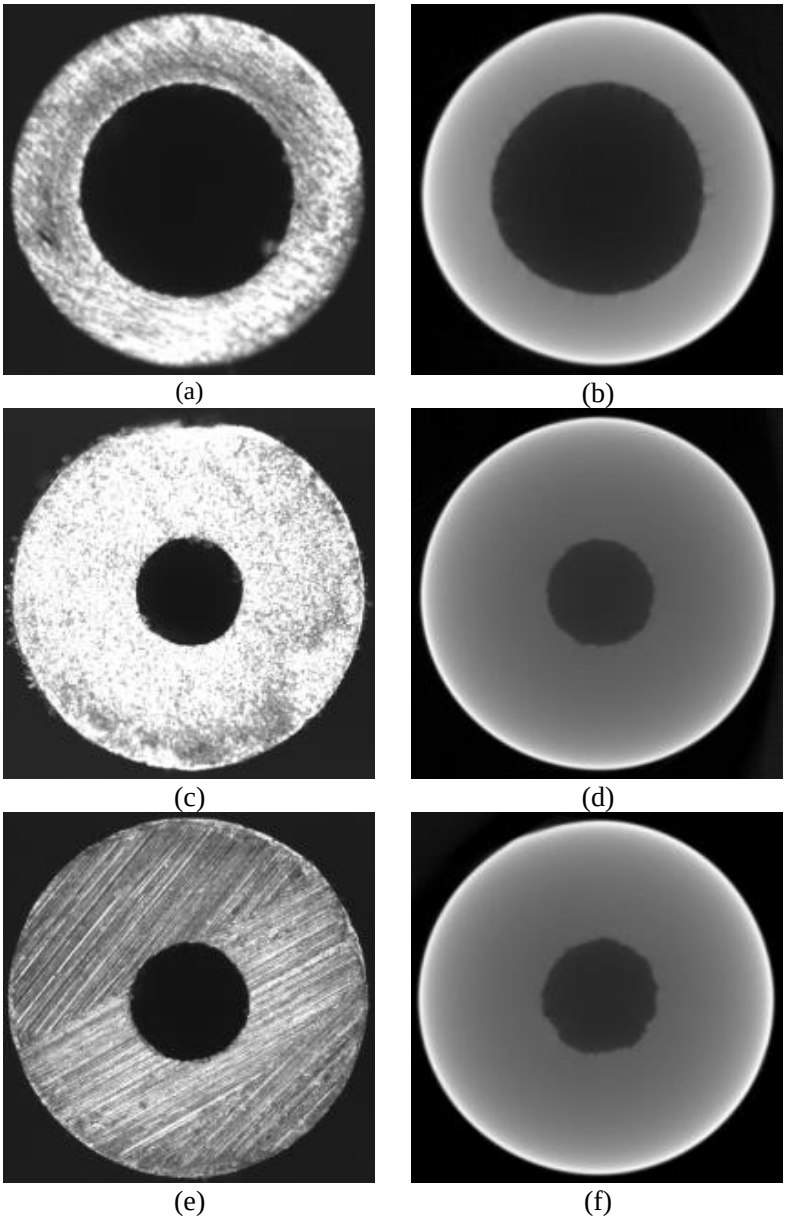

Figure 3.8 – Microtubes cross sections: (a) microtube A (end), (b) microtube A (intermediary position), (c) microtube B (end), (d) microtube B (intermediary position), (e) microtube C (end), and (f) microtube C (intermediary position).

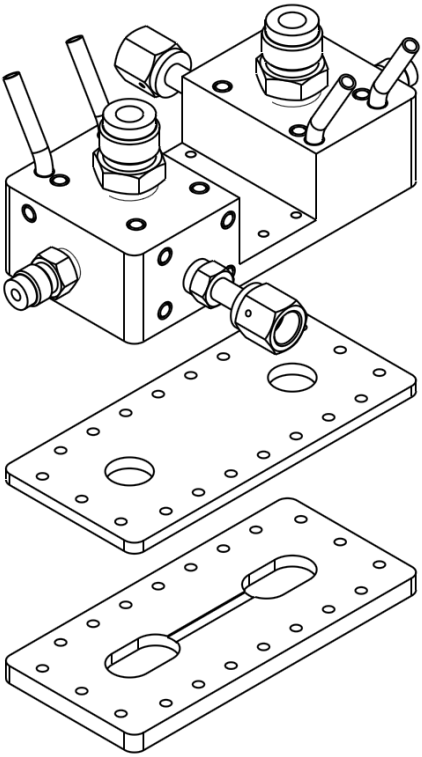

Figure 3.9 – Experimental setup UFSC2.

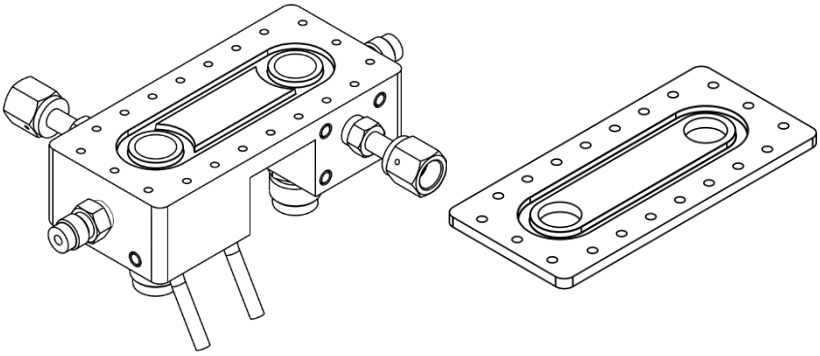

(a) (b)

Figure 3.10 – Seal grooves in the reservoirs (a) and in the intermediary plate (b) of experimental setup UFSC2.

The pressure transducers and the data acquisition system employed in the experiments were the same described in the last section. However, instead of thermocouples, platinum resistance temperature detectors (RTDs) Pt100 of accuracy class 1/3 DIN and diameter of 3 mm were employed in both reservoirs for temperature measurement. The uncertainty of these RTDs is $1/3\,(0.3 + 0.005|T|)$ °C and their temperature operating range is from -50 °C to 250 °C. RTDs with small diameter were chosen to reduce the effect of thermal inertia on the measurements. It should be mentioned that RTDs with holes in the sheath were tested to bring the gas into direct contact with the resistance of the transducer. However, the low pressures in the experiment induced air leakage through the RTD cable and this concept was replaced by sensors with sealed sheath. A SCXI-1503 module dedicated exclusively to temperature measurements with RTDs was connected to a SCXI-1306 terminal block attached to the SCXI-1001 chassis.

The experimental setup was assembled with reservoirs of different volumes: $V_1 = 326.1 \pm 1.3$ ml and $V_2 = 26.4 \pm 0.9$ ml. These volumes were determined using the method described in Section 3.3. Similar to the experimental setup UFSC1, the volumes could be changed by connecting sample volumes to the fixed reservoirs. A pressure rising rate of approximately 1.3×10^{-3} Pa/s was found when the system was subjected to the lowest possible pressure, resulting in leakage rates of approximately 3.9×10^{-13} kg/s in the downstream reservoir and 4.8×10^{-12} kg/s in the upstream reservoir, considerably higher than those verified in the experimental setup UFSC1.

The vacuum system used in the experimental setup UFSC1 was shared with the setup UFSC2. A Quimis Q214M2 thermostatic bath, with a 10 L/min circulation rate, was connected to the flow paths around both reservoirs and the temperature was set to the room temperature to avoid fluctuations during the experiments. For non-isothermal experiments, which will be performed in future investigations, this equipment allows temperature control between -20°C and 120°C.

The tightness of the microchannel is a critical aspect of this experimental setup, since a perfect planar contact between the surfaces of the plates is necessary to avoid leakage. Therefore, narrow geometrical tolerances for the surface finishing of the plates that form the microchannel are required in the manufacturing process. Also, tight dimensional tolerances were specified for the groove in the channel plate to guarantee that the cross section of the microchannel was as uniform as possible along its length. Figure 3.11a shows a picture of the experimental setup UFSC2 and Figure 3.11b shows the complete experimental system.

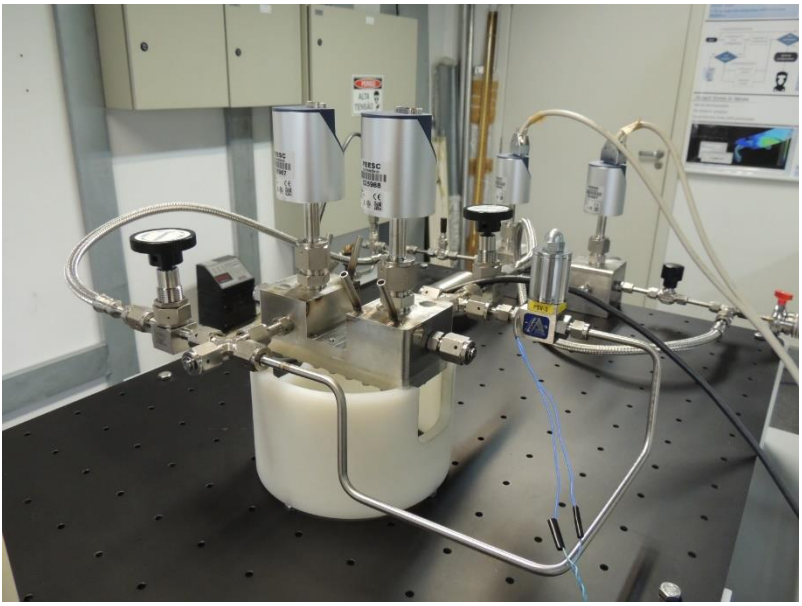

(a)

(b)

Figure 3.11 – Pictures of the experimental setup UFSC2 (a) and the complete system with both experimental setups (b).

A rectangular microchannel with aspect ratio (h/w) close to 1 made in stainless steel was manufactured for the present study. The dimensional characteristics measured are given in Table 3.2. The cross section dimensions and the channel roughness were measured using the optical surface profiler Zygo NewView 7300. All parameters presented in Table 3.2 were obtained from at least five measurements. The height of the channel is the most difficult parameter to be determined because it is affected by the contact between the intermediary and channel plates. This dimension was adjusted based on a procedure with flows of nitrogen, as will be described in the next sections.

The profile of the cross sectional geometry is shown for an intermediary position in Figure 3.12. A carefully controlled manufacturing process was adopted with a high-precision CNC machine and a fine grinding was performed before and after the micro-milling of the channel plate. The first grinding step leveled the entire surface and the second removed any metal burr extending beyond the edge of the cut piece. The plates were carefully inspected along the whole process in order to guarantee the correct tolerances.

The order of the end effects is $h/L \cong 0.85\%$ in the hydrodynamic regime and $h/L\ln(L/h) \cong 4.06\%$ in the free molecular regime (Sharipov & Graur, 2014). Since all experiments were performed in the slip flow and transition regimes, the end effects were neglected.

Table 3.2 – Characteristics of the microchannel used in the experiments.

Height (Optical) [μm]	Height (Flow) [μm]	Width [μm]	Length [mm]	Roughness (Ra) [μm]	Roughness (Rz) [μm]
341.3±1.5	340.8±2.0	309.5±6.5	40.00±0.01	0.18±0.07	1.69±0.28

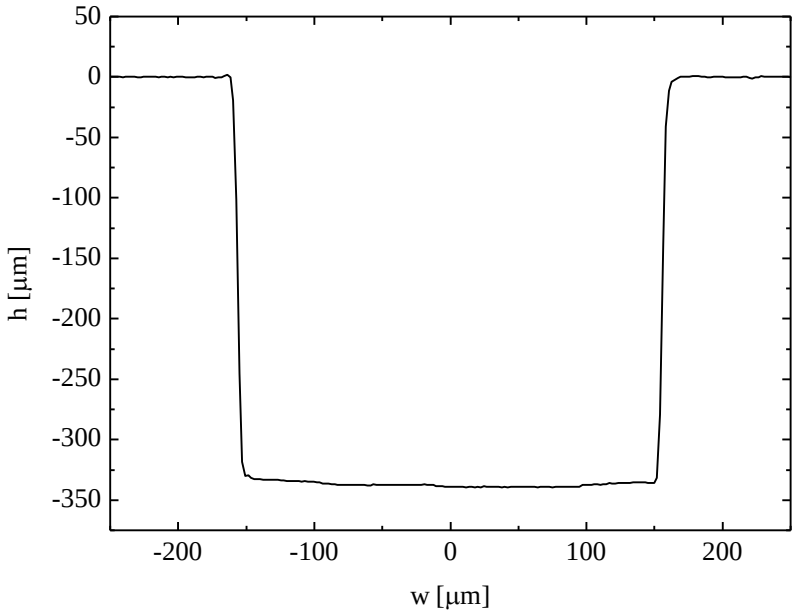

Figure 3.12 – Microchannel cross sectional profile for an intermediary position.

3.2.3 Experimental setup at INSA

This experimental setup was already available at INSA and was built to handle both the constant volume and the droplet tracking methods. All measurements performed at the *Institut Clément Ader* regarding the current work adopted the dynamic version of the constant volume method. The experimental setup consists of an internal test rig, a tank of gas at high pressure and a vacuum pump (Figure 3.13), with a thermal insulation chamber to reduce temperature oscillations. Two Peltier modules can be used to control the temperature inside the system and six diaphragm valves, V1A, V2A, V3A, V1B, V2B and V3B with elastomeric sealing elements are employed. Valves V1A and V1B are used to isolate the internal rig from the other components of the system and valves V3A and V3B are used to set the initial pressures in the reservoirs for the experiment, blocking the gas flow through the microchannel. Valves V2A and V2B are used exclusively for the droplet tracking method, which also needs two series of 12 opto-electrical sensors OSA and OSB for the measurements. The setup was built in stainless steel, aluminum and glass with ISO-KF connections and Swagelok Ultra-

Torr fittings (Pitakarnnop *et al.*, 2010). Connections also allow the addition of sample cylinders in order to change the volumes of the reservoirs.

The two reservoirs used in the experiments had volumes equal to $V_1 = 675.3 \pm 3.0$ ml and $V_2 = 174.5 \pm 1.8$ ml. The tightness of this experimental setup had been previously checked by means of a portable helium high precision leak detector. During the experiments, a pressure rising rate of 1.9×10^{-4} Pa/s was estimated, based on pressure measurements, when the system was subjected to the lowest possible pressure, resulting in leakage rates of approximately 3.8×10^{-13} kg/s in the downstream reservoir and 1.5×10^{-12} kg/s in the upstream reservoir. For a second configuration, the upstream volume was changed to $V_1 = 173.2 \pm 2.2$ ml for a series of experiments with approximately equal volumes in the system. The volumes were determined using the method described in Section 3.3.

The measurements employed pressures transducers CDG025D with full scales of 13332 Pa, 1333 Pa and 133 Pa, represented by CGA and CGB in Figure 3.13. Two auxiliary piezoresistive pressure sensors provided by Kulite, PSA and PSB, were also used to prevent overpressure in CGA and CGB, when higher pressures were introduced in the internal rig. Finally, the temperatures of the gas in the reservoirs were measured with platinum resistance temperature detectors (RTDs) Pt100 of class B, that is, with uncertainty $(0.3 + 0.005|T|)$ °C, placed on the external surface of the reservoirs. An auxiliary thermocouple was used to monitor and control the temperature inside the insulation box. A National Instruments data acquisition system USB-6221 with maximum sampling rate of 250 kS/s was employed in the measurements. A two-stage rotary vane pump with pumping speed of 2.4 m^3/h and an ultimate vacuum pressure of 5×10^{-3} mbar was used.

All experiments conducted using this experimental setup were performed using microtube A described in Section 3.2.1, with dimensions given in Table 3.1. These measurements were useful to validate the similar apparatus at UFSC and to acquire data for a wider gas rarefaction range.

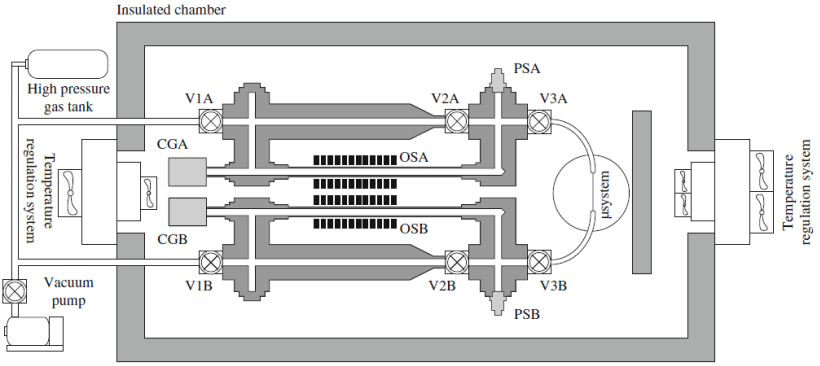

Figure 3.13 – Experimental setup INSA (Pitakarnnop *et al*., 2010).

3.3 DETERMINATION OF THE VOLUMES OF THE RESERVOIRS

In order to measure the mass flow rates through the microchannels by the dynamic constant volume technique, the volumes of the upstream and downstream reservoirs, V_1 and V_2, respectively, must be accurately determined. In the present work these measurements were conducted similarly to a regular experiment, except that the parameters of interest were only the pressures in the reservoirs at the initial instant of the experiment, $P_1^{0\prime}$ and $P_2^{0\prime}$, and the final equilibrium pressure, P'_{EQ}. For isothermal condition, the following equation can be written relating these pressures and volumes:

$$P_1^{0\prime}V_1 + P_2^{0\prime}V_2 = P'_{EQ}(V_1 + V_2) \ . \tag{3.31}$$

Therefore, from pressure measurements and Eq. (3.31), one can determine the relation V_1/V_2. However, a second equation must be provided to determine the absolute values of V_1 and V_2. This can be done by connecting an additional sample cylinder with known volume V_C to one of the reservoirs. In the case the sample cylinder is connected to the upstream reservoir, the following equation holds:

$$P_1^{0\prime\prime}(V_1 + V_C) + P_2^{0\prime\prime}V_2 = P''_{EQ}(V_1 + V_2 + V_C)\,. \tag{3.32}$$

After rearranging Eqs. (3.31) and (3.32), the following expressions can be derived for V_1 and V_2:

$$V_1 = \frac{V_C}{\left(\frac{b}{a} - 1\right)}, \tag{3.33}$$

$$V_2 = \frac{V_C}{(b - a)}, \tag{3.34}$$

where

$$a = \frac{\left(P'_{EQ} - P_2^{0\prime}\right)}{\left(P_1^{0\prime} - P'_{EQ}\right)}\ , \tag{3.35}$$

$$b = \frac{\left(P''_{EQ} - P_2^{0\prime\prime}\right)}{\left(P_1^{0\prime\prime} - P''_{EQ}\right)}\ . \tag{3.36}$$

The volume V_C is measured by weighting the mass of water necessary to completely fill up the sample cylinder.

3.4 EXPERIMENTAL PROCEDURE

Independently of the experimental setup considered, the same procedure was employed before proceeding with the measurements:

i. The microchannel of interest was carefully fitted to the system and the appropriate pressure gauges were mounted in the test section in accordance with the rarefaction conditions of interest;
ii. The entire system was evacuated before the measurements. This was done to guarantee that no trace of gases other than the gas to be tested would be inside the system during the experiments. The required vacuum was achieved after a long period of time, typically around 48 h, in order to remove also gases adsorbed in the internal surfaces of the system (outgassing);
iii. Leak tests were carried out to avoid the presence of air inside the system during the experiments. The tests consisted of setting a pressure in the system and monitoring its value during a long period of time, typically 2 h. The pressure increase could be associated to a leak rate of air entering the system. This test was repeated every time the microchannel or other components of the internal rig were changed. If any leakage was detected, the

appropriate adjustments were made in the modified connections and the process restarted. Figure 3.14 shows the minimum pressure rise in experimental setup UFSC2 along time to illustrate the outcome of a leak test.

The experimental procedure adopted in the setups UFSC1 and UFSC2 consisted in the following steps indicated in Figure 3.15:

i. Setting a uniform pressure inside the system. In this case, valve B was closed and valve A was opened until the required upstream pressure was established. Valve C remained closed during the whole process;
ii. Then, during a brief elapse of time valve B was opened and closed. By doing this, the downstream pressure was reduced and a pressure difference was established between the reservoirs R1 and R2;
iii. Once the pressure difference was established and the valves were closed, the experiment started, with the pressures in the reservoirs varying until the thermodynamic equilibrium was reached in the system. During this period, the pressure increased in the downstream reservoir and decreased in the upstream reservoir.

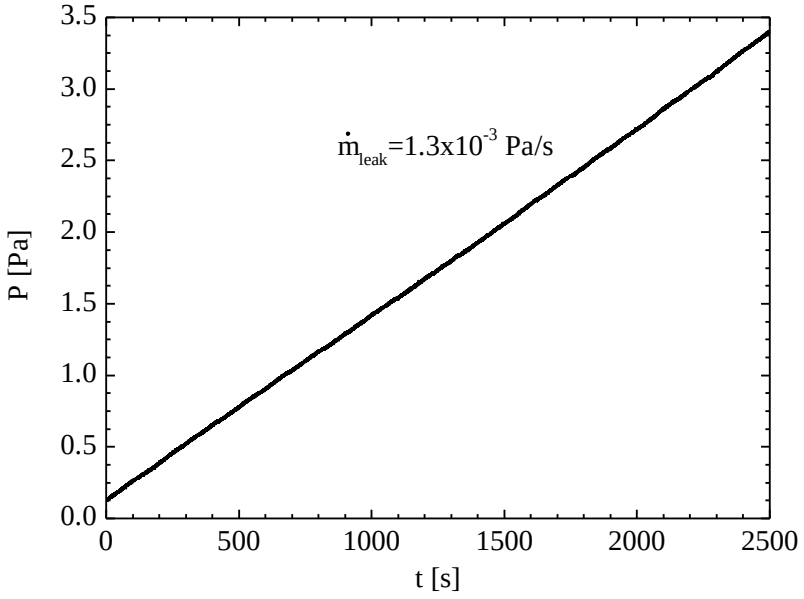

Figure 3.14 – Leak test of experimental setup UFSC2.

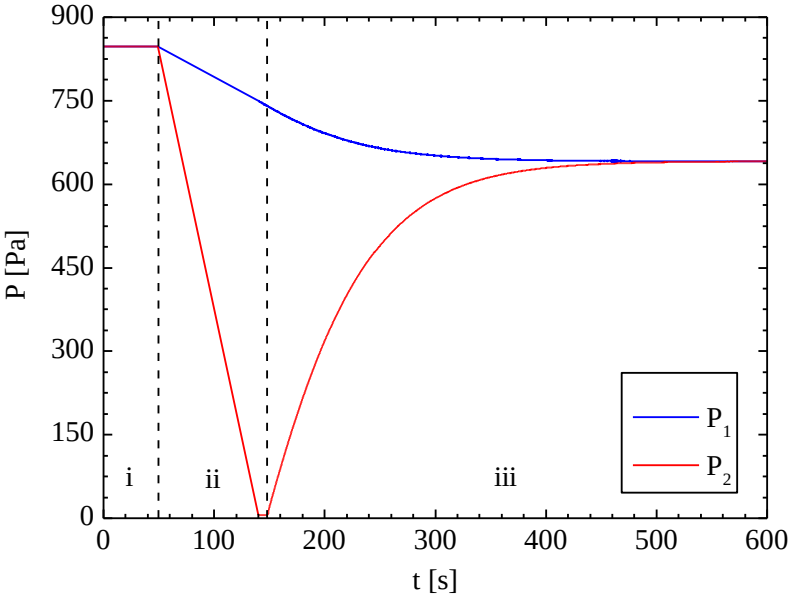

Figure 3.15 – Experimental procedure.

A similar procedure was adopted for the experiments conducted with the experimental setup INSA. However, the charging of the reservoirs was slightly different, given the alternative arrangement of the valves in the system. In this case, after evacuating the system and checking its tightness, valves V1A, V1B and V3A were closed. All other valves remained opened during the whole duration of the experiment. Then, valves V1A and V1B were opened and closed individually in order to set independently the pressures in the upstream and downstream reservoirs. Finally, the experiments were initiated by opening valve V3A and letting the pressures vary until reaching the corresponding value of the equilibrium condition.

In all configurations, the pressure variations in the reservoirs during the experiment were affected by the initial pressure in each reservoir, volumes of the reservoirs, working gas and conductance of the microchannel. On the other hand, the final equilibrium pressure was a function simply of the pressures and volumes of the reservoirs.

3.5 EXTRACTION OF SLIP AND ACCOMMODATION COEFFICIENTS FROM EXPERIMENTAL DATA

Many analytical, semi-analytical and numerical approaches have been proposed in the literature to predict the flow of rarefied gases through channels of different geometries. The most suitable models for the flows analyzed in this work are presented and discussed in the next sections. Based on such models, slip and accommodation coefficients were extracted from mass flow rate measurements.

3.5.1 Circular cross section channel

Predictions of mass flow rate through microtubes in the hydrodynamic and slip flow regimes can be obtained on the basis of the Navier-Stokes equation provided that the velocity slip at the wall is taken into account. An analytical expression can be developed for isothermal steady flows without body forces. The velocity profile in a section of the channel is equal to the one of fully developed incompressible flow, with the density being calculated via the equation of state based on the local pressure and temperature. This assumption is not valid if $Ma > 0.3$ (Colin, 2014), when the flow compressibility changes considerably the velocity profile from the parabolic shape (Guo & Wu, 1998).

Suppose a channel of circular cross section, with diameter D and length L, connecting two reservoirs at constant pressure P_1 and P_2, with $P_1 > P_2$. If $L \gg D$, the end effects can be neglected and the Navier-Stokes equation is reduced to

$$\frac{1}{r}\frac{d}{dr}\left(r\frac{du}{dz}\right) = \frac{1}{\mu}\frac{dP}{dz} \quad , \tag{3.37}$$

where r and z are the radial and longitudinal coordinates, respectively, u is the gas bulk velocity in the longitudinal direction, μ is the gas viscosity and P is the pressure.

The following slip velocity boundary condition is adopted:

$$u|_{r=D/2} = -A_1\lambda\left.\frac{\partial u}{\partial r}\right|_{r=D/2} - A_2\lambda^2\frac{1}{r}\left(\frac{\partial}{\partial r}r\frac{\partial u}{\partial r}\right)\Big|_{r=D/2} \quad , \tag{3.38}$$

where λ is the gas mean free path. In this equation, the wall was considered at rest. The coefficients A_1 and A_2 can be written in terms of

the first- and second-order slip coefficients, σ_P and σ_{2P}, respectively, that is,

$$A_1 = \frac{\sigma_P}{k_\lambda} \ , \tag{3.39a}$$

$$A_2 = \frac{\sigma_{2P}}{k_\lambda^2} , \tag{3.39b}$$

where k_λ is defined in Table 1.1 as a function of the chosen molecular model. The coefficients σ_P and σ_{2P}, contrary to A_1 and A_2, are only weakly dependent of the molecular interaction model considered (Perrier *et al*., 2011).

Following the previous flow formulation, the following expression for the mass flow rate, $\dot{m}$, can be obtained (Perrier *et al*., 2011):

$$\dot{m} = \frac{\pi D^4 \Delta P P_m}{128 \mu R T L} \left(1 + 8 A_1 Kn_m + 16 A_2 \frac{\Pi + 1}{\Pi - 1} \ln(\Pi) Kn_m^2 \right) . \tag{3.40}$$

In this equation $\Delta P = P_1 - P_2$ is the pressure difference between the inlet and outlet of the microtube, $\Pi = P_1/P_2$ is the pressure ratio, $P_m = 0.5(P_1 + P_2)$ is the mean pressure and Kn_m is the mean Knudsen number, calculated with reference to P_m. The other parameters, R, T and L, are the specific gas constant, absolute temperature and microtube length, respectively.

Alternatively, a dimensionless mass flow rate, S, can be defined:

$$S = \dot{m} \Big/ \frac{\pi D^4 \Delta P P_m}{128 \mu R T L} = \left(1 + 8 A_1 Kn_m + 16 A_2 \frac{\Pi + 1}{\Pi - 1} \ln(\Pi) Kn_m^2 \right) \ , \tag{3.41}$$

where the denominator in the first equality represents the analytical solution for a pressure-driven flow with no-slip boundary conditions, that is, a Poiseuille flow.

The range of applicability of Eqs. (3.40) and (3.41) is limited to slightly rarefied flows. In this work it was considered that these equations are valid up to $Kn_m = 0.3$, as suggested by Ewart *et al*. (2006) and Yamaguchi *et al*. (2011). A first-order model can be readily obtained by setting $A_2 = 0$, with accurate results for $Kn_m \leq 0.1$.

The coefficients A_1 and A_2 can be extracted from experimental measurements of mass flow rate, $\dot{m}$, and mean Knudsen number, Kn_m, by fitting the data with Eq. (3.41). It is important to note that the first-order term depends only on the molecular model and the slip coefficient, whereas the second-order term depends also on Π. Consequently, the slip coefficients can be calculated using Eqs. (3.39) and the experimentally determined values of A_1 and A_2. Finally, σ_P can be related to the tangential momentum accommodation coefficient, α, via Eqs. (1.15) – (1.17).

Equation (3.41) can also be used to determine the diameter of the microtube given that all other parameters are known. This can be done by recognizing that Eq. (3.41) can be written as

$$S = A_{exp} + B_{exp} Kn_m + C_{exp} Kn_m^2 \,, \tag{3.42}$$

where A_{exp}, B_{exp}, and C_{exp} are obtained by fitting the experimental data and $S = S(1/D^4)$ and $Kn_m = Kn_m(1/D)$. By comparing Eqs. (3.41) and (3.42), one concludes that A_{exp} must have a unitary value. Therefore, the diameter of the microtube can be adjusted to satisfy $A_{exp} = 1$. This is equivalent to determining the diameter indirectly from mass flow measurements in the hydrodynamic regime using Poiseuille's law. Clearly, this is only valid in the range of applicability of Eq. (3.41), that is, $Kn_m \leq 0.1$ or $Kn_m \leq 0.3$ if a first- or a second-order model is considered, respectively.

For more rarefied flows, predictions based on the solution of the Boltzmann equation are necessary. Usually, these predictions are obtained numerically and expressed in terms of the reduced mass flow rate:

$$Q = \frac{1}{\pi (D/2)^3} \left(\frac{dP}{dz} \right)^{-1} \sqrt{2RT} \dot{m} \,. \tag{3.43}$$

Porodnov *et al*. (1978) presented results of Q as a function of δ for many different values of α, obtained with the BGK kinetic equation and diffuse-specular boundary conditions, as detailed in Annex A. However, for large pressure drops δ can change significantly along the channel. In this case, although $\dot{m}$ must be the same in any cross section of the channel, Q and the pressure gradient can change. Therefore, it is more convenient to introduce the following alternative formulation for the reduced mass flow rate:

$$G = \frac{1}{\pi(D/2)^3}\frac{L}{\Delta P}\sqrt{2RT_m}\dot{m}\,, \tag{3.44}$$

which is independent of the longitudinal coordinate (Sharipov & Seleznev, 1994). Based on numerical results, Sharipov and Seleznev (1994) have shown that, within an error of 1%,

$$G(\delta_1, \delta_2) = Q(\delta_m)\,, \tag{3.45}$$

where δ_1, δ_2, and δ_m are the rarefaction parameter at the channel inlet, rarefaction parameter at the channel outlet and mean rarefaction parameter $\delta_m = (\delta_1 + \delta_2)/2 = \delta(P_m)$. The results of Porodnov *et al.* (1978) were used for comparisons with the experimental measurements obtained in the present work via Eq. (3.44).

3.5.2 Rectangular cross section channel

For slightly rarefied gas flows, that is $Kn_m \leq 0.3$, an analytical expression similar to that for circular cross section channels can be obtained. The channel of rectangular cross section is assumed to connect two reservoirs at constant pressure P_1 and P_2, with $P_1 > P_2$. The cross section of the channel, normal to the z direction, is defined by its height, h, and its width, w. Also, the length of the channel is considered long enough ($L \gg h$) so that end effects can be neglected. By adopting the simplifying hypotheses of steady, isothermal and locally fully developed flow and neglecting body forces, the component of the Navier-Stokes equation in the longitudinal direction is

$$\frac{\partial^2 u}{\partial x^2} + \frac{\partial^2 u}{\partial y^2} = \frac{1}{\mu}\frac{dP}{dz}\,, \tag{3.46}$$

where x and y are the transversal coordinates and z is the longitudinal coordinate. As in Eq. (3.37), u is the gas bulk velocity in the longitudinal direction, μ is the gas viscosity and P is the pressure.

The following slip boundary conditions for stationary walls are applied:

$$u|_{x=\mp w/2} = \pm A_1\lambda\left.\frac{\partial u}{\partial x}\right|_{x=\mp w/2} - A_2\lambda^2\left.\frac{\partial^2 u}{\partial x^2}\right|_{x=\mp w/2}\,, \tag{3.47a}$$

$$u|_{y=\mp h/2} = \pm A_1 \lambda \left.\frac{\partial u}{\partial y}\right|_{y=\mp h/2} - A_2 \lambda^2 \left.\frac{\partial^2 u}{\partial y^2}\right|_{y=\mp h/2} . \quad (3.47b)$$

Differently from the solution for circular cross section channels, the solution of Eq. (3.46) subjected to Eqs. (3.47) is not obtained in a straightforward manner. Méolans *et al*. (2012) presented solution for the mass flow rate through the channel based on an expansion in series of u for the case in which $h \leq w$, that is,

$$\dot{m} = \frac{h^3 w \Delta P P_m}{12 \mu R T L} V_n \left(1 + 6A_1 \frac{T_n}{S_n} Kn_m + \frac{A_2 \pi^4}{16 S_n} \frac{\Pi + 1}{\Pi - 1} \ln(\Pi)\, Kn_m^2\right), \quad (3.48)$$

where $Kn_m = \lambda_m / h$ and

$$S_n = \frac{\pi^4}{96} - \frac{2h}{\pi w} \sum_{n=0}^{\infty} \frac{\tanh(0.5\pi(2n+1)\, w/h)}{(2n+1)^5}, \quad (3.49)$$

$$V_n = \frac{96}{\pi^4} S_n , \quad (3.50)$$

$$T_n = \frac{4}{3} S_n - \frac{1}{3}\left(1 - \frac{h}{w}\right) \sum_{n=0}^{\infty} \frac{\tanh^2(0.5\pi(2n+1)\, w/h)}{(2n+1)^4} . \quad (3.51)$$

The dimensionless mass flow rate, S, is

$$S = \dot{m} \Big/ \frac{h^3 w \Delta P P_m V_n}{12 \mu R T L} = \left(1 + 6A_1 \frac{T_n}{S_n} Kn_m + \frac{A_2 \pi^4}{16 S_n} \frac{\Pi + 1}{\Pi - 1} \ln(\Pi)\, Kn_m^2\right). \quad (3.52)$$

As in Eqs. (3.40) and (3.41), the coefficient of the quadratic term on Kn_m in Eqs. (3.48) and (3.52) is a function of the pressure ratio Π. All the other terms are constant for a particular gas and channel. Again, the denominator in the first equality of Eq. (3.52) represents the analytical solution for a pressure-driven flow with no-slip boundary conditions.

Equation (3.52) can also be written in the form of equation (3.42) and used to determine the height of the channel h considering that all other

parameters are known (including the width of the channel). In this case, $S = S(1/h^3)$ and $Kn_m = Kn_m(1/h)$.

Similar to circular cross section channels, solutions of the Boltzmann equation are also provided for higher rarefied flows in terms of Q:

$$Q = -\frac{1}{h^2 w}\left(\frac{dP}{dx}\right)^{-1}\sqrt{2RT_m}\dot{m} \quad . \tag{3.53}$$

Hadj Nacer (2012) provided results of Q as a function of δ for many different values of α and aspect ratios (h/w) of the microchannel, obtained from the BGK kinetic equation with diffuse-specular boundary conditions, as shown in Annex B for $h/w = 1$.

Again, it is more convenient to have an expression for the reduced mass flow rate G, which is independent of the longitudinal coordinate:

$$G = \frac{1}{h^2 w}\frac{L}{\Delta P}\sqrt{2RT_m}\dot{m}. \tag{3.54}$$

Sharipov (1999) showed that the relation between G and Q provided by Eq. (3.45) can be successfully applied also for rectangular cross section channels with the ratio h/w close to unity.

The present work comprises only the analyses of flows through microtubes and a rectangular microchannel with aspect ratio close to 1. Therefore, it will consider only solutions for circular and square cross section microchannels. Figure 3.16 presents the numerical solutions of $G(\delta_m)$ for these two particular geometries and different values of α, obtained by Porodnov *et al*. (1978) and Hadj Nacer (2012).

The analysis of uncertainties of all measured and calculated quantities is presented in Appendix A.

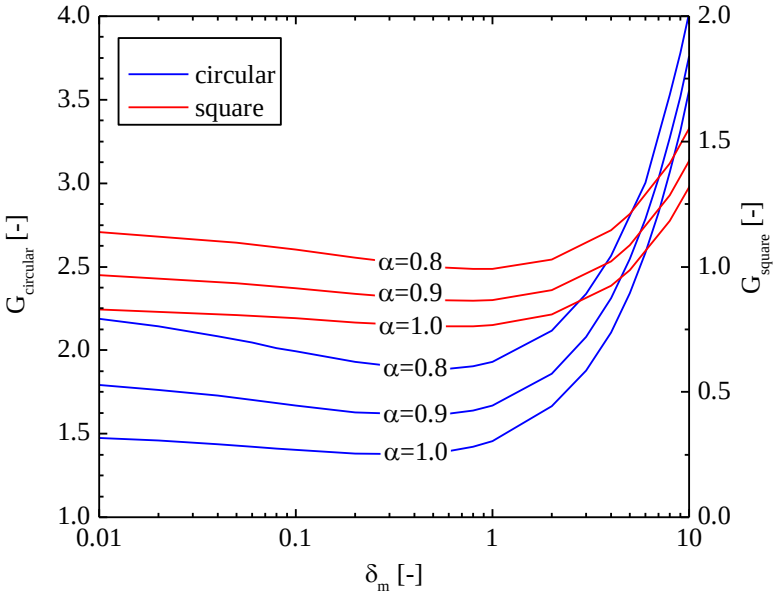

Figure 3.16 – Numerical solutions for $G(\delta_m)$ for circular (Porodnov *et al.*, 1978) and square cross section (Hadj Nacer, 2012) microchannels.

4 RESULTS

This chapter presents the results obtained in the experimental investigation of gas flows in microchannels. First, a comparative analysis with results available in the literature is performed to validate the experimental setup and procedure. Second, the influence of the experimental setup on the results is verified and the quasi-stationary assumption for time-dependent experiments is validated. Third, the experimental data are used to determine the conductance of the microchannels. Fourth, the channel geometry is also analyzed with reference to measurements in a rectangular microchannel with aspect ratio close to 1. Finally, measurements are used to assess the influence of the channel surface — including surface material and surface roughness — on the flow of gases with different chemical compositions (Table 4.1).

Table 4.1 – Properties of the gases at 23 °C calculated using Version 10.101 of Engineering Equation Solver (2016).

Gas	Composition	$R\ [J/kg \cdot K]$	$\mu\ [Pa \cdot s]$	c_p/c_v
Nitrogen	N_2	296.80	1.77×10^{-5}	1.40
R134a	CH_2FCF_3	81.49	1.18×10^{-5}	1.11
R600a	C_4H_{10}	143.05	0.74×10^{-5}	1.09

4.1 EXPERIMENTAL VALIDATION OF THE EXPERIMENTAL SETUP UFSC1 AND PROCEDURE

4.1.1 Comparison with data from the literature

The first experiments were conducted with nitrogen as the working fluid to allow comparisons with data available in the literature. These results also provided a reference for the experiments with other gases. In this experimental campaign, all the results were obtained for microtube A (Table 3.1) in experimental setup UFSC1.

Initially, the data for pressure variation with time inside the reservoirs were fitted using Eq. (3.24). Since the measurements of mass flow rates are associated with the pressure variation in the reservoirs, as described in Section 3.1.2, the fitting capability of Eq. (3.24) was verified. Figure 4.1 shows the fitting of the pressures in the upstream and downstream reservoirs, P_1 and P_2, respectively, for the highest (Figure 4.1a) and lowest values (Figure 4.1b) of the initial mean pressure. Since

all the experiments were initiated with $P_2 \cong 0$, these cases also correspond to the conditions of largest and smallest initial pressure differences.

In both figures, a reduced number of experimental points are plotted to facilitate visualization (the acquisition rate was 33 Hz for all measurements). As can be seen, Eq. (3.24) describes the measurements with significant accuracy in both cases, with determination coefficients, R^2, very close to unity. In general, better agreement was observed for experiments with higher mean pressures. Note that this is not a limitation imposed by the method proposed herein but caused by uncertainties of the employed pressure transducers at lower pressures.

Moreover, Figure 4.1 indicates that at lower pressures, the system takes much longer to achieve the equilibrium pressure. In this sense, experiments involving low pressures are much more difficult with the system more susceptible to leakage and temperature oscillations. In addition, the pressure variations in the reservoirs are smaller and difficult to measure with the employed pressure sensors.

A significant advantage of the dynamic constant volume technique developed in this work is that the mass flow rate data can be extracted as a continuous function from a single experiment for the entire rarefaction range covered. Accurate values of quasi-stationary mass flow rates are provided at any given time of the experiment as long as Eqs. (3.28) and (3.30) are satisfied. However, the technique notably loses accuracy when the experiment approaches the equilibrium condition, which is associated with a null flow rate. This happens partly because even a small leakage can considerably affect the measurement of the mass flow rate. The other aspect is that temperature variations can be significant compared with pressure changes, not following the isothermal assumption adopted initially, i.e., $\varepsilon < 0.01$ in Eq. (3.4).

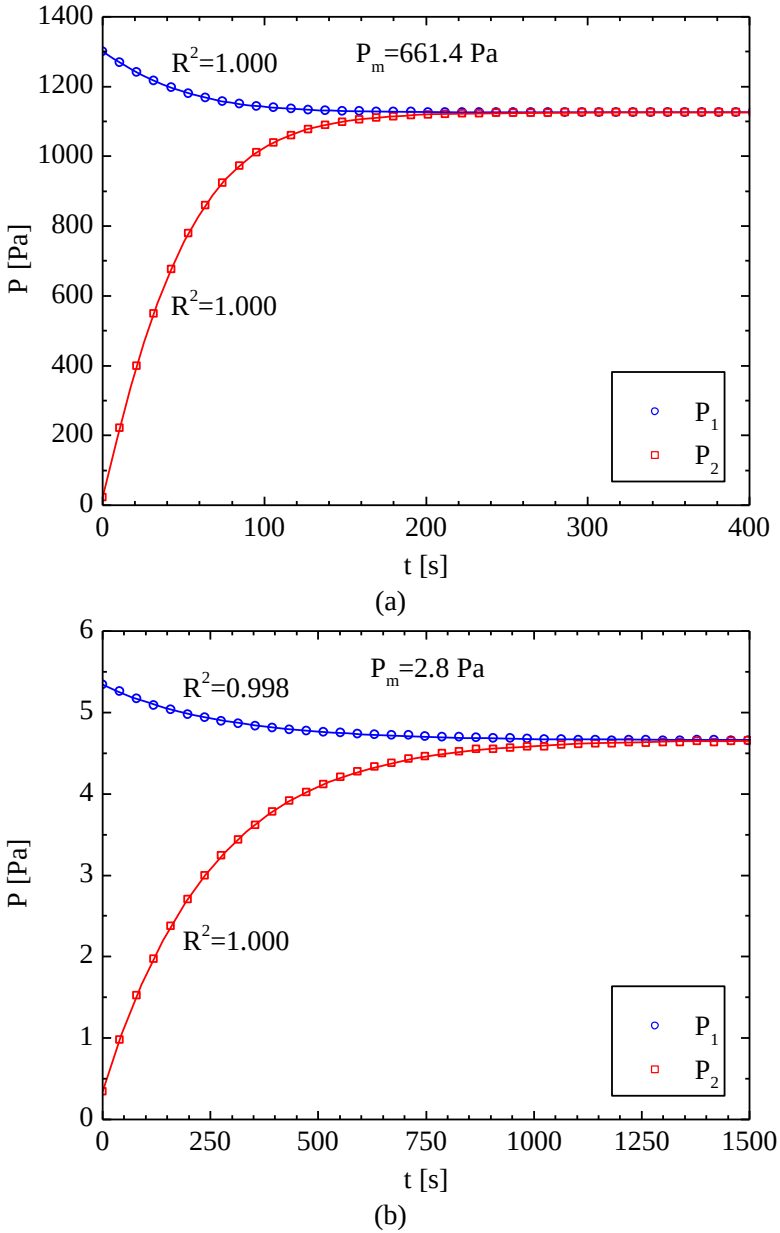

Figure 4.1 – Pressure fitting for experiments with N_2 with largest (a) and smallest (b) initial mean pressures. The pressure uncertainty is approximately 0.2%.

The temperature oscillations were significant compared with the pressure variations only at the end of the experiments. Therefore, the analysis of a single experiment was considered valid until reaching the condition $\varepsilon_i = 1\%$. To estimate ε_i, temperature was fitted using a Fourier series and its derivative with time was employed directly in Eq. (3.4) together with the pressure derivative obtained from Eq. (3.24).

Figure 4.2 plots ε_i against time for the experiment associated with the pressure variations in Figure 4.1a. It can be seen that the condition $|\varepsilon_i| \leq 1\%$ is first violated in the measurements in the upstream reservoir. This happens close to 150 s, while the same condition is reached after approximately 200 s in the downstream reservoir. This is an expected result because the volume of the upstream reservoir is greater than that of the downstream reservoir. Therefore, all variables calculated based on the mass flow rate were estimated from pressure measurements in the downstream reservoir. Since the leakage rate in this reservoir was very small (approximately 2.5×10^{-15} kg/s) compared with the smallest mass flow rate measurement under isothermal conditions (approximately 3.5×10^{-13} kg/s), its influence on the experiments was neglected. Figure 4.3 shows the temperature variation along time for the experiment of Figure 4.1a.

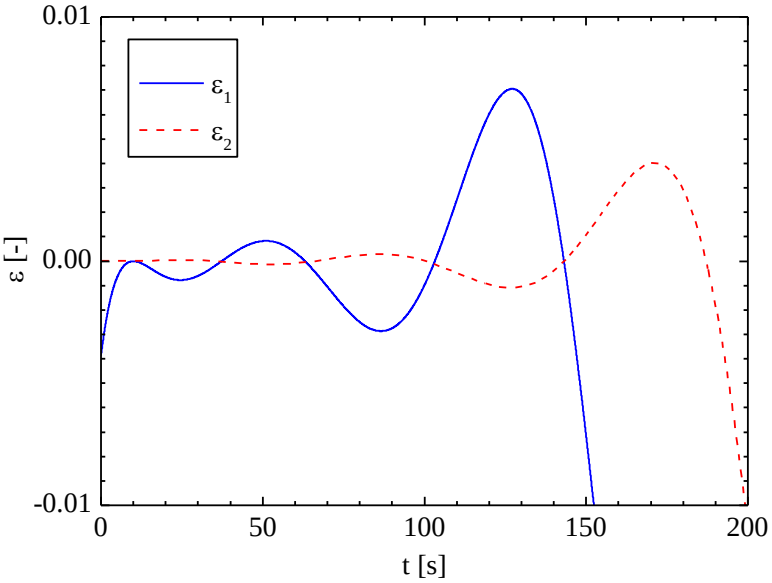

Figure 4.2 – Variation of ε_i, defined by Eq. (3.4), during a single experiment with N_2.

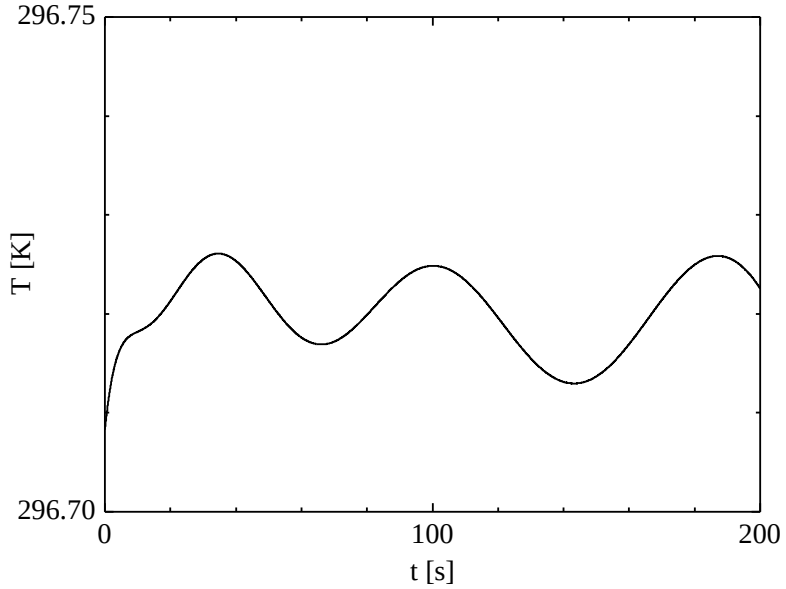

Figure 4.3 – Temperature variation during a single experiment with N_2. The uncertainty of the measurement is equal to 0.5 K.

Figure 4.4 presents the rarefaction level in terms of Kn_m for the first 200 s of the experiment in Figure 4.1a. It can be seen that Kn_m was reduced by almost half, in a range from approximately 0.023 to 0.013. Therefore, data for different rarefaction levels can be obtained in a single experiment. The rarefaction range covered during an experiment can be defined by adjusting the initial pressures and the volumes of the reservoirs. At the beginning of the experiment, the mean pressure is $P_m^0 = (P_1^0 + P_2^0)/2$ and at the end of the experiment the value of thermodynamic equilibrium is reached, i.e., $P_m^\infty = P_{EQ} = (P_1^\infty V_1 + P_2^\infty V_2)/(V_1 + V_2)$, where the superscripts "0" and "∞" refer to conditions at the beginning and end of the experiment, respectively.

Even if the mass flow rates are more accurately determined from pressure measurements in the downstream reservoir, the measurements in the upstream reservoir can be used to verify the consistency of the results. Figure 4.5 presents the mass flow rates through the microtube calculated from measurements in the upstream and downstream reservoirs via Eq. (3.25) for the first 150 s of the experiment depicted in Figure 4.1a. During this period, the temperature oscillations can be neglected and both measurements are valid. The black dashed lines indicate the uncertainties

associated with the downstream measurements, which have the smallest uncertainty range. The analysis of uncertainties is presented in Appendix A. It can be seen that the measurements agree, thus demonstrating the consistency of the measurement method. Differences of approximately 0.7% were observed at the beginning of the experiment, as shown in the inset of Figure 4.5. In the particular case considered, the mass flow rate varied from 6×10^{-8} to 2×10^{-9} kg/s, that is, it decreased almost thirty-fold in one experiment.

A series of similar experiments allowed measurements for a wide rarefaction range and lower mass flow rates under more rarefied conditions, reaching levels as low as 3.5×10^{-13} kg/s. Data from these experiments were initially gathered and the dimensionless mass flow rate S was plotted against Kn_m at different pressure ratios. For all the analyses conducted from here on the diameters considered for the microtubes were those determined indirectly from flow measurements, since it provides a more reliable representation of the channel geometry.

The experimental data shown in Figure 4.6 at a pressure ratio of $\Pi = 2$ were fitted using Eq. (3.42) with $A_{exp} = 1$ and considering a first-order slip velocity boundary condition in the Kn_m range 0 – 0.1 and a second-order condition in the range 0 – 0.3. In both cases, the fitting described the experimental results with significant accuracy in the rarefaction range considered, with the determination coefficients very close to unity. Table 4.2 presents the fitting coefficients at different pressure ratios together with the corresponding determination coefficients, R^2. In all the cases considered, the determination coefficient was not less than 0.999, confirming the adequacy of the Navier-Stokes equation with first- and second-order velocity slip boundary conditions in the rarefaction ranges considered. As expected, from Eq. (3.42), C_{exp} was dependent on Π, varying by approximately 10% among the considered cases, while B_{exp} was virtually insensitive to this parameter despite a clear difference observed among B_{exp} values associated with first- and second-order models. The uncertainties presented in Table 4.2 are associated only with the fitting of the experimental data. The coefficients B_{exp} and C_{exp} were related to the slip coefficients σ_P and σ_{2P} (Table 4.3), which were used to not only reduce the influence of the molecular model but also suppress the explicit dependence of the second-order coefficient on the pressure ratio.

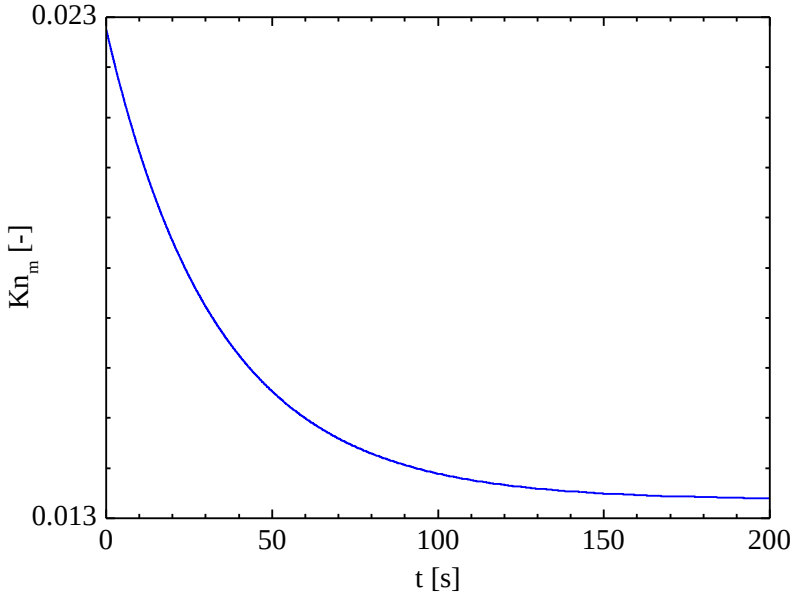

Figure 4.4 – Rarefaction level during a single experiment with N_2.

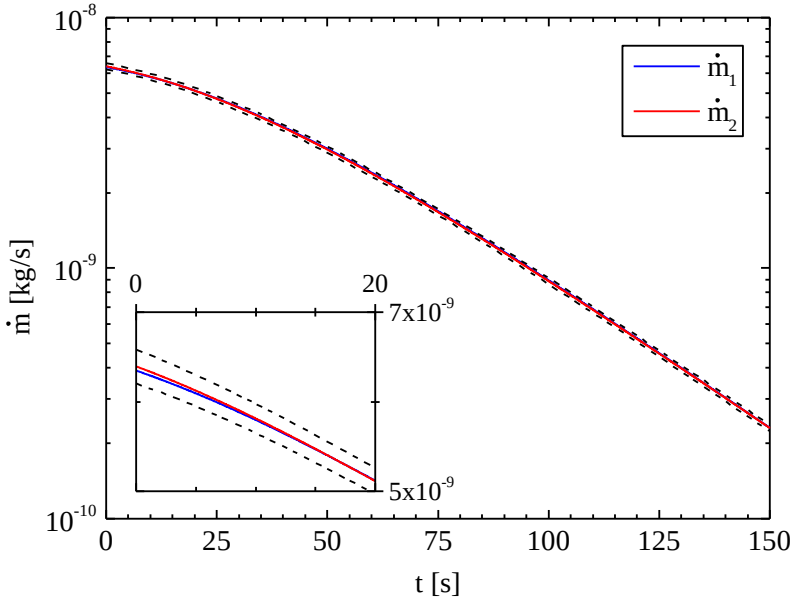

Figure 4.5 – Mass flow rate of N_2 along time for a single experiment. The black dashed lines represent the uncertainty range.

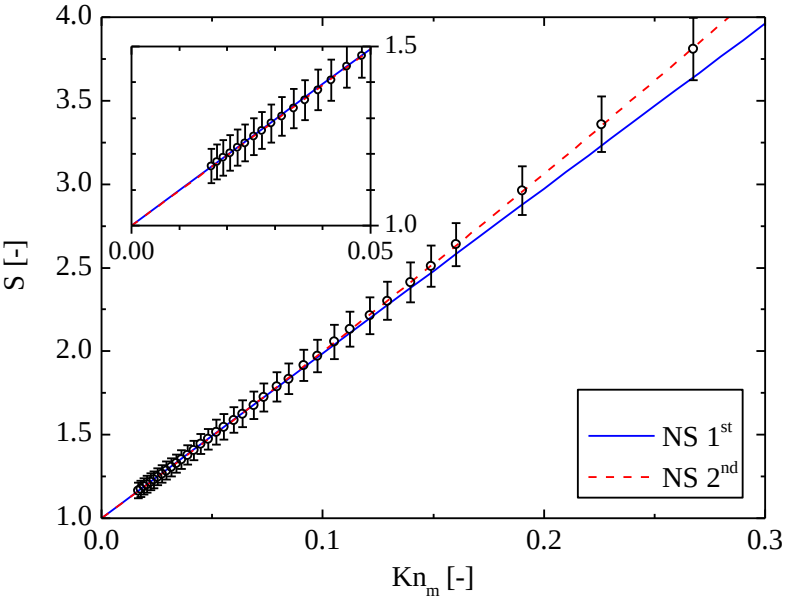

Figure 4.6 – Dimensionless mass flow rate of N_2 in microtube A at $\Pi = 2$.

Table 4.2 – Fitting coefficients of first- (top) and second-order (bottom) for N_2 according to the pressure ratio.

Π	B_{exp}	C_{exp}	R^2
2	9.872 ± 0.037	-	1.000
	9.661 ± 0.034	3.257 ± 0.188	1.000
3	9.877 ± 0.037	-	1.000
	9.699 ± 0.033	3.058 ± 0.162	1.000
5	9.897 ± 0.045	-	0.999
	9.703 ± 0.040	3.069 ± 0.218	1.000
8	9.913 ± 0.049	-	0.999
	9.723 ± 0.046	2.940 ± 0.236	1.000

As can be seen in Table 4.3, σ_P is virtually independent of Π, while σ_{2P} shows a strong dependence, changing by almost 43% in the considered pressure ratio range. The mean value of σ_P was $\bar{\sigma}_P = 1.096 \pm 0.005$ under the first-order slip velocity boundary condition and $\bar{\sigma}_P = 1.074 \pm 0.006$ under the second-order slip velocity boundary condition. Based on the BGK kinetic model, Albertoni *et al.* (1963) obtained $\sigma_P = 1.016$ by assuming complete accommodation of the molecules at the wall.

Using the same model, Loyalka *et al.* (1975) predicted σ_P for different values of α and found that $\sigma_P(\alpha = 0.9) = 1.2272$. By comparing these values with the experimental results obtained in the present work, the TMAC for nitrogen in a metallic microtube was found to be $0.9 < \alpha < 1$. The first-order term of Eq. (3.40) will be more extensively analyzed by comparing measurements of α with experimental results available in the literature.

Table 4.3 – Slip coefficients of first- (top) and second-order (bottom) for N_2 according to the pressure ratio.

Π	σ_P	σ_{2P}
2	1.094 ± 0.004	-
	1.070 ± 0.004	0.077 ± 0.004
3	1.094 ± 0.004	-
	1.074 ± 0.004	0.068 ± 0.004
5	1.096 ± 0.005	-
	1.075 ± 0.004	0.062 ± 0.004
8	1.098 ± 0.005	-
	1.077 ± 0.005	0.054 ± 0.004

Table 4.3 shows that σ_{2P} decreases with the pressure ratio Π. This trend was not observed by Ewart *et al.* (2007a) for He and Ar flows, and hence, it must be verified considering alternative gases and geometries. The mean value of σ_{2P} in the pressure ratio range analyzed is $\bar{\sigma}_{2P} = 0.065 \pm 0.017$ and can be compared with theoretical and experimental results available in the literature. However, there is no consensus on the magnitude of this coefficient. For example, the theoretical value proposed by Deissler (1964) is $\sigma_{2P} = 9\pi/32$, while the measurements of Ewart *et al.* (2007a) and Yamaguchi *et al.* (2011) indicated contrasting values. Ewart *et al.* (2007a) obtained $\sigma_{2P} = 0.231 \pm 0.057$, while Yamaguchi *et al.* (2011) found two values, $\sigma_{2P} = 0.031 \pm 0.005$ and $\sigma_{2P} = 0.064 \pm 0.012$, for microtubes of diameters D equal to 320 μm and 530 μm, respectively. Note that in both cases the authors analyzed N_2 flows in silica microtubes. The values obtained by Yamaguchi *et al.* (2011) are closer to the results of the present work. Besides the large variability of σ_{2P} found in the literature, it is known that this coefficient depends also of geometric characteristics of the channel and hence cannot be adopted as a universal coefficient as σ_P.

Many results of TMAC are available in the literature for N_2 flows and can be used for comparison. However, different formulations relating σ_P to α exist, which hampers a rigorous comparison. In addition, some variability in the results is expected since different channels and experimental setups are used. Therefore, experimental results for TMAC in the literature were compared with results obtained in the present work by considering the same equations adopted in each reference, which are presented in Section 1.2.1. However, a few studies considered stainless steel microtubes and results for channels of different materials were also included. Finally, it should be noted that surface characteristics may differ and sometimes such parameters are not described in the references. Table 4.4 shows the present results of TMAC as well as those found in the literature, with information about the surface material and its topological characteristics.

Table 4.4 – TMAC values found in the literature. First- (in parentheses) and second-order (without parenthesis) results are shown.

	α^M	α^L	α^S	Kn
a	0.908 ± 0.041	0.981 ± 0.041		$Kn_m \leq 0.3$
b			0.981 ± 0.041 (0.826 ± 0.010)	$Kn_m \leq 0.3$ $(Kn_m \leq 0.3)$
c			0.961 ± 0.005 (0.899 ± 0.009)	$Kn_m \leq 0.3$ $(Kn_m \leq 0.3)$
d			(0.901 ± 0.001)	$(Kn_m \leq 0.3)$
e	0.794 ± 0.022	0.857 ± 0.024	0.851 ± 0.024	$Kn_m \leq 0.3$
f	0.845 ± 0.038	0.913 ± 0.041	0.906 ± 0.041	$Kn_m \leq 0.3$
g	0.88 – 0.90		0.95 – 0.96	$Kn_m \leq 0.32$
h			(0.881 ± 0.003)	$\delta_m \geq 10$
i			(0.909 ± 0.003)	$\delta_m \geq 10$
j	**0.904 ± 0.003** **(0.894 ± 0.003)**	**0.978 ± 0.003** **(0.967 ± 0.003)**	**0.970 ± 0.003** **(0.960 ± 0.003)**	$\boldsymbol{Kn_m \leq 0.3}$ $\boldsymbol{(Kn_m \leq 0.1)}$

[a] Ewart *et al*. (2007a), fused silica, roughness below 0.1%.
[b] Perrier *et al*. (2011), fused silica, $D = 25\mu m$, roughness below 20nm.
[c] Perrier *et al*. (2011), fused silica, $D = 50\mu m$, roughness below 20nm.
[d] Perrier *et al*. (2011), fused silica, $D = 75\mu m$, roughness below 20nm.
[e] Yamaguchi *et al*. (2011), deactivated-fused silica, $D = 320$ μm.
[f] Yamaguchi *et al*. (2011), deactivated-fused silica, $D = 530$ μm.
[g] Yamaguchi (2012), stainless steel.
[h] Hadj Nacer *et al*. (2014), stainless steel with silica-based coating.
[i] Hadj Nacer *et al*. (2014), stainless steel.
[j] **Present work, stainless steel, roughness below 0.2%.**

Table 4.4 shows that the present results are very close to those of Ewart *et al*. (2007a) and Yamaguchi *et al*. (2012). The surface roughness of the microchannel used by Ewart *et al*. (2007a) is similar to that of the microchannel used in the present experiments. This is probably the reason for the agreement between the results, although the surface materials were different. On the other hand, Yamaguchi *et al*. (2012) used microtubes of the same material without any surface treatment as in the present experiments. Therefore, the agreement between the results was expected and confirms the adequacy of the experimental setup and procedure developed in this study. The second-order results of Perrier *et al*. (2011) are also in close agreement. However, the first-order solution presented discrepancies that can be attributed to the different rarefaction interval considered. In fact, the use of the first-order slip velocity boundary condition for $Kn_m > 0.1$, as adopted by Perrier *et al*. (2011), is not an accurate procedure. The same explanation cannot be given for the differences observed from the results of Hadj Nacer *et al*. (2014) with the same surface material. Nevertheless, such differences are small enough to be caused by the presence of contaminants or variability in the surface characteristics of the samples, which were not specified by the authors. Finally, significant differences are observed with the results of Yamaguchi *et al*. (2011). The authors did not provide the surface roughness but it should be around 20 nm, as verified by Perrier *et al*. (2011) for fused silica. Therefore, the relative roughness should be much lesser than 0.1%, and the surface would probably be similar to a specular surface, resulting in smaller values of α.

Values of α can be established for a wider rarefaction range through comparisons between measurements and theoretical results from the Boltzmann equation. Herein, measurements of the reduced mass flow rate G, as expressed by Eq. (3.44), are compared with the numerical results of the BGK kinetic model provided by Porodnov *et al*. (1978). Figure 4.7 shows the results for G as a function of the mean rarefaction parameter δ_m. It is clear from the theoretical curves for $\alpha = 0.90$, 0.98, and 1.00 that α is close to unity, between 0.98 and 1.00. In general terms, these results agree with those shown in Table 4.4 for the slip and early transitional flow regimes, especially when Eqs. (1.16) for α^L and (1.17) for α^S are considered to relate σ_P with α. This proves the higher accuracy of these equations compared to Eq. (1.15) used to estimate α^M, which does not consider the influence of the reflected molecules in the Knudsen layer.

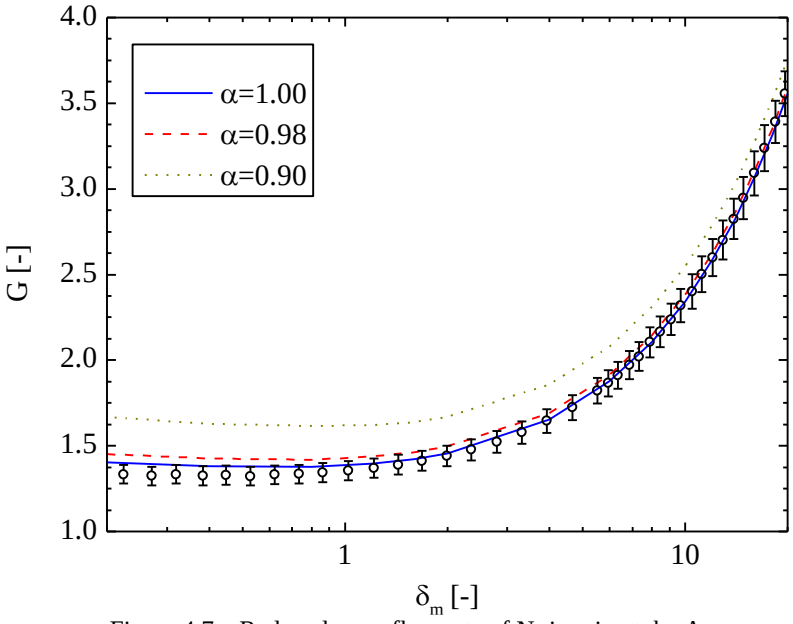

Figure 4.7 – Reduced mass flow rate of N_2 in microtube A.

In Figure 4.7, deviations between experimental data and the theoretical curve for $\alpha = 1$ are observed for small values of δ_m and can be attributed to limitations of the pressure sensors employed, since the pressures measured are very low in these experiments.

Concerning the variability of α in the rarefaction range, Arkilic *et al.* (2001) and Maurer *et al.* (2003) observed that for N_2 flows in rectangular channels, α decreases when Kn_m increases. The present results show a much smaller variation in α compared with the data of Arkilic *et al.* (2001) and Maurer *et al.* (2003). Actually, the theoretical curve for $\alpha = 1.00$ is within the uncertainty range of practically all experimental data. The same trend observed by Arkilic *et al.* (2001) and Maurer *et al.* (2003) was pointed out in a review by Agrawal and Prabhu (2008), who proposed that $\alpha = 1 - \log(1 + Kn^{0.7})$. However, this finding is questionable because it was based on a wide variety of experiments from the literature without proper characterization of all influential aspects on the experimental determination of α. In addition, the measurements available in the literature present a great dispersion.

Similar comparisons for N_2 in a wider rarefaction range were presented by Perrier *et al.* (2011) and Hadj Nacer *et al.* (2014), with solutions obtained via the BGK and S kinetic models, respectively. Note

that the dispersion of the measurements in Perrier *et al*. (2011) and Hadj Nacer *et al*. (2014) were much greater than in the present work. Perrier *et al*. (2011) found a good fitting between experimental data and theoretical curves (Figure 2.6) by considering complete accommodation, that is, $\alpha = 1.00$. Their results are in agreement with the present measurements, including those for the slip and early transitional flows (Table 4.4), validating the experimental setup and procedure developed in this work.

Figure 2.10 shows that the experimental data of Hadj Nacer *et al*. (2014) do not accurately follow the theoretical models, except for slightly rarefied flows where good agreement was found with numerical data for $\alpha = 1.00$. However, their results presented the strange behavior of crossing the theoretical curves as $\delta_m \to 0$, indicating inconsistency in the analyzed flows, especially at lower pressures. This may be the reason for the discrepancies between their results and the present measurements shown in Table 4.4.

In conclusion, regardless of the method and rarefaction range employed to extract α, the gas–surface interaction in the N_2 flow in a commercially available stainless steel surface with low roughness approaches the complete diffusive behavior, with α very close to unity. Overall, the results of this work closely agree with experimental data available in the literature even when considering the significant variability of the data available.

4.1.2 Effect of the experimental setup

An experimental analysis was conducted to identify any possible influence of the experimental setup on the results. To this end, experiments performed at UFSC, and described in the previous section, were repeated using another experimental setup available at the *Institut Clément Ader*, France, hereafter referred to as INSA. Measurements of the mass flow rates of N_2 in the same stainless steel microtube used previously (microtube A) are presented in Figure 4.8 in terms of G. Only the theoretical curves for $\alpha = 1.00$ and $\alpha = 0.98$ are shown for clarity.

As can be seen, the measurements obtained using both experimental setups closely agree with small differences within the uncertainty range. Therefore, the measurements can be considered unrelated to the experimental setup for the entire rarefaction range analyzed.

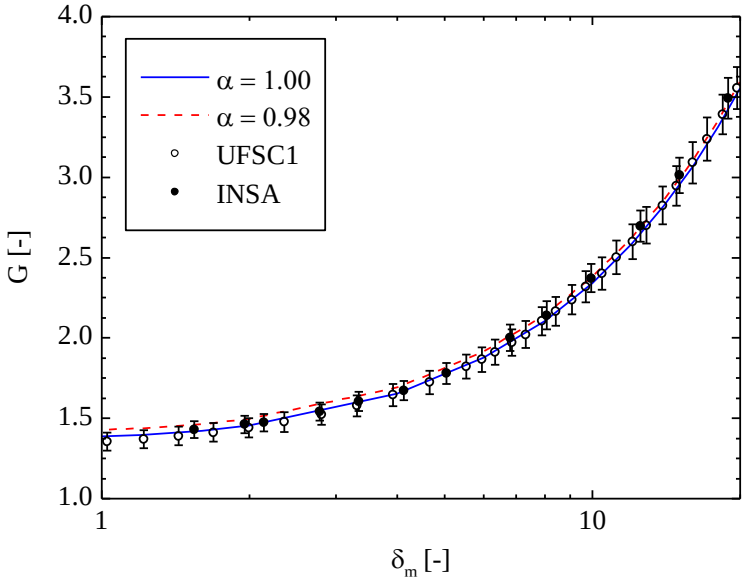

Figure 4.8 – Comparison of reduced mass flow rates for flows of N_2 in microtube A obtained using two different experimental setups.

4.1.3 Analysis of time-dependency

The effectiveness of the stationary assumption adopted for the mass flow rate measurements must be tested. To this end, the transient pressure measurements in the reservoirs were compared with numerical predictions obtained with the model proposed by Sharipov and Graur (2014), which models the transient flow in the tube as quasi-stationary with respect to the pressure variations in the reservoirs. In this model the flow rate in the channel is obtained from the solution of the linearized stationary kinetic equation for each cross section of the channel while the pressure variations at the inlet and outlet are determined from mass balances in the reservoirs. The authors claimed that the stationary assumption is valid for the flow through the channel when $L \gg D$. Under this condition, the time necessary to establish steady flow conditions in each cross section of the channel is significantly lesser than the time needed to establish steady flow conditions throughout the channel, allowing stationary solutions for each cross section. Figure 4.9 shows the numerical and experimental results for the pressure variation in the reservoirs for N_2 flows in microtube A. The numerical results for different rarefaction levels were obtained in collaboration with researchers from

Aix-Marseille University. Based on the results presented in Section 4.1.1, the simulations assumed $\alpha = 1$. Particularly, in this analysis the diameter of the microtube obtained from optical measurements (Table 3.1), $D = 438.6\ \mu m$, was used.

As can be seen from Figure 4.9, the numerical and experimental results closely agree for all rarefaction levels. The largest deviation was 0.8% for the lower rarefied case (Figure 4.9a) and 3.3% for the higher rarefied case (Figure 4.9d), which in absolute terms corresponds to approximately 0.3 Pa. Such deviations are small and can be partly associated with uncertainties in the measurements of the microtube dimensions and volumes of the reservoirs and partly associated with the uncertainties of the numerical calculations.

This demonstrates that the stationary flow model in the channel captures the transient behavior of the system with accuracy, and hence, the transient nature of the flow can be neglected for all pressure levels considered in the present study. Consequently, the mass flow rate measurements performed using Eq. (3.25) approach the stationary condition.

4.1.4 Conductance

As mentioned in Section 3.1.2.1, the conductance of channels is a parameter commonly employed in the vacuum technology field. This parameter can be directly determined from measurements with the dynamic constant volume technique for the particular case in which both reservoirs have the same volume. In this case, the mean pressure P_m in the system is constant during the experiment whose characteristic time τ is determined by fitting the pressure difference ΔP along time using Eq. (3.11). Then, the conductance C is obtained from τ via Eq. (3.12). The results for N_2 flow in microtube A were obtained with the experimental setup INSA and are shown in Figure 4.10 as a function of P_m. Although a flow cannot be completely characterized only by the P_m, Sharipov (1999) showed that G can be determined based only on δ_m (and consequently P_m) within an error of 1%. Similarly, C can also be described solely in terms of P_m within an acceptable error, being weakly dependent on other variables. Theoretical limits for the conductance in the hydrodynamic ($C = \pi D^4 P_m / 128 \mu L$) and free molecular flow regimes ($C = D^3 \sqrt{2\pi RT}/6L$) are indicated in the same figure by dashed lines. The results obtained by a semi-empirical model proposed by Knudsen (1909) are also included and are given by:

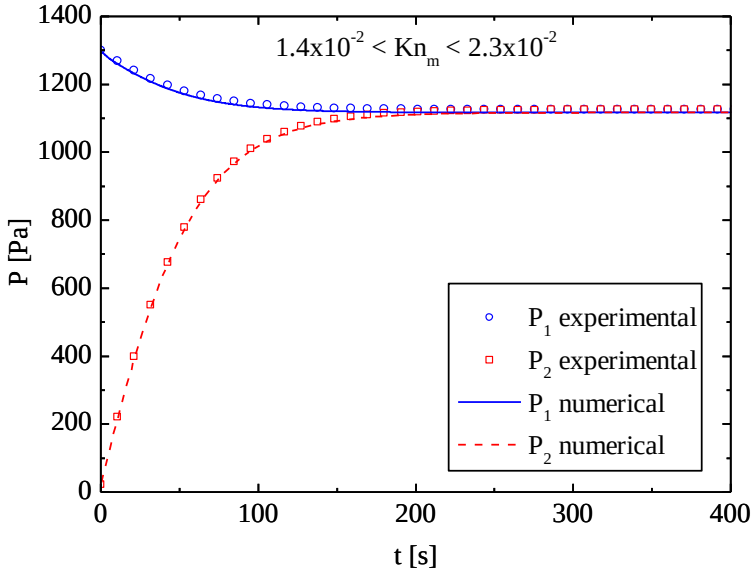

(a)

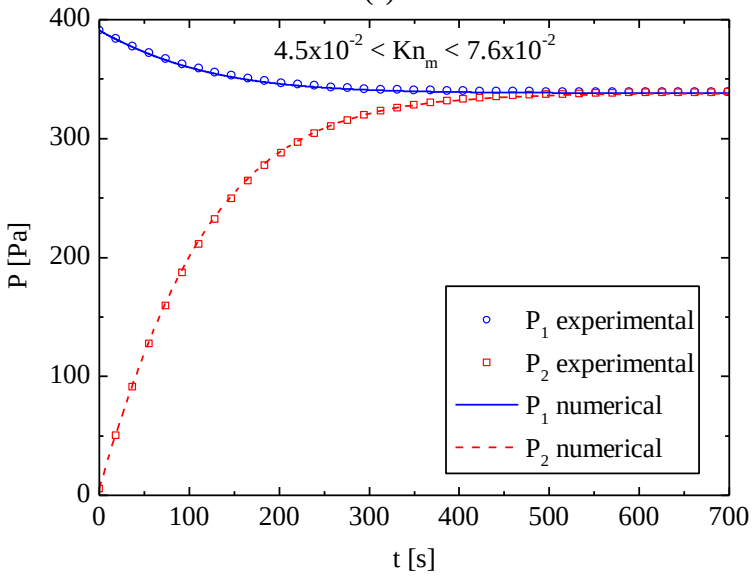

(b)

Figure 4.9 – Comparison of numerical and experimental pressure variation with time for N_2 flows. Numerical results obtained in collaboration with Aix-Marseille University using the model developed by Sharipov and Graur (2014). The uncertainty in the pressure measurements is approximately 0.2%.

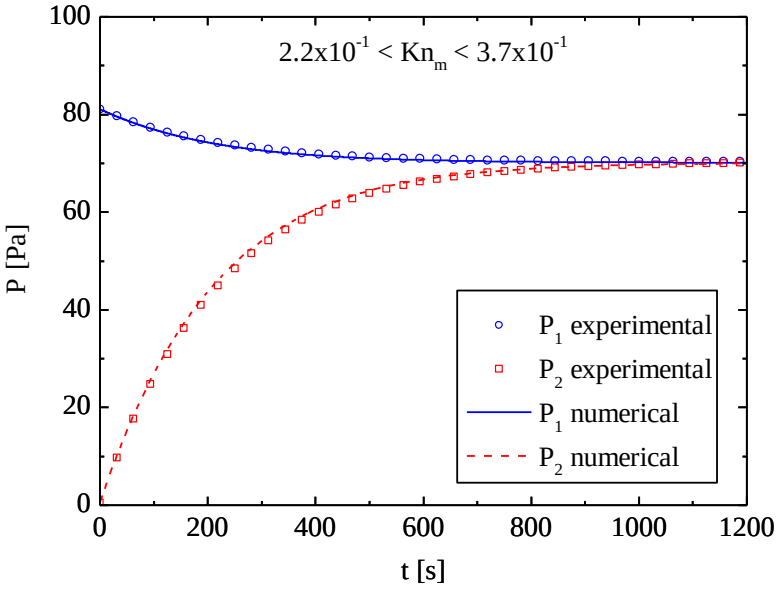

(c)

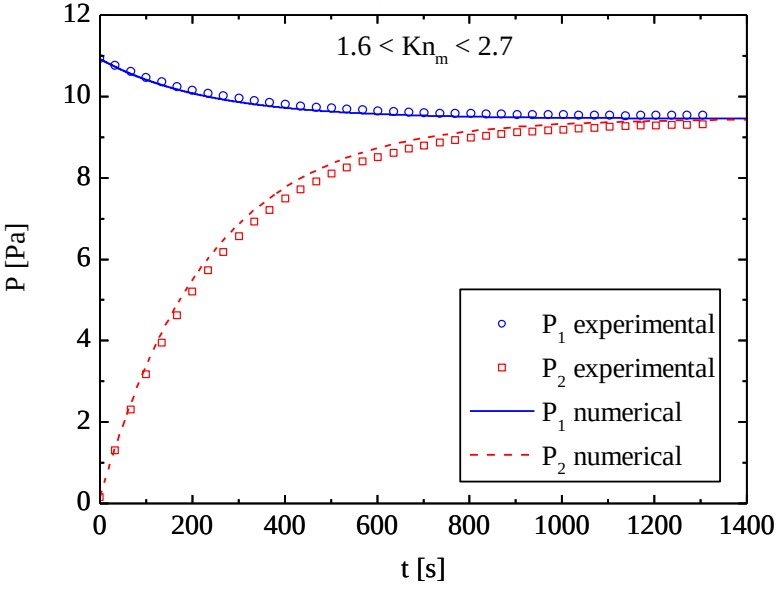

(d)

Figure 4.9 (Continued).

$$C = \frac{\pi}{8}\frac{(D/2)^4}{\mu}\frac{P_m}{L} + \frac{4}{3}\frac{(D/2)^3}{L}\sqrt{2\pi RT}\frac{\left(1 + 2.507(D/2\lambda_m)\right)}{\left(1 + 3.095(D/2\lambda_m)\right)}\,, \qquad (4.1)$$

where λ_m represents the average mean free path. Equation (4.1) combines expressions for the conductance in the hydrodynamic and free molecular flow regimes with an interpolating function determined by fitting experimental data in the transitional flow regime.

Each experimental point in Figure 4.10 represents an experiment. A typical pressure fitting from a single experiment for the case $P_m = 6.14\ kPa$ is shown in Figure 4.11. In all cases, the determination coefficient was greater than 0.998 regardless of the mean pressure.

From Figure 4.10, it is possible to see that the experimental measurements agreed with the theoretical limits, except for pressures below approximately 30 Pa. These deviations of the experimental data are due to limitations of the pressure transducers for measuring low pressures and due to uncertainties associated with Eq. (4.1). Nevertheless, the mean deviation, calculated as

$$\overline{\Delta C} = \frac{1}{n}\sum_{i=1}^{n}\frac{\left|C_{exp}^{i}(P_m) - C_{th}^{i}(P_m)\right|}{C_{th}^{i}(P_m)}\,, \qquad (4.2)$$

was around 3%, where C_{exp}^{i} is the conductance obtained from the experiment for a particular mean pressure P_m and C_{th}^{i} is the corresponding theoretical value given by Eq. (4.1).

Thus, considering the virtually complete accommodation of the N_2 molecules at the stainless steel surface shown in Section 4.1.1, the results of the Knudsen's model (Knudsen, 1909) are in close agreement with the experimental data even in the transitional flow regime. This is an interesting aspect since the conductance obtained for a particular rarefaction condition, represented by the mean pressure P_m, can be used to determine the mass flow rate for any pressure difference. This is illustrated in Figure 4.12, where results from Eq. (4.1) and from measurements are shown for three pressure differences. The expected constant value under free molecular flow regime and the linear behavior in the hydrodynamic regime are evident from these results. The experimental results and those obtained by Eq. (4.1) are in close agreement.

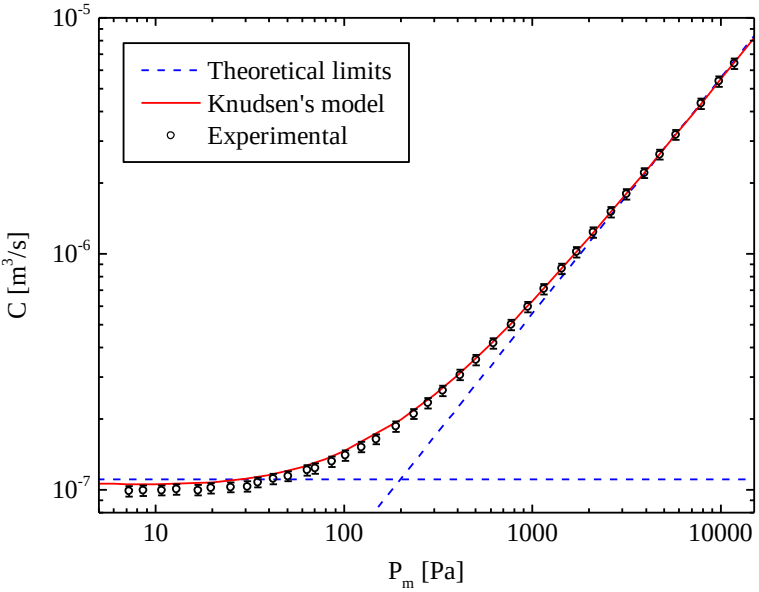

Figure 4.10 – Conductance of microtube A for flows of N_2.

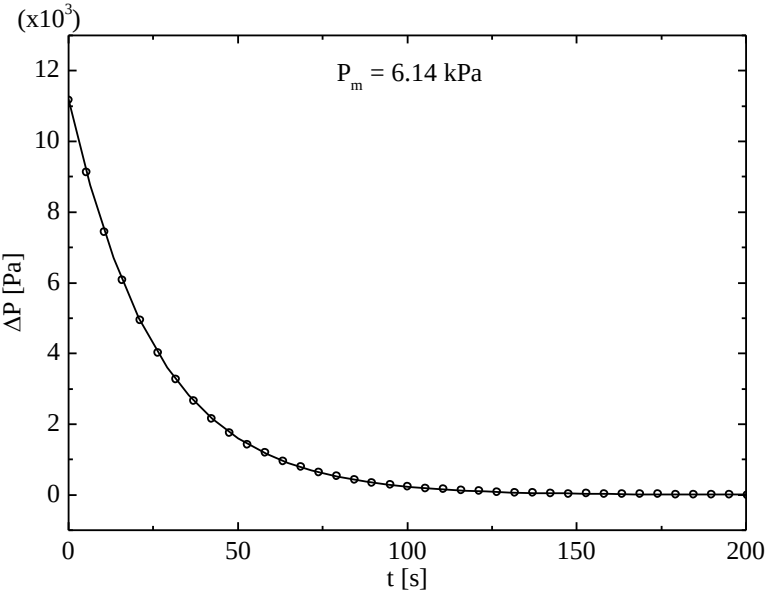

Figure 4.11 – Fitting of pressure difference for N_2 flows in microtube A for a single experiment in which $V_1 = V_2$.

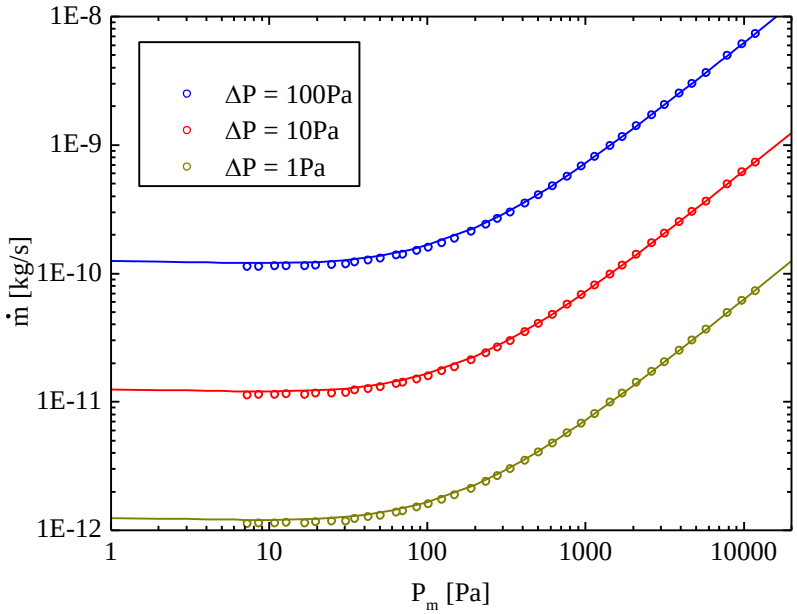

Figure 4.12 – Mass flow rates of N_2 in microtube A predicted from conductance data for different ΔP. The symbols represent experimental data obtained in this work while the lines represent data obtained from the correlation proposed by Knudsen (1909). The uncertainty of the mass flow rate is approximately 3%.

4.2 EXPERIMENTAL VALIDATION OF THE EXPERIMENTAL SETUP UFSC2

Nitrogen flows were also analyzed through the rectangular cross section microchannel described in Section 3.2.2 with aspect ratio close to 1 ($h/w \cong 1.1$). As previously done for the other cases, the measurements were initially fitted, this time using Eq. (3.52), and the slip and accommodation coefficients were extracted and compared with data from the literature. Subsequently, the measurements were also compared with theoretical predictions obtained with the BGK kinetic model for different values of α.

Figure 4.13 shows the results of the dimensionless mass flow rate, S, at $\Pi = 2$. Again, the first-order model was employed up to $Kn_m = 0.1$, while the second-order model was considered for $Kn_m \leq 0.3$. The fitting coefficients as well as the corresponding determination coefficients are shown in Table 4.5. Regardless of the pressure ratio and the order of the

model adopted, the determination coefficients for the curve fitting, R^2, were greater than 0.999. The slip coefficients at different pressure ratios, Π, are shown in Table 4.6 considering $h/w = 1$.

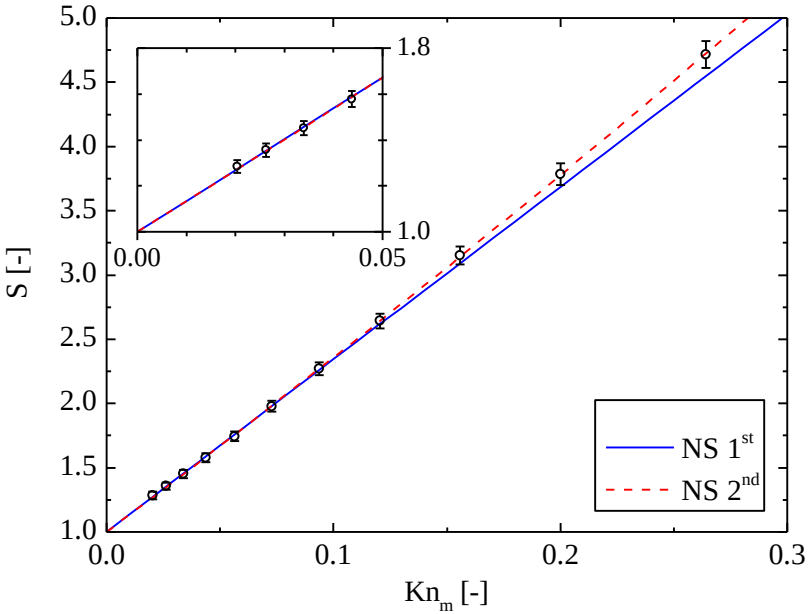

Figure 4.13 - Dimensionless mass flow rate of N_2 in a square cross section microchannel of stainless steel at $\Pi = 2$.

Table 4.5 - Fitting coefficients of first- (top) and second-order (bottom) for N_2 according to the pressure ratio in a square cross section microchannel of stainless steel.

Π	B_{exp}	C_{exp}	R^2
2	13.43 ± 0.15	-	0.999
	13.25 ± 0.14	3.176 ± 0.639	1.000
3	13.41 ± 0.19	-	0.999
	13.30 ± 0.15	3.139 ± 0.631	1.000
5	13.46 ± 0.22	-	0.999
	13.26 ± 0.21	3.603 ± 1.085	1.000
8	13.48 ± 0.23	-	0.999
	13.29 ± 0.23	3.524 ± 1.102	1.000

Table 4.6 - Slip coefficients of first- (top) and second-order (bottom) for N2 according to the pressure ratio in a square cross section microchannel of stainless steel.

Π	σ_P	σ_{2P}
2	1.488 ± 0.017	-
	1.468 ± 0.016	0.084 ± 0.017
3	1.486 ± 0.021	-
	1.473 ± 0.017	0.079 ± 0.016
5	1.491 ± 0.024	-
	1.469 ± 0.023	0.082 ± 0.025
8	1.493 ± 0.025	-
	1.472 ± 0.025	0.073 ± 0.023

As can be seen from Table 4.6, the σ_P value does not significantly change with the pressure ratio or when extracted from first- or second-order models. The influence of the pressure ratio on σ_{2P} is also not evident owing to measurement uncertainties. The mean values of σ_P for the first- and second-order models are $\bar{\sigma}_P = 1.490 \pm 0.026$ and $\bar{\sigma}_P = 1.470 \pm 0.025$, respectively, which are greater than those obtained in Section 4.1.1 for a microtube. This is reflected in the smaller values of α shown in Table 4.7. The importance of the second-order term in relation to the first-order term for the analyzed flow can be estimated by the relationship σ_{2P}/σ_P. In this case, similar results were obtained for the microtube $(\bar{\sigma}_{2P}/\bar{\sigma}_P)_t = 0.061$ and the microchannel $(\bar{\sigma}_{2P}/\bar{\sigma}_P)_{ch} = 0.054$. This similarity was also found by Graur *et al*. (2009), but they predicted that the second-order effect plays a more determinant role with $(\sigma_{2P}/\sigma_P)_t = 0.217$ and $(\sigma_{2P}/\sigma_P)_{ch} = 0.298$. Note that Graur *et al*. (2009) adopted an aspect ratio (h/w) of approximately 0.019 for the channel, whereas the aspect ratio in the present study is close to 1 (Table 3.2).

It can be noted from Table 4.7 that the values of α obtained in the present work are smaller than the results available in the literature for N_2 flows in rectangular microchannels. In fact, no other study has presented such small values of α, even when surfaces with reduced roughness were employed. The closest results were obtained by Hadj Nacer *et al*. (2014) over surfaces covered with a thin gold coating. However, as discussed in Section 2.1.2 and shown in Figure 2.9, the channel employed by Hadj Nacer *et al*. (2014) had a very irregular rectangular cross section.

Table 4.7 - TMAC values found in the literature. First-order results are shown in parentheses.

	α^M	α^L	α^S	Kn
a	(0.80 – 0.95)			$Kn_o \leq 0.36$
b	0.87 ± 0.03			$Kn_m \leq 0.6$
c	0.93			$Kn_o \leq 0.25$
d			0.956 ± 0.005 (0.889±0.004)	$Kn_m \leq 0.3$ $(Kn_m \leq 0.3)$
e			(0.845±0.004)	$(Kn_m \leq 0.1)$
f	**0.752 ± 0.008** **(0.746 ± 0.008)**	**0.811 ± 0.009** **(0.804 ± 0.009)**	**0.806 ± 0.009** **(0.799 ± 0.009)**	$\boldsymbol{Kn_m \leq 0.3}$ $\boldsymbol{(Kn_m \leq 0.1)}$

[a] Arkilic *et al*. (2001), silicon (1.33 μm × 52.3 μm), roughness below 0.65nm.
[b] Maurer *et al*. (2003), glass and silicon (1.14 μm x 200 μm), estimated roughness 20 nm.
[c] Colin *et al*. (2004), glass and silicon (4.48 μm × 51.6 μm, 1.88 μm × 21.2 μm, 1.16 μm × 21.0 μm, 0.54 μm × 50.0 μm).
[d] Graur *et al*. (2009), silicon (9.38 μm × 492 μm), roughness below 20 nm.
[e] Hadj Nacer *et al*. (2011), silicon coated with gold (27.84 μm × 52.23 μm), estimated roughness 0.87 nm.
[f] Present work, stainless steel (340.8 μm × 309.5 μm), roughness below 0.18μm.

The α values obtained for the rectangular microchannel are much smaller than the values obtained for the microtubes (Section 4.1.1). This is unexpected since the gas and surface material were virtually the same in both analyses. Some aspects may have affected the present results, with the tightness of the channel probably being the most important one. In other similar experimental setups, the microchannels were sealed by bonding the top surface to the plate containing the etched channel. In the present work, both surfaces were fastened together using screws. Although this configuration makes it easy to open the channel when necessary, it is more difficult to guarantee tightness of the channel. Therefore, the possibility of gas pockets in the contact area between the plates, which would affect the cross section of the channel and increase the flow, cannot be eliminated.

The actual cleanliness of the microchannel could also affect the results. For instance, the microtube was employed in its original state without performing any special surface cleaning. On the other hand, the microchannel with rectangular cross section was cleaned in an ultrasonic bath of acetone to remove impurities from the manufacturing process.

This issue was clarified through experiments and comparisons of results for microtubes with and without cleaning with acetone and no difference was observed in terms of mass flow rate. Finally, some discrepancy may be associated with the fact that the channel cross section is not exactly square as it was considered in the model.

Figure 4.14 compares the experimental data with theoretical predictions obtained by Hadj Nacer *et al.* (2012) using the BGK kinetic model. As expected, from the extracted values of α^L and α^S in the slip flow regime using Eqs. (1.16) and (1.17), respectively, the results for $\alpha = 0.80$ show a better agreement with the experimental data. Figure 4.14 shows that the curves obtained experimentally and theoretically have the same slope at different rarefaction levels even under highly rarefied conditions.

For all the experiments performed with the rectangular cross section microchannel, it was verified that $Re \leq 1.6$ and $Ma \leq 0.12$ at the channel outlet.

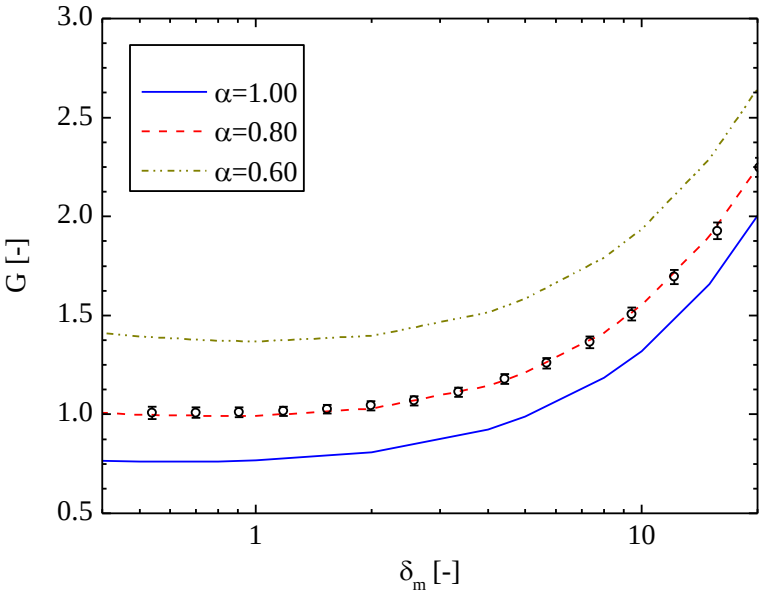

Figure 4.14 – Reduced mass flow rate of N_2 in a square cross section microchannel of stainless steel.

4.3 GAS EFFECT

The effect of the gas chemical composition on the gas–surface interaction was investigated using the same microchannel in order to mitigate secondary effects induced by variabilities in the geometry or surface characteristics. This section analyzes the flows of polyatomic gases R134a and R600a in microtube A. This microtube was used in the measurements described in Section 4.1.1 for N_2 flows, and the results will be used as reference for comparison with data of the other gases.

Initially, the measurements of the dimensionless mass flow rate, S, were fitted to Eq. (3.41) with $A_{exp} = 1$ by considering first- and second-order slip velocity boundary conditions for Kn_m from 0 to 0.1 and from 0 to 0.3, respectively. The results of S at $\Pi = 2$ are presented in Figure 4.15 and the fitting coefficients for different pressure ratios are presented in Table 4.8.

As previously observed for N_2 flows, the first- and second-order expressions fit the experimental data well, with determination coefficients greater than 0.999 for R134a and greater than 0.996 for R600a. Moreover, it is interesting to note that in both cases, the experimental results of S tend to unity when $Kn_m \to 0$, as expected. The same verification is meaningless for N_2 flows since the microtube diameter was adjusted to obtain $S = 1$ when $Kn_m \to 0$. Tables 4.2 and 4.8 show that the experimental coefficient of first-order B_{exp} does not significantly change according to the type of gas. In contrast, second-order effects represented by the coefficient C_{exp} can vary considerably and are more important for flows of R600a, followed by N_2 and finally R134a.

Table 4.9 presents the slip coefficients σ_P and σ_{2P} for R134a and R600a. The values of σ_{2P} are quite different for both gases and slightly decrease as the pressure ratio is increased. The values of σ_P are close to the values obtained for N_2, with the values for R600a very close to the theoretical value 1.016 estimated by Albertoni *et al.* (1963) considering complete accommodation of the molecules at the wall.

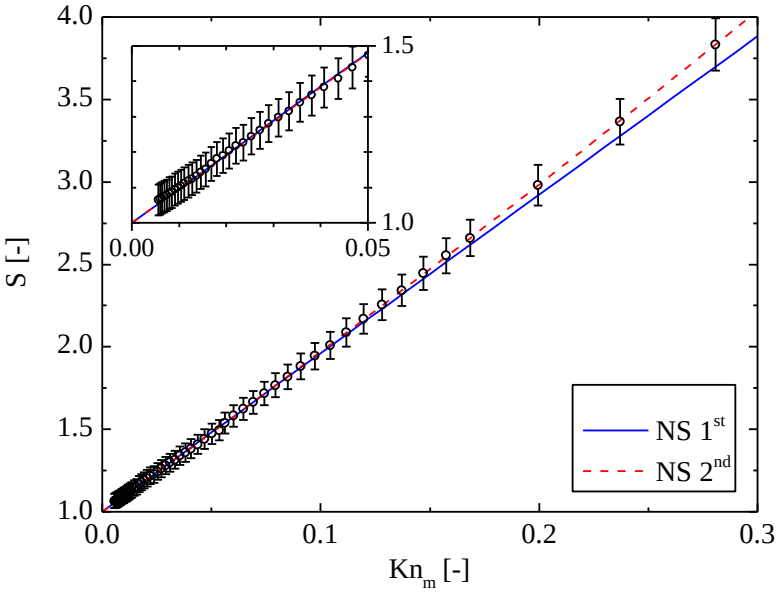

(a)

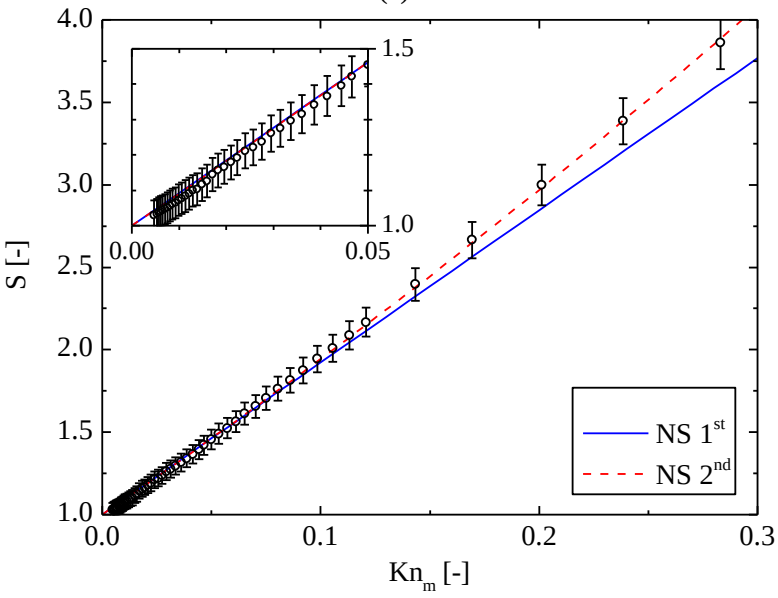

(b)

Figure 4.15 – Dimensionless mass flow rate of (a) R134a and (b) R600a in microtube A at $\Pi = 2$.

Table 4.8 – Fitting coefficients of first- (top) and second-order (bottom) for R134a and R600a according to the pressure ratio in microtube A.

Π	B_{exp}	C_{exp}	R^2
R134a			
2	9.611 ± 0.050	-	0.999
	9.484 ± 0.050	2.171 ± 0.262	1.000
3	9.625 ± 0.052	-	0.999
	9.491 ± 0.056	2.276 ± 0.324	1.000
5	9.620 ± 0.061	-	0.999
	9.502 ± 0.058	2.295 ± 0.303	1.000
8	9.612 ± 0.067	-	0.999
	9.509 ± 0.060	2.296 ± 0.296	1.000
R600a			
2	9.230 ± 0.123	-	0.996
	9.022 ± 0.120	4.155 ± 0.604	0.999
3	9.217 ± 0.119	-	0.996
	8.998 ± 0.113	4.614 ± 0.626	1.000
5	9.241 ± 0.113	-	0.996
	9.060 ± 0.102	4.284 ± 0.520	1.000
8	9.230 ± 0.108	-	0.997
	9.019 ± 0.105	4.706 ± 0.613	1.000

Again, σ_P is insensitive to the pressure ratio, while σ_{2P} shows a small variation. Nevertheless, no evident correlation was observed between the variations of both parameters. The mean values of the first slip coefficients for R134a are $\bar{\sigma}_P = 1.066 \pm 0.007$ (first-order model) and $\bar{\sigma}_P = 1.052 \pm 0.007$ (second-order model). The mean value of the second slip coefficient is $\bar{\sigma}_{2P} = 0.048 \pm 0.010$ (second-order model). For R600a, these values are $\bar{\sigma}_P = 1.022 \pm 0.014$ (first-order model) and $\bar{\sigma}_P = 1.000 \pm 0.015$ (second-order model), whereas the mean value of the second slip coefficient is $\bar{\sigma}_{2P} = 0.094 \pm 0.020$ (second-order model). The smaller values of the first slip coefficient result in greater values of α for both gases compared with N_2, as summarized in Table 4.10. The table also presents the results available in the literature for polyatomic gases. Only studies that also considered N_2 flows were chosen to provide a useful reference. The rarefaction ranges specified in Table 4.4 were adopted in these analyses.

Table 4.9 – Slip coefficients of first- (top) and second-order (bottom) for R134a and R600a according to the pressure ratio in microtube A.

Π	σ_P	σ_{2P}
	R134a	
2	1.065 ± 0.006 1.051 ± 0.006	- 0.051 ± 0.006
3	1.066 ± 0.006 1.051 ± 0.006	- 0.051 ± 0.007
5	1.066 ± 0.007 1.053 ± 0.006	- 0.047 ± 0.006
8	1.065 ± 0.007 1.053 ± 0.007	- 0.042 ± 0.005
	R600a	
2	1.022 ± 0.014 0.999 ± 0.014	- 0.098 ± 0.014
3	1.021 ± 0.013 0.997 ± 0.013	- 0.103 ± 0.014
5	1.024 ± 0.013 1.004 ± 0.011	- 0.087 ± 0.011
8	1.022 ± 0.012 0.999±0.012	- 0.086±0.011

The results in Table 4.10 indicate similar behaviors for O_2 and N_2 with respect to the surfaces analyzed, as suggested by the approximately equal values of α. The work of Hadj Nacer *et al*. (2014) is of special interest since they tested channels similar to those analyzed in the present investigation and also considered the polyatomic molecule of CO_2. In the case of a stainless steel microtube with silica-based coating, Hadj Nacer *et al*. (2014) observed that CO_2 presents a more diffuse behavior. This result contrasts with most results for monoatomic gases from the literature such as those obtained by Ewart *et al*. (2007a) and Perrier *et al*. (2011) that indicate higher values of α for lighter gases. However, in the case of a simple stainless steel surface, the results for CO_2 are very similar to those for N_2. A similar behavior was found in the present analysis for R134a and R600a, which are heavier than N_2 but have TMAC values close to those of N_2.

Table 4.10 – TMAC values found in the literature. First-order results are shown in parentheses.

	α^M	α^L	α^S	Gas
a	0.794 ± 0.022	0.857 ± 0.024	0.851 ± 0.024	N_2
b	0.794 ± 0.021	0.857 ± 0.024	0.851 ± 0.023	O_2
c	0.845 ± 0.038	0.913 ± 0.041	0.906 ± 0.041	N_2
d	0.836 ± 0.035	0.904 ± 0.038	0.897 ± 0.038	O_2
e	0.88 – 0.90		0.95 – 0.96	N_2
f	0.88 – 0.90		0.94 – 0.96	O_2
g			(0.881 ± 0.003)	N_2
h			(0.951 ± 0.004)	CO_2
i			(0.909 ± 0.003)	N_2
j			(0.907 ± 0.003)	CO_2
k	**0.904 ± 0.003 (0.894 ± 0.003)**	**0.978 ± 0.003 (0.967 ± 0.003)**	**0.970 ± 0.003 (0.960 ± 0.003)**	**N_2**
l	**0.914 ± 0.003 (0.908 ± 0.003)**	**0.989 ± 0.004 (0.982 ± 0.004)**	**0.982 ± 0.004 (0.974 ± 0.003)**	**R134a**
m	**0.940 ± 0.007 (0.929 ± 0.007)**	**1.016 ± 0.008 (1.004 ± 0.007)**	**1.008 ± 0.008 (0.997 ± 0.007)**	**R600a**

[a, b] Yamaguchi *et al*. (2011), deactivated-fused silica, $D = 320$ μm.
[c, d] Yamaguchi *et al*. (2011), deactivated-fused silica, $D = 530$ μm.
[e, f] Yamaguchi (2012) *et al*., stainless steel.
[g, h] Hadj Nacer *et al*. (2014), stainless steel with silica-based coating.
[i, j] Hadj Nacer *et al*. (2014), stainless steel.
[k, l, m] Present work, stainless steel, roughness below 0.2%.

Note that the value of α^L for R600a considering a second-order model is slightly greater than the theoretical maximum $\alpha = 1$, which occurs for complete accommodation. The results show that the assumption of complete accommodation at the wall is adequate for all gases when formulations that are more precise for the slip coefficient are adopted, such as Eqs. (1.16) and (1.17).

The results for R134a and R600a were also compared to the BGK model solutions obtained by Porodnov *et al*. (1978) for a wide rarefaction range (Figure 4.16). Similar to the case of N_2, the experimental data for R134a and R600a are well represented by the theoretical curve for $\alpha = 1$. Nevertheless, some disagreement is observed for both gases under more rarefied conditions ($\delta_m < 3$). Note that such conditions are associated with measurements at very low pressure levels with errors due to limitations of the instrumentation employed.

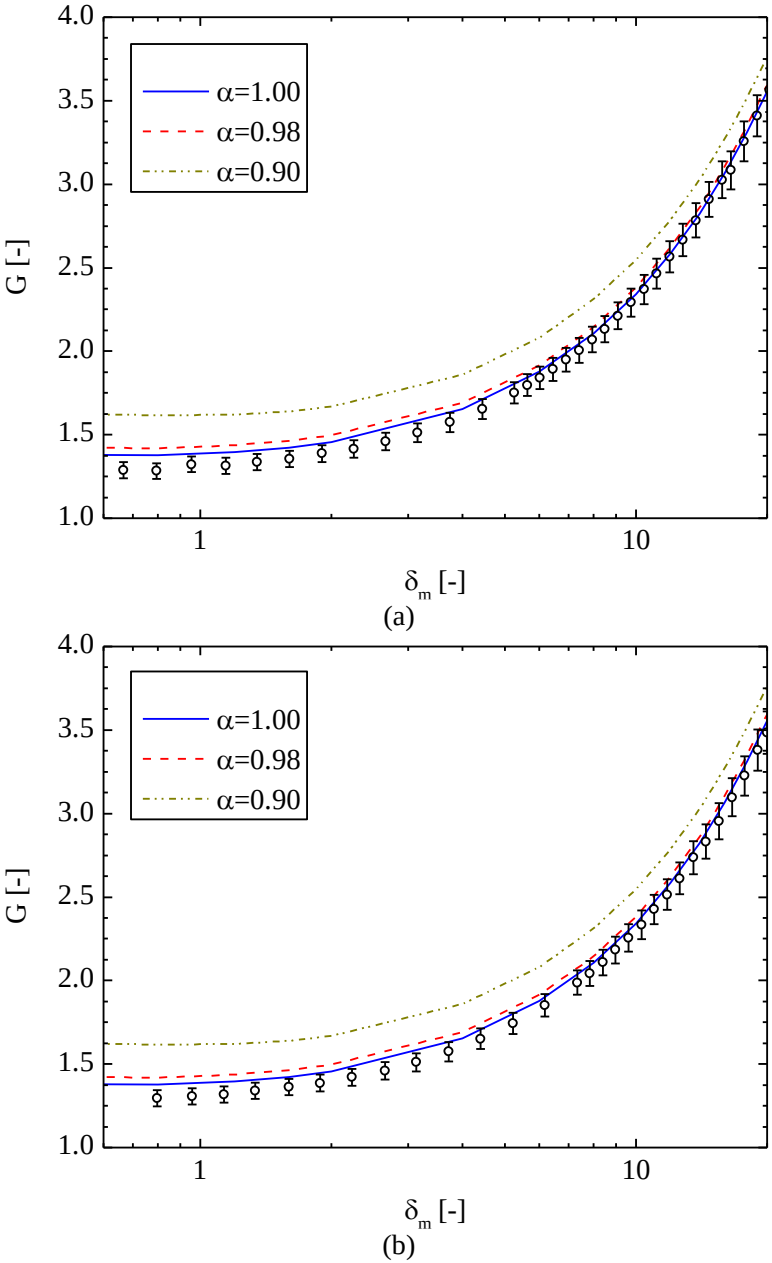

Figure 4.16 – Reduced mass flow rate of (a) R134a and (b) R600a in microtube A.

The mass flow rates of N_2, R134a and R600a were compared in the entire rarefaction range, keeping the pressure difference between the inlet and outlet of the channel equal to 100 Pa. Figure 4.17a shows that the largest mass flow rate occurs for R134a. Therefore, as far as applications in compressor valves are concerned, R134a is more susceptible to leakage than R600a, which in turn is more critical than N_2. This is an outcome of the higher molar weight, M, of R134a (102.03 g/mol) compared with R600a (58.12 g/mol) and N_2 (28.01 g/mol).

On the other hand, Figure 4.17b indicates an opposite trend for the molar flow rate $\dot{n}$ $(= \dot{m}/M)$, with more molecules of N_2 flowing in the microchannel followed by R600a and R134a. This behavior can be macroscopically explained by the relationship between the mass flow rate for a particular rarefaction condition, given by Eq. (3.40), and the molar weight M, which can be determined using Eq. (1.36) to relate the gas pressure with its mean free path. Considering that Kn_m and ΔP are constant for a particular condition, it is possible to show that $\dot{m} = \dot{m}(\sqrt{M})$. In this case, the mass flow rate must increase with M. On the contrary, $\dot{n} = \dot{n}(1/\sqrt{M})$ and the molar flow rate must decrease with M. For this particular case, the viscosity does not affect the difference found between the gases. According to the results, the differences observed between the accommodation coefficients of the gases are not sufficient to alter the effects of the macroscopic parameter M on the flow.

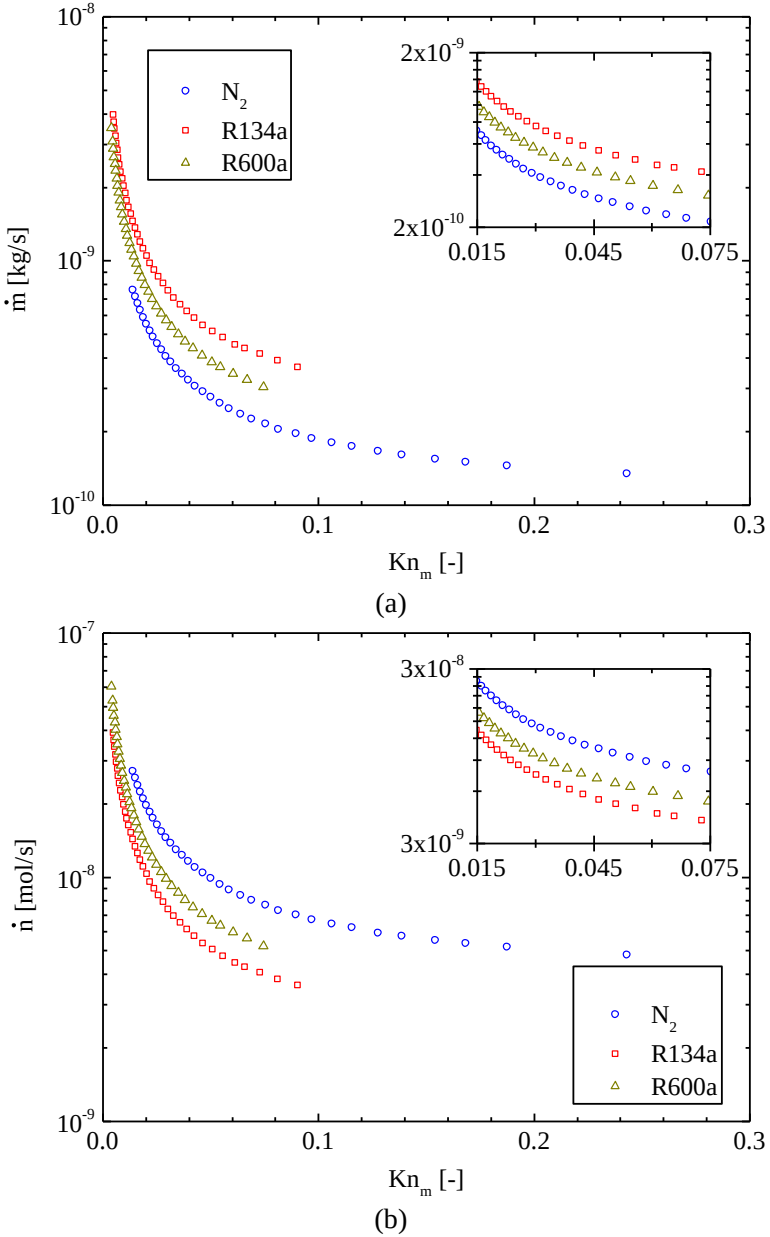

Figure 4.17 – Mass (a) and molar (b) flow rates of N_2, R134a, and R600a in microtube A for a pressure difference of 100Pa. The uncertainty of $\dot{m}$ and $\dot{n}$ is 3%.

4.4 MATERIAL AND SURFACE EFFECT

The analysis presented in the previous sections was extended to flows of N_2, R134a and R600a in microtubes B and C composed of copper and brass, respectively. The fitting and slip coefficients extracted from the slightly rarefied portion of the rarefaction range considered, that is, for $Kn_m \leq 0.1$ in the case of first-order and $Kn_m \leq 0.3$ in the case of second-order models, are shown in Appendix B. The mean values of the slip coefficients are presented in Table 4.11, while the corresponding values of α are shown in Table 4.12 for the first- and second-order models considering Eq. (1.17) to relate σ_P and α.

The values presented in Table 4.12 are very close to each other and to unity. Therefore, we can conclude that the gas–surface interaction for the gases and materials analyzed can be well described by a completely diffuse one. Note that values slightly greater than unity were obtained for microtube C regardless of the type of gas and may be associated with its high surface roughness. Such irregularities could introduce perturbations into the flow that are not considered in the present theoretical modeling. The incorrect determination of the microtube diameter could also be responsible for TMAC values above unity. However, this effect is less likely because two distinct measurement techniques provided similar results. The diameter determined from flow measurements was used in the analysis.

These experimental results were compared in the entire rarefaction range with solutions from the BGK kinetic equation for microtubes B and C (Figure 4.18). As already verified for microtube A, the results for the reduced mass flow rate, G, of all gases in microtube B are very close to each other and to the theoretical predictions with $\alpha = 1$. On the other hand, the reduced mass flow rates of all gases in microtube C are lower than those predicted theoretically with $\alpha = 1$. Again, this deviation may be associated with the high surface roughness or, less likely, with inaccuracies in the determination of the microtube diameter. It was verified that in all cases, the gas–surface interaction showed no significant difference with respect to gas chemical composition.

For all the experiments presented so far, including those with microtubes A, B and C and with gases N_2, R134a and R600a, it was verified that $Re \leq 11.6$ and $Ma \leq 0.23$ at the channel outlet.

Table 4.11 – Mean slip coefficients for flows of N_2, R134a and R600a in microtubes B and C.

Gas	1st-order	2nd-order	
	$\bar{\sigma}_P$	$\bar{\sigma}_P$	$\bar{\sigma}_{2P}$
Microtube B			
N_2	1.083 ± 0.017	1.069 ± 0.015	0.053 ± 0.030
R134a	1.088 ± 0.011	1.074 ± 0.012	0.030 ± 0.014
R600a	1.048 ± 0.007	1.027 ± 0.009	0.070 ± 0.017
Microtube C			
N_2	0.952 ± 0.016	0.934 ± 0.014	0.055 ± 0.014
R134a	0.956 ± 0.007	0.942 ± 0.007	0.044 ± 0.011
R600a	0.928 ± 0.010	0.907 ± 0.012	0.077 ± 0.020

Table 4.12 – TMAC values for flows of N_2, R134a, and R600a in microtubes A, B and C. First-order results are shown in parentheses.

Gas	microtube		
	A	B	C
N_2	0.970 ± 0.003 (0.960 ± 0.003)	0.973 ± 0.007 (0.966 ± 0.008)	1.045 ± 0.008 (1.035 ± 0.009)
R134a	0.982 ± 0.004 (0.974 ± 0.003)	0.970 ± 0.006 (0.964 ± 0.005)	1.040 ± 0.004 (1.032 ± 0.004)
R600a	1.008 ± 0.008 (0.997 ± 0.007)	0.994 ± 0.005 (0.984 ± 0.004)	1.060 ± 0.007 (1.048 ± 0.006)

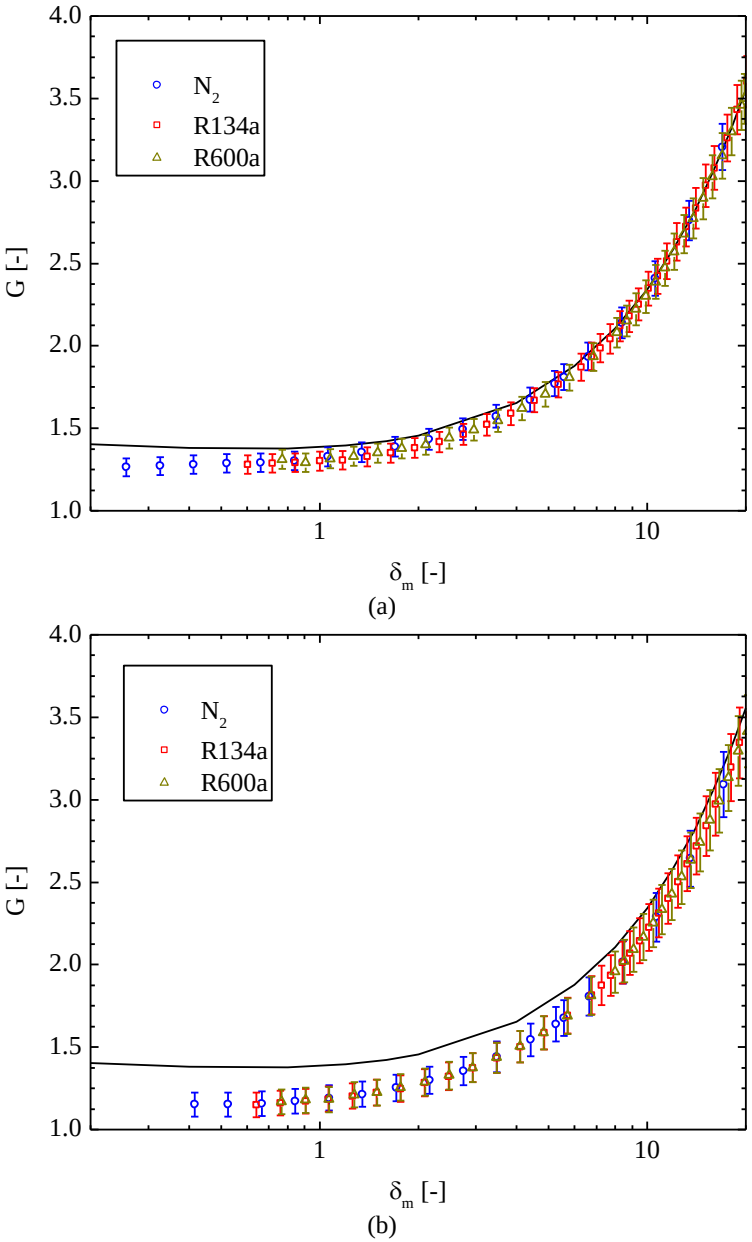

Figure 4.18 – Reduced mass flow rates of N_2, R134a and R600a in (a) microtube B (copper) and (b) microtube C (brass).

4.5 SUMMARY

In this chapter, results for mass flow rates and slip and accommodation coefficients were obtained for N_2 flows in a stainless steel microtube and were compared with data from the literature. Good agreement was observed in all flow situations, thus validating the experimental setup and procedure employed in the present study. The independence of the results with respect to the experimental setup was also confirmed with additional measurements performed with an experimental setup developed at INSA Toulouse. Besides, the dynamic constant volume technique was validated for the measurement of quasi-stationary mass flow rates and used to determine the conductance of channels when the volumes of the upstream and downstream reservoirs were equal. The results closely followed the semi-empirical expression provided by Knudsen (1909) for diffuse surfaces. Experiments were also conducted for N_2 flows in a rectangular cross section microchannel with h/w close to 1. TMAC values close to 0.8 were obtained.

Finally, the effect of the gas chemical composition and channel characteristics (material and surface finishing) on the gas–surface interaction was investigated by considering polyatomic gases R134a and R600a and metallic materials stainless steel, copper and brass. Both parameters showed a small influence on the TMAC value, with all results approaching a completely diffuse interaction. Slightly higher values were obtained for R600a flows and for flows in the brass microtube.

5 CONCLUSIONS

The behavior of gas microflows deviates from the conventional continuum theory owing to the absence of thermodynamic equilibrium at the fluid boundaries. Alternative theoretical models based on continuum and kinetic theory use the TMAC to account for the gas–surface interaction at the molecular level.

Most studies in the literature provide data regarding TMAC of flows of noble gases and gases of simple molecules, such as N_2, O_2 and CO_2, over silica or silicon surfaces. Data regarding flows of polyatomic molecules and over metallic surfaces are scarce. The present work provided experimental information on gas–surface interactions associated with gases commonly employed in the refrigeration industry, namely refrigerant fluids R134a and R600a, in metallic microchannels made of stainless steel, copper and brass in the slip and transition regimes.

A dynamic version of the well-known quasi-stationary constant volume technique was proposed to measure the mass flow rate of isothermal flows induced by pressure gradients. Moreover, two experimental setups were designed for the analysis of rarefied flows, one for circular section channels (microtubes) and the other for rectangular section channels with better characterized surfaces.

5.1 MAIN CONCLUSIONS

The proposed dynamic constant volume method was found to simplify the measurements of mass flow rates of gases in microchannels with smaller variability compared with data available in the literature. Compared with the standard constant volume technique, the dynamic method also allowed measurements of large datasets of mass flow rates under different rarefaction conditions more quickly and from single experiments. Moreover, the method was suitable to determine the flow conductance of channels under arbitrary rarefaction conditions.

The TMAC and slip coefficient were extracted from experimental measurements of mass flow rates. For slightly rarefied gas flows, these parameters were determined by comparing the measurements with theoretical predictions from the solution of the Navier-Stokes equation with the slip velocity boundary conditions at the walls. The results available in the literature based on the BGK kinetic equation were adopted to extract TMAC for more rarefied flows.

The results for N_2 flow in a stainless steel microtube indicated $\alpha \cong 1$ and were compared with data in the literature to validate the experimental setup and procedure. Similar results in the rectangular stainless steel microchannel were less conclusive, with a TMAC of 0.80. Questions related to leakage between the plates forming the channel and the process of cleaning the channel must be investigated in future work.

The dynamic constant volume technique was also employed to determine the conductance of N_2 flows in a microtube under a wide range of rarefaction conditions. The experimentally determined conductances were compared with a semi-empirical correlation available in the literature and excellent agreement was observed with a mean relative deviation of approximately 3%, thus confirming the adequacy of the measurement setup and procedure.

The results of R134a and R600a indicated that heavy polyatomic gases approach complete diffuse behavior ($\alpha \cong 1$), following the same trend observed for N_2. Significant deviations can be observed if this parameter is extracted from data in the slip flow regime considering Maxwell's formulation for the slip coefficient.

The chemical composition of the gas did not significantly affect the gas–surface interaction, although for R600a, the TMAC values were found to be slightly greater than those for N_2 and R134a. In this sense, polyatomic gases with heavier molecules can be better accommodated to the wall than lighter molecules. This is not in line with results from Ewart *et al*. (2007a), Graur *et al*. (2009), Perrier *et al*. (2011) and Hadj Nacer *et al*. (2014) for monoatomic gases, which indicate that the value of TMAC increases toward a complete diffuse reflection when the molecular weight decreases. The same tendency was also verified in the literature for flows of CO_2 and N_2, with the heavier gas presenting a TMAC closer to unity. This behavior could be associated with the intrinsic complexity of the molecular structure of polyatomic gases, which can affect the momentum exchange at the wall.

Finally, the metallic materials considered did not considerably affect the gas–surface interaction with $\alpha \cong 1$ for all channels regardless of the gas analyzed. The only variations, around 5% in terms of TMAC, were observed for the flows in the brass microtube and were attributed to the higher roughness of the surface.

5.2 FUTURE WORK

An important step to improve the experimental setup would be to assess any eventual leakage in the rectangular cross section microchannel.

Moreover, a more effective thermal insulation should be installed to analyze flows at higher pressures where temperature variations have a larger influence on the measurements.

The analysis could be extended to consider polyatomic gases with similar molecular structures and chemical compositions, such as hydrocarbons, to identify possible trends of the TMAC with molecular weight, as observed for monoatomic gases in the literature.

Another research direction would be to isolate the effects of the material and channel surface roughness by adopting channels with controlled surface roughness. Reduced surface roughness would allow better analysis of the influence of the surface material on the TMAC.

Finally, experiments with gaseous mixtures as well as temperature-driven flows should also be performed to reduce the lack of experimental data for such flows. In fact, two-phase flows of refrigerant fluids and lubricating oil in microchannels must also to be investigated to allow the characterization of leakage in the valves of refrigeration compressors.

REFERENCES

Agrawal, A., & Prabhu, S. V. (2008). Survey on measurement of tangential momentum accommodation coefficient. *Journal of Vacuum Science & Technology A: Vacuum, Surfaces, and Films, 26*(4), 634.

Albertoni, S., Cercignani, C., & Gotusso, L. (1963). Numerical evaluation of the slip coefficient. *Physics of Fluids, 6*(7), 993.

Arkilic, E., Schmidt, M., & Breuer, K. (1997). Gaseous slip flow in long microchannels. *Journal of Microelectromechanical Systems, 6*(2), 167-178.

Arkilic, E. B., Breuer, K. S., & Schmidt, M. A. (2001). Mass flow and tangential momentum accommodation in silicon micromachined channels. *Journal of Fluid Mechanics, 437*.

Balmer, R. T. (2011). *Modern engineering thermodynamics*. Amsterdam: Academic Press.

Batchelor, G. K. (1967). *An introduction to fluid dynamics*. Cambridge: Univ. Press.

Bhatnagar, P. L., Gross, E. P., & Krook, M. (1954). A model for collision processes in gases. I. Small amplitude processes in charged and neutral one-component systems. *Physical Review*, 94(3), 511-525.

Blanchard, D., & Ligrani, P. (2007). Slip and accommodation coefficients from rarefaction and roughness in rotating microscale disk flows. *Physics of Fluids, 19*(6), 063602.

Bird, G. A. (1994). *Molecular gas dynamics and the direct simulation of gas flows*. Oxford: Clarendon Press.

Cao, B., Chen, M., & Guo, Z. (2005). Temperature dependence of the tangential momentum accommodation coefficient for gases. *Applied Physics Letters, 86*(9), 091905.

Cao, B., Chen, M., & Guo, Z. (2006). Effect of surface roughness on gas flow in microchannels by molecular dynamics simulation. *International Journal of Engineering Science, 44*(13-14), 927-937.

Cercignani, C., & Lampis, M. (1971). Kinetic models for gas-surface interactions. *Transport Theory and Statistical Physics, 1*(2), 101-114.

Cercignani, C. (1988). *The Boltzmann equation and its applications*. New York: Springer-Verlag.

Chai, Z., Guo, Z., Zheng, L., & Shi, B. (2008). Lattice Boltzmann simulation of surface roughness effect on gaseous flow in a microchannel. *Journal of Applied Physics, 104*(1), 014902.

Colin, S., Lalonde, P., & Caen, R. (2004). Validation of a second-order slip flow model in rectangular microchannels. *Heat Transfer Engineering, 25*(3), 23-30.

Colin, S. (2014). Single-phase gas flow in microchannels. In *Heat Transfer and Fluid Flow in Minichannels and Microchannels*. Elsevier.

Davis, D. H., Levenson, L. L., & Milleron, N. (1964). Effect of "rougher-than-rough" surfaces on molecular flow through short ducts. *Journal of Applied Physics, 35*(3), 529.

Deissler, R. (1964). An analysis of second-order slip flow and temperature-jump boundary conditions for rarefied gases. *International Journal of Heat and Mass Transfer, 7*(6), 681-694.

Deng, Z., Chen, Y., & Shao, C. (2016). Gas flow through rough microchannels in the transition flow regime. *Physical Review E, 93*(1).

Engineering Equation Solver (Version 10.101) [Computer software]. (2016).

Ewart, T., Perrier, P., Graur, I., & Méolans, J. G. (2006). Mass flow rate measurements in gas micro flows. *Experiments in Fluids, 41*(3), 487-498.

Ewart, T., Perrier, P., Graur, I., & Méolans, J. G. (2007a). Tangential momentum accommodation in microtube. *Microfluidics and Nanofluidics, 3*(6), 689-695.

Ewart, T., Perrier, P., Graur, I. A., & Méolans, J. G. (2007b). Mass flow rate measurements in a microchannel, from hydrodynamic to near free molecular regimes. *Journal of Fluid Mechanics, 584*, 337.

Feynman, R. P. (1992). There's plenty of room at the bottom. *Journal of Microelectromechanical Systems*, 1(1), 60-66.

Gombosi, T. I. (1994). *Gaskinetic theory*. Cambridge: Cambridge University Press.

Graur, I. A., Perrier, P., Ghozlani, W., & Méolans, J. G. (2009). Measurements of tangential momentum accommodation coefficient for various gases in plane microchannel. *Physics of Fluids, 21*(10), 102004.

Guo, Z. Y., & Wu, X. B. (1998). Further study on compressibility effects on the gas flow and heat transfer in a microtube. *Microscale Thermophysical Engineering, 2*, 111-120.

Hadjiconstantinou, N. G. (2003). *Comment on Cercignani's second-order slip coefficient*. Physics of Fluids, 15(8), 2352.

Hadj Nacer, M., Graur, I., & Perrier, P. (2011). Mass flow measurement through rectangular microchannel from hydrodynamic to near free molecular regimes. *La Houille Blanche*, (4), 49-54.

Hadj Nacer, M. (2012). *Tangential momentum accommodation coefficient in microchannels with different surface materials (measurements and simulations)* (Ph. D. thesis). University of Aix-Marseille.

Hadj Nacer, M., Graur, I., Perrier, P., Méolans, J. G., & Wuest, M. (2014). Gas flow through microtubes with different internal surface coatings. *Journal of Vacuum Science & Technology A: Vacuum, Surfaces, and Films, 32*(2), 021601.

Harley, J. C., Huang, Y., Bau, H. H., & Zemel, J. N. (1995). Gas flow in micro-channels. *Journal of Fluid Mechanics, 284*(-1), 257.

Jousten, K., Menzer, H., & Niepraschk, R. (2002). A new fully automated gas flowmeter at the PTB for flow rates between 10^{-13} mol/s and 10^{-6} mol/s. *Metrologia, 39*(6), 519-529.

Karniadakis, G., Beskok, A., & Aluru, N. R. (2005). *Microflows and nanoflows: Fundamentals and simulation*. New York, NY: Springer.

Kennard, E. H. (1938). *Kinetic theory of gases: With an introduction to statistical mechanics*. New York: McGraw-Hill Book.

Knudsen, M. (1909). Die gesetze der molekularströmung und der inneren reibungsströmung der gase durch röhren. *Annalen Der Physik, 333*(1), 75-130. (*In German*)

Kremer, G. M. (2005). *Uma introdução à equação de Boltzmann*. São Paulo: Edusp. (*In Portuguese*).

Lihnaropoulos, J., & Valougeorgis, D. (2011). Unsteady vacuum gas flow in cylindrical tubes. *Fusion Engineering and Design, 86*(9-11), 2139-2142.

Lilly, T. C., Duncan, J. A., Nothnagel, S. L., Gimelshein, S. F., Gimelshein, N. E., Ketsdever, A. D., & Wysong, I. J. (2007). Numerical and experimental investigation of microchannel flows with rough surfaces. *Physics of Fluids, 19*(10), 106101.

Loyalka, S. K. (1968). Momentum and temperature-slip coefficients with arbitrary accommodation at the surface. *Journal of Chemical Physics, 48*, 5431.

Loyalka, S. K., Petrellis, N., & Storvick, T. S. (1975). Some numerical results for the BGK model: Thermal creep and viscous slip problems with arbitrary accomodation at the surface. *Physics of Fluids, 18*(9), 1094.

Loyalka, S. K. (1976). Poiseuille flow and thermal creep flow in long, rectangular channels in the molecular and transition flow regimes. *Journal of Vacuum Science and Technology, 13*(6), 1188.

Loyalka, S. K., & Storvick, T. S. (1979). Kinetic theory of thermal transpiration and mechanocaloric effect. III. Flow of a polyatomic gas between parallel plates. *The Journal of Chemical Physics, 71*(1), 339.

Maurer, J., Tabeling, P., Joseph, P., & Willaime, H. (2003). Second-order slip laws in microchannels for helium and nitrogen. *Physics of Fluids, 15*(9), 2613-2621.

Maxwell, J. C. (1879). On stresses in rarified gases arising from inequalities of temperature. *Philosophical Transactions of the Royal Society of London*, 170, 231-256.

McCormack, F. J. (1973). Construction of linearized kinetic models for gaseous mixtures and molecular gases. *Physics of Fluids, 16*(12), 2095.

McCulloh, K. E. (1987). Low-range flowmeters for use with vacuum and leak standards. *Journal of Vacuum Science & Technology A: Vacuum, Surfaces, and Films, 5*(3), 376.

Méolans, J. G., Nacer, M. H., Rojas, M., Perrier, P., & Graur, I. (2012). Effects of two transversal finite dimensions in long microchannel: Analytical approach in slip regime. *Physics of Fluids, 24*(11), 112005.

Mohamad, A. A. (2011). *Lattice Boltzmann method: Fundamentals and engineering applications with computer codes*. London: Springer.

Perrier, P., Graur, I. A., Ewart, T., & Méolans, J. G. (2011). Mass flow rate measurements in microtubes: From hydrodynamic to near free molecular regime. *Physics of Fluids, 23*(4), 042004.

Pitakarnnop, J., Varoutis, S., Valougeorgis, D., Geoffroy, S., Baldas, L., & Colin, S. (2010). A novel experimental setup for gas microflows. *Microfluidics and Nanofluidics, 8*(1), 57-72.

Porodnov, B. T., Suetin, P. E., Borisov, S. F., & Akinshin, V. D. (1974). Experimental investigation of rarefied gas flow in different channels. *Journal of Fluid Mechanics, 64*(03), 417.

Porodnov, B. T., Kulev, A. N., & Tuchvetov, F. T. (1978). Thermal transpiration in a circular capillary with a small temperature difference. *Journal of Fluid Mechanics, 88*(04), 609.

Rojas-Cardenas, M., Graur, I., Perrier, P., & Meolans, J. G. (2011). Thermal transpiration flow: A circular cross-section microtube submitted to a temperature gradient. *Physics of Fluids, 23*(3), 031702.

Rovenskaya, O. (2013). Kinetic analysis of surface roughness in a microchannel. *Computers & Fluids, 77,* 159-165.

Sazhin, O. V., Borisov, S. F., & Sharipov, F. (2001). Accommodation coefficient of tangential momentum on atomically clean and contaminated surfaces. *Journal of Vacuum Science & Technology A: Vacuum, Surfaces, and Films, 19*(5), 2499.

Shakhov, E. M. (1968). Generalization of the Krook kinetic relaxation equation. *Fluid Dynamics, 3*(5), 95-96.

Sharipov, F. M., & Seleznev, V. D. (1994). Rarefied gas flow through a long tube at any pressure ratio. *Journal of Vacuum Science & Technology A: Vacuum, Surfaces, and Films, 12*(5), 2933.

Sharipov, F., & Seleznev, V. (1998). Data on internal rarefied gas flows. *Journal of Physical and Chemical Reference Data, 27*(3), 657.

Sharipov, F. (1999). Rarefied gas flow through a long rectangular channel. *Journal of Vacuum Science & Technology A: Vacuum, Surfaces, and Films, 17*(5), 3062.

Sharipov, F. (2003). Application of the Cercignani–Lampis scattering kernel to calculations of rarefied gas flows. III. Poiseuille flow and thermal creep through a long tube. *European Journal of Mechanics B/Fluids, 22,* 145-154.

Sharipov, F. (2011). Data on the velocity slip and temperature jump on a gas-solid interface. *Journal of Physical and Chemical Reference Data, 40*(2), 023101.

Sharipov, F. (2012). Transient flow of rarefied gas through an orifice. *Journal of Vacuum Science & Technology A: Vacuum, Surfaces, and Films, 30*(2), 021602.

Sharipov, F. (2013). Transient flow of rarefied gas through a short tube. *Vacuum, 90,* 25-30.

Sharipov, F., & Graur, I. (2014). General approach to transient flows of rarefied gases through long capillaries. *Vacuum, 100,* 22-25.

Sharipov, F. (2016). *Rarefied gas dynamics: Fundamentals for research and practice*. Weinheim, Germany: Wiley-VCH.

Silva, L. R., & Deschamps, C. J. (2015). Modeling of gas leakage through compressor valves. *International Journal of Refrigeration, 53*, 195-205.

Suetin, P. E., Porodnov, B. T., Chernjak, V. G., & Borisov, S. F. (1973). Poiseuille flow at arbitrary Knudsen numbers and tangential momentum accommodation. *Journal of Fluid Mechanics, 60*(3), 581-592.

Sugiyama, W., Sawada, T., & Nakamori, K. (1996). Rarefied gas flow between two flat plates with two dimensional surface roughness. *Vacuum, 47*(6-8), 791-794.

Tabeling, P. (2005). *Introduction to microfluidics*. Oxford, U.K.: Oxford University Press.

Turner, S. E., Lam, L. C., Faghri, M., & Gregory, O. J. (2004). Experimental investigation of gas flow in microchannels. *Journal of Heat Transfer, 126*, 753-763.

Vargas, M., Naris, S., Valougeorgis, D., Pantazis, S., & Jousten, K. (2014). Hybrid modeling of time-dependent rarefied gas expansion. *Journal of Vacuum Science & Technology A: Vacuum, Surfaces, and Films, 32*(2), 021602.

Vincenti, W. G., & Kruger, C. H. (1965). *Introduction to physical gas dynamics*. New York: Wiley.

Yamaguchi, H., Hanawa, T., Yamamoto, O., Matsuda, Y., Egami, Y., & Niimi, T. (2011). Experimental measurement on tangential momentum accommodation coefficient in a single microtube. *Microfluidics and Nanofluidics, 11*(1), 57-64.

Yamaguchi, H., Matsuda, Y., & Niimi, T. (2012). Tangential momentum accommodation coefficient measurements for various materials and gas species. *Journal of Physics: Conference Series, 362*, 012035.

Yan, H., Zhang, W., Peng, Z., & Meng, G. (2015). Effect of random surface topography on the gaseous flow in microtubes with an extended slip model. *Microfluidics and Nanofluidics, 18*(5-6), 897-910.

Yoshida, H., Shiro, M., Arai, K., Hirata, M., & Akimichi, H. (2010). Effect of surface material and roughness on conductance of channel between parallel disks at molecular flow. *Journal of Vacuum Science & Technology A: Vacuum, Surfaces, and Films, 28*(4), 937.

Zhang, W., Meng, G., & Wei, X. (2012a). A review on slip models for gas microflows. *Microfluidics and Nanofluidics*, 13(6), 845-882.

Zhang, C., Chen, Y., Deng, Z., & Shi, M. (2012b). Role of rough surface topography on gas slip flow in microchannels. *Physical Review E, 86*(1).

LIST OF OWN PUBLICATIONS

JOURNALS

Silva, E., Rojas-Cardenas, M., & Deschamps, C. J. (2016). Experimental analysis of velocity slip at the wall for gas flows of nitrogen, R134a, and R600a through a metallic microtube. *International Journal of Refrigeration*, 66, 121-132.

Rojas-Cardenas, M., Silva, E., Ho, M. T., Deschamps, C. J., Graur, I. Time-dependent methodology for non-stationary mass flow rate measurements in a long micro-tube: Experimental and numerical analysis at arbitrary rarefaction conditions. *Microfluidics and Nanofluidics*, submitted.

PROCEEDINGS OF CONFERENCES

Silva, E., Nicoluzzi, M. F., Rojas-Cardenas, M., & Deschamps C. J. (2016). Analysis of Viscous Slip at Wall in the Flows of R134a and R600a through Metallic Microtubes. *23rd International Compressor Engineering Conference at Purdue*.

Silva, E., Deschamps, C. J., & Rojas-Cardenas, M. (2015). Mass Flow Rate Measurements Through Metallic Microtubes in the Slip and Transition Regimes. *ASME 13th International Conference on Nanochannels, Microchannels, and Minichannels*.

Silva, E., Rojas-Cardenas, M., & Deschamps C. J. (2015). Tangential Momentum Accommodation Coefficient Measurements of Refrigerant R134a (Tetrafluoroethane) in Metallic Microtubes. *2nd European Conference on Non-equilibrium Gas Flows*. (Extended abstract)

Silva, E., Rojas-Cardenas, M., & Deschamps C. J. (2014). Experimental Analysis of Refrigerant Flow in Small Clearances. *22nd International Compressor Engineering Conference at Purdue*.

APPENDIX A – ANALYSIS OF UNCERTAINTIES

In the experiments performed only the pressures and temperatures in the upstream and downstream reservoirs were monitored along time. All other quantities were derived from these measurements. Then, the uncertainties associated with any quantity of interest needed to be estimated from the uncertainties associated with pressure and temperature measurements. In this section, these uncertainties were estimated in conjunction with the uncertainties associated with the volumes of the reservoirs. Subsequently, the uncertainties associated with the derived quantities were also assessed.

A.1 TEMPERATURE AND PRESSURE MEASUREMENTS

The temperature measurements were performed using different instruments in the experimental setups considered. However, in every case the uncertainty associated with the temperature measurement in a particular reservoir was predominantly determined by the accuracy of the instrument itself. The uncertainties of the instruments used in each experimental setup are described in Table A.1 together with the respective standard uncertainties $u(T_i)$ for a confidence level of 95.45%.

Table A.1 –Uncertainties of the temperature sensors.

Experimental setup	Uncertainty [°C]	$u(T_i)$ [°C]
UFSC1	0.5	0.25
UFSC2	$1/3\,(0.3 + 0.005\lvert T_i\rvert)$	$1/6\,(0.3 + 0.005\lvert T_i\rvert)$
INSA	$(0.3 + 0.005\lvert T_i\rvert)$	$1/2\,(0.3 + 0.005\lvert T_i\rvert)$

On the other hand, the same pressure transducers were employed independently of the experimental setup considered. In this case, the pressure uncertainty was assumed to be a function of the sensor uncertainty (0.2% of the reading) and resolution (0.003% of the full scale). Then, the standard uncertainty $u(P_i)$ for a confidence level of 95.45% can be estimated as:

$$u(P_i) = \sqrt{\left(\frac{0.1}{100}P_i\right)^2 + \left(\frac{0.0015}{100\sqrt{3}}FS_i\right)^2}\ , \tag{A.1}$$

where FS_i is the full scale of the pressure sensor of interest. The second term on the right hand side of equation (A.1), associated with the sensor resolution, was determined assuming a uniform distribution.

A.2 VOLUME MEASUREMENT

To calculate the mass flow rate of gas through the microchannel using Eq. (3.25) the volume of the reservoirs were determined with Eqs. (3.33) and (3.34). Therefore, the uncertainty related to the volume of the reservoirs depended on the uncertainties of the additional volume and of the coefficients a and b. The following correlations can be derived from Eqs. (3.33) and (3.34) to estimate the standard uncertainties $u(V_1)$ and $u(V_2)$ of the volumes:

$$\frac{u(V_1)}{V_1} = \sqrt{\left[\frac{u(V_C)}{V_C}\right]^2 + \left[\left(\frac{V_2}{V_1} + \frac{V_2}{V_C}\right)u(a)\right]^2 + \left[\frac{V_2}{V_C}u(b)\right]^2}\ , \tag{A.4}$$

and

$$\frac{u(V_2)}{V_2} = \sqrt{\left[\frac{u(V_C)}{V_C}\right]^2 + \left[\frac{V_2}{V_C}u(a)\right]^2 + \left[\frac{V_2}{V_C}u(b)\right]^2}\ . \tag{A.5}$$

A.3 DERIVED QUANTITIES

The mass flow rate was calculated from Eq. (3.25). Then, its standard uncertainty $u(\dot{m})$ was estimated from a combination of the standard uncertainties of the volume of the reservoir $u(V_i)$, as estimated from Eqs. (A.4) or (A.5), the temperature $u(T_i)$, the pressure $u(P_i)$ and the coefficients of the fitting function $u(\Psi_{B,i})$, $u(\Psi_{C,i})$ and $u(\Psi_{D,i})$. Recognizing that the latter terms came from a fitting function that fits experimental data very closely and in order to simplify the calculations, we considered that $u(\Psi_{B,i}) = u(\Psi_{C,i}) = u(\Psi_{D,i}) = 0$. Also, an additional uncertainty related to the term $(1 - \varepsilon_i)$ in Eq. (3.4), that was assumed as unitary in Eq. (3.25) was considered. As mentioned in Section 3.1.1, all experiments were performed under the condition that $\varepsilon_i \leq 0.01$, then, in the worst scenario $u(1 - \varepsilon_i) = 0.5\%$ considering a confidence level of 95.45%. Consequently, $u(\dot{m})$ was estimated as:

$$\frac{u(\dot{m})}{\dot{m}} = \sqrt{\left[\frac{u(V_i)}{V_i}\right]^2 + \left[\frac{u(T_i)}{T_i}\right]^2 + \left[\frac{u(P_i)}{(P_i - \Psi_{D,i})}\right]^2 + [u(1-\varepsilon_i)]^2} \quad . \quad \text{(A.6)}$$

Similarly, estimations for the uncertainties associated with S and G were obtained from Eqs. (3.41), (3.44), (3.52) and (3.54). In this case, the uncertainties related to the cross section geometries of the channels and the mass flow rate prevail. Therefore, for circular cross section channels:

$$\frac{u(S)}{S} = \sqrt{\left[\frac{u(\dot{m})}{\dot{m}}\right]^2 + \left[4\frac{u(D)}{D}\right]^2} \quad , \quad \text{(A.7)}$$

$$\frac{u(G)}{G} = \sqrt{\left[\frac{u(\dot{m})}{\dot{m}}\right]^2 + \left[3\frac{u(D)}{D}\right]^2} \quad . \quad \text{(A.8)}$$

Alternatively, for rectangular cross section channels:

$$\frac{u(S)}{S} = \sqrt{\left[\frac{u(\dot{m})}{\dot{m}}\right]^2 + \left[3\frac{u(h)}{h}\right]^2 + \left[\frac{u(w)}{w}\right]^2} \quad , \quad \text{(A.9)}$$

$$\frac{u(G)}{G} = \sqrt{\left[\frac{u(\dot{m})}{\dot{m}}\right]^2 + \left[2\frac{u(h)}{h}\right]^2 + \left[\frac{u(w)}{w}\right]^2} \, . \quad \text{(A.10)}$$

APPENDIX B – FITTING AND SLIP COEFFICIENTS FOR COPPER AND BRASS MICROTUBES

Table B.1 – Fitting coefficients of first- (top) and second-order (bottom) according to the pressure ratio in microtube B.

Π	B_{exp}	C_{exp}	R^2
Nitrogen			
2	9.770 ± 0.066	-	1.000
	9.629 ± 0.053	2.635 ± 0.269	1.000
3	9.793 ± 0.085	-	1.000
	9.651 ± 0.063	2.528 ± 0.293	1.000
5	9.767 ± 0.130	-	0.999
	9.660 ± 0.109	2.486 ± 0.570	1.000
8	9.772 ± 0.145	-	0.999
	9.672 ± 0.125	2.296 ± 0.615	1.000
R134a			
2	9.813 ± 0.085	-	0.998
	9.689 ± 0.095	1.323 ± 0.504	1.000
3	9.827 ± 0.087	-	0.998
	9.704 ± 0.105	1.327 ± 0.608	1.000
5	9.824 ± 0.093	-	0.997
	9.694 ± 0.102	1.484 ± 0.544	1.000
8	9.830 ± 0.101	-	0.997
	9.689 ± 0.101	1.553 ± 0.513	1.000
R600a			
2	9.440 ± 0.053	-	0.999
	9.255 ± 0.048	3.178 ± 0.269	1.000
3	9.459 ± 0.052	-	0.999
	9.288 ± 0.045	3.128 ± 0.233	1.000
5	9.467 ± 0.052	-	0.999
	9.266 ± 0.048	3.467 ± 0.275	1.000
8	9.456 ± 0.052	-	0.999
	9.281 ± 0.052	3.409 ± 0.286	1.000

Table B.2 – Slip coefficients of first- (top) and second-order (bottom) according to the pressure ratio in microtube B.

Π	σ_P	σ_{2P}
	Nitrogen	
2	1.082 ± 0.007 1.067 ± 0.006	- 0.062 ± 0.006
3	1.085 ± 0.009 1.069 ± 0.007	- 0.056 ± 0.007
5	1.082 ± 0.014 1.070 ± 0.012	- 0.051 ± 0.012
8	1.083 ± 0.016 1.071 ± 0.014	- 0.042 ± 0.011
	R134a	
2	1.087 ± 0.009 1.073 ± 0.011	- 0.031 ± 0.012
3	1.089 ± 0.010 1.075 ± 0.012	- 0.030 ± 0.014
5	1.088 ± 0.010 1.074 ± 0.011	- 0.030 ± 0.011
8	1.089 ± 0.011 1.073 ± 0.011	- 0.029 ± 0.009
	R600a	
2	1.046 ± 0.006 1.025 ± 0.005	- 0.075 ± 0.006
3	1.048 ± 0.006 1.029 ± 0.005	- 0.070 ± 0.005
5	1.049 ± 0.006 1.026 ± 0.005	- 0.070 ± 0006
8	1.048 ± 0.006 1.028 ± 0.006	- 0.063 ± 0.005

Table B.3 – Fitting coefficients of first- (top) and second-order (bottom) according to the pressure ratio in microtube C.

Π	B_{exp}	C_{exp}	R^2
Nitrogen			
2	8.561 ± 0.061	-	1.000
	8.410 ± 0.048	2.664 ± 0.250	1.000
3	8.592 ± 0.080	-	1.000
	8.461 ± 0.067	2.382 ± 0.311	1.000
5	8.623 ± 0.101	-	0.999
	8.418 ± 0.096	2.697 ± 0.500	1.000
8	8.581 ± 0.132	-	0.999
	8.428 ± 0.116	2.632 ± 0.572	1.000
R134a			
2	8.630 ± 0.032	-	1.000
	8.487 ± 0.041	2.073 ± 0.235	1.000
3	8.631 ± 0.041	-	0.999
	8.504 ± 0.045	2.045 ± 0.229	1.000
5	8.635 ± 0.051	-	0.999
	8.508 ± 0.058	2.082 ± 0.330	1.000
8	8.631 ± 0.060	-	0.999
	8.513 ± 0.062	2.069 ± 0.337	1.000
R600a			
2	8.365 ± 0.092	-	0.997
	8.141 ± 0.091	3.767 ± 0.508	1.000
3	8.392 ± 0.087	-	0.997
	8.200 ± 0.080	3.473 ± 0.410	1.000
5	8.374 ± 0.083	-	0.997
	8.193 ± 0.079	3.697 ± 0.442	1.000
8	8.370 ± 0.081	-	0.998
	8.225 ± 0.077	3.517 ± 0.409	1.000

Table B.4 – Slip coefficients of first- (top) and second-order (bottom) according to the pressure ratio in microtube C.

Π	σ_P	σ_{2P}
	Nitrogen	
2	0.948 ± 0.007 0.932 ± 0.005	- 0.063 ± 0.006
3	0.952 ± 0.009 0.937 ± 0.007	- 0.053 ± 0.007
5	0.955 ± 0.011 0.932 ± 0.011	- 0.055 ± 0.010
8	0.951 ± 0.015 0.934 ± 0.013	- 0.048 ± 0.010
	R134a	
2	0.956 ± 0.004 0.940 ± 0.005	- 0.049 ± 0.006
3	0.956 ± 0.005 0.942 ± 0.005	- 0.046 ± 0.005
5	0.957 ± 0.006 0.942 ± 0.006	- 0.042 ± 0.007
8	0.956 ± 0.007 0.943 ± 0.007	- 0.038 ± 0.006
	R600a	
2	0.927 ± 0.010 0.902 ± 0.010	- 0.089 ± 0.012
3	0.930 ± 0.010 0.908 ± 0.009	- 0.078 ± 0.009
5	0.928 ± 0.009 0.908 ± 0.009	- 0.075 ± 0.009
8	0.927 ± 0.009 0.911 ± 0.009	- 0.065 ± 0.008

ANNEX A – REDUCED MASS FLOW RATE FOR CIRCULAR CHANNEL

Reduced mass flow rate Q (Eq. (3.43)) as a function of the rarefaction parameter δ and α (Porodnov *et al*., 1978).

δ	α										
	1.00	0.98	0.96	0.94	0.92	0.90	0.88	0.86	0.84	0.82	0.80
0.01	1.476	1.534	1.594	1.657	1.723	1.791	1.862	1.936	2.026	2.099	2.187
0.02	1.460	1.516	1.574	1.635	1.693	1.764	1.833	1.904	1.983	2.059	2.144
0.04	1.438	1.492	1.547	1.605	1.666	1.728	1.794	1.861	1.933	2.002	2.085
0.06	1.423	1.475	1.529	1.585	1.643	1.703	1.766	1.832	1.899	1.979	2.045
0.08	1.412	1.462	1.515	1.569	1.626	1.685	1.746	1.810	1.873	1.945	2.014
0.1	1.403	1.452	1.503	1.556	1.611	1.668	1.728	1.790	1.853	1.921	1.992
0.2	1.381	1.426	1.474	1.523	1.574	1.627	1.682	1.480	1.806	1.885	1.931
0.4	1.378	1.420	1.465	1.510	1.562	1.615	1.668	1.719	1.768	1.827	1.888
0.6	1.397	1.437	1.479	1.523	1.568	1.621	1.671	1.721	1.772	1.828	1.888
0.8	1.424	1.464	1.505	1.547	1.592	1.638	1.687	1.737	1.791	1.846	1.904
1	1.457	1.496	1.536	1.578	1.622	1.668	1.715	1.765	1.818	1.873	1.930
2	1.665	1.693	1.732	1.773	1.816	1.861	1.907	1.956	2.007	2.060	2.116
3	1.877	1.914	1.953	1.994	2.037	2.081	2.127	2.176	2.227	2.280	2.336
4	2.107	2.145	2.184	2.225	2.267	2.312	2.358	2.406	2.458	2.511	2.567
5	2.343	2.381	2.420	2.461	2.504	2.548	2.594	2.643	2.694	2.747	2.803
6	2.583	2.620	2.659	2.700	2.742	2.787	2.833	2.881	2.934	2.987	3.003
7	2.824	2.862	2.901	2.942	2.984	3.029	3.075	3.123	3.167	3.229	3.285
8	3.067	3.105	3.144	3.185	3.228	3.272	3.319	3.375	3.420	3.473	3.529
9	3.312	3.349	3.389	3.430	3.472	3.517	3.563	3.612	3.664	3.718	3.778
10	3.557	3.595	3.642	3.675	3.717	3.761	3.808	3.856	3.910	3.963	4.019

ANNEX B – REDUCED MASS FLOW RATE FOR SQUARE CHANNEL

Reduced mass flow rate Q (Eq. (3.53)) as a function of the rarefaction parameter δ and α for $h/w = 1$ (Hadj Nacer, 2012).

δ	α					
	1.00	0.95	0.90	0.85	0.80	0.60
0.001	0.8375	0.9037	0.9781	1.0622	1.1578	1.7113
0.005	0.8334	0.8986	0.9719	1.0546	1.1484	1.6896
0.01	0.8290	0.8932	0.9654	1.0467	1.1390	1.6694
0.05	0.8075	0.8677	0.9350	1.0107	1.0962	1.5831
0.1	0.7933	0.8507	0.9147	0.9866	1.0677	1.5274
0.2	0.7774	0.8315	0.8918	0.9593	1.0354	1.4655
0.5	0.7619	0.8116	0.8669	0.9288	0.9986	1.3932
0.8	0.7629	0.8107	0.8639	0.9236	0.9907	1.3717
1	0.7674	0.8145	0.8670	0.9257	0.9920	1.3679
2	0.8090	0.8549	0.9061	0.9634	1.0280	1.3954
4	0.9232	0.9697	1.0213	1.0791	1.1459	1.5153
5	0.9873	1.0344	1.0867	1.1451	1.2108	1.5826
8	1.1836	1.2321	1.2859	1.3459	1.4132	1.7922
10	1.3179	1.3672	1.4219	1.4827	1.5510	1.9341
15	1.6592	1.7100	1.7662	1.8287	1.8987	2.2900
20	2.0045	2.0563	2.1136	2.1772	2.2483	2.6453